ALMA MATER STUDIORUM · UNIVERSITY OF BOLOGNA

School of Science
Department of Physics and Astronomy
Master Degree in Physics

TWISTED BILAYER GRAPHENE:

Effective model, topological states and relevant symmetries

Supervisor:
Prof. Cristian Degli Esposti Boschi

Co-supervisor:
Prof. Elisa Ercolessi

Submitted by:
Maria Vittoria Gurrieri

Academic Year 2019/2020

Abstract

Correlated Mott-insulating states alternated with unconventional superconductivity have been lately observed in magic-angle graphene superlattices. For small angles of rotation the band structure of twisted bilayer graphene (TBG) exhibits isolated nearly-flat bands, which are responsible for such correlated behaviour. At first, we describe TBG effective model in order to construct a topological phase diagram for the mini-bands near charge neutrality. Then, through symmetry analysis, we try to unravel and understand the limit of such model, when one tries to revert back to localised low-energy orbitals in real space (Wannier functions) for Hubbard-like descriptions.

CONTENTS

INTRODUCTION

Two articles published in 2018 on the science journal "Nature" by Jarillo-Herrero and colleagues [1] [2] represent a remarkable step for those studying condensed matter physics. Those papers carry the discovery of correlated insulating and superconducting states in "magic angle" twisted bilayer graphene (TBG), leading to a considerably intensified theoretical activity in the already burgeoning field of graphene research.

This fascinating material is made of a 2-D layer of carbon atoms that are bonded together, generating an honeycomb shaped lattice. Graphene was discovered for the first time in 2004 by two scientists, Geim and Novoselov [3], who were trying to isolate the thinnest possible layer of graphite through common scotch tape. Since then this material has been used for the most varied purposes and still now its possible applications are being explored.

However, the study of graphene honeycomb lattice is much older. The linear energy dispersion relation at the Dirac cones makes this material a semi-metal with unusual electronic properties, that are best described by theories of mass-less relativistic particles. Remarkable in the history of graphene was the discovery of Quantum Hall effect and topological phases of matter. In 1987 Duncan Haldane proposed its *Haldane model* [4], to explain Anomalous Quantum Hall effect in the presence of Bloch band structure and time reversal broken symmetry in graphene lattice structures. As the studies on topological phase transitions intensified, graphene became a reference model in the understanding of topological materials.

A turning point came in 2012 with the continuum Dirac model for small angle twisted bilayer graphene by A. MacDonald and collegues [5]. When 2-D materials are stacked with a relative twist, a so-called moiré pattern is formed. For small angles of rotation the two layers of graphene show a long range modulation shaped as an honeycomb super-lattice with extended AA stacking regions at the vertices, alternate with AB/BA ones, figure (1).

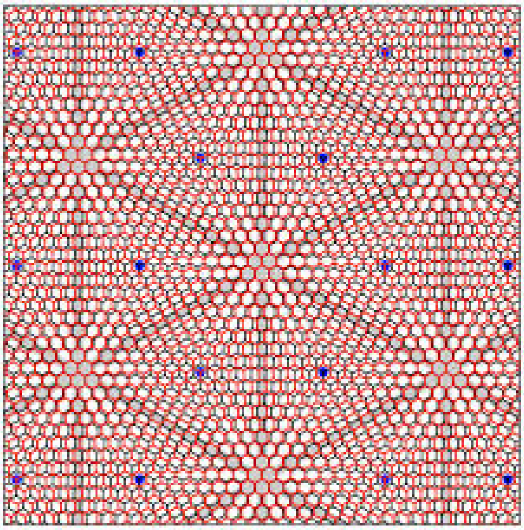

Figure 1: *Two stacked lattices of graphene with a twist. In the picture it is shown the formation of the hexagonal super-cell of the moiré lattice for two sheets of graphene rotated about a common atom site. The vertices of the triangles coincide with AA stacking regions, while the internal part correspond to AB ones.* [6]

Although the formation of a crystalline lattice depends on the commensurability of the rotation angle, MacDonald formulated a low-energy effective Hamiltonian always valid for small angles of twist. This in fact, is able to describe the electronic structure using Bloch bands even for incommensurate patterns.

The band structure is thus folded into a mini Brillouin Zone, whose valleys show interesting topological properties. At small twist angles low energy nearly flat bands form, inducing a significant decrease in Fermi velocity at the charge neutrality points. In particular, Fermi velocity drops to zero at a series of special angles called *magic angles*. Correlated insulating states at half-filling of these bands, that can be possibly explained with a Mott-like theory, have been observed experimentally. More interestingly, at the magic angle when the flat bands are doped in a slightly different way from the Mott-like insulating states, superconductivity is achieved [2]. The power of this material relies on the possibility of studying correlated systems controlling its electronic density and low-energy bandwidth, simulating different scenarios. In this prospective it is necessary the implementation of a tight-binding model to explore unsolved questions. Nevertheless this remains an open problem and a faithful tight-binding model has not been formulated yet.

This work is divided into five sections following the most important steps in the comprehension of TBG. High regard is placed in understanding the continuum model and the topological properties of the single valley low-energy nearly-flat bands. The effect of relaxation of the two layers, together with the symmetries of the effective model, are examined on two levels. At first they are used to construct a topological path diagram for the single valley flat bands. Later, they are studied as limits in the construction of a tight-binding model.

1

MONOLAYER GRAPHENE

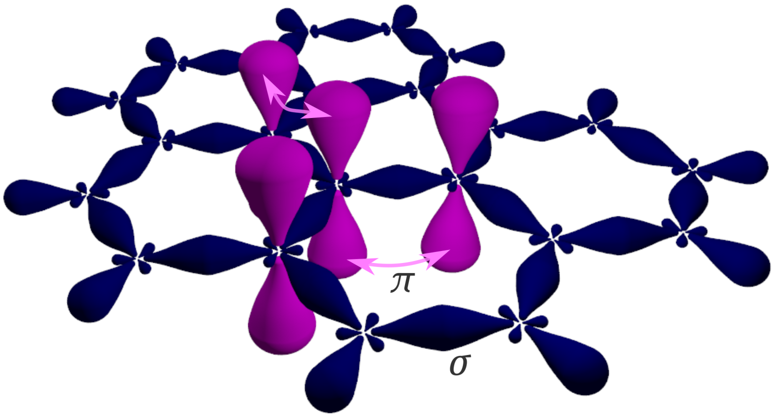

Figure 1.1: *Graphene lattice. The 2D planar structure is shown with its bonds. σ-bonds result from an overlap of sp^2 hybrid orbitals and tie together three nearest neighbors atoms of carbon. Non-hybridised p orbitals, perpendicular to the plane, form half-filled bands that can generate π bonds with other atoms [7]*

Graphene is a single layer material made of a two dimensional lattice of carbon atoms, whose orbitals have sp^2 hybridisation. Each atom in fact is tied together with its three nearest neighbors by σ-bonds, creating a trigonal planar structure. The total shape results in a honeycomb lattice of hexagonal cells with the sigma bonds on the plane and the non-hybridised p orbitals perpendicular to the structure. Because of the carbon electrons structure $(1s)^2(2s)^2(2p)^4$, p, orbitals form half-filled bands that can generate π bonds with other atoms and make graphene a semi-metal. These lasts π bonds, in particular, are responsible for the electronic conduction of graphene.

1.1 Direct and reciprocal lattice

Because of graphene crystal structure, it is possible to find within the lattice a unit cell shaped of a 2-dimensional rhombus. The cell consists in two identical carbon atoms placed at two different positions labelled by A and B respectively. The unit cell constant is $a_0 = a\sqrt{3}$, where $a = 1,42\text{Å}$ is the distance between two nearest neighborhood atoms A and B. The 2-D unit cell vectors are $\boldsymbol{a}_1 = \frac{a}{2}(3, \sqrt{3})$ and $\boldsymbol{a}_2 = \frac{a}{2}(3, -\sqrt{3})$, so any position vector in the lattice can be expressed as a linear combination $\boldsymbol{R} = n_1\boldsymbol{a}_1 + n_2\boldsymbol{a}_2$ with n_1 and n_2 real integers. The result is a structure of two sub-lattices made up of only A and only B atoms that interpenetrate.

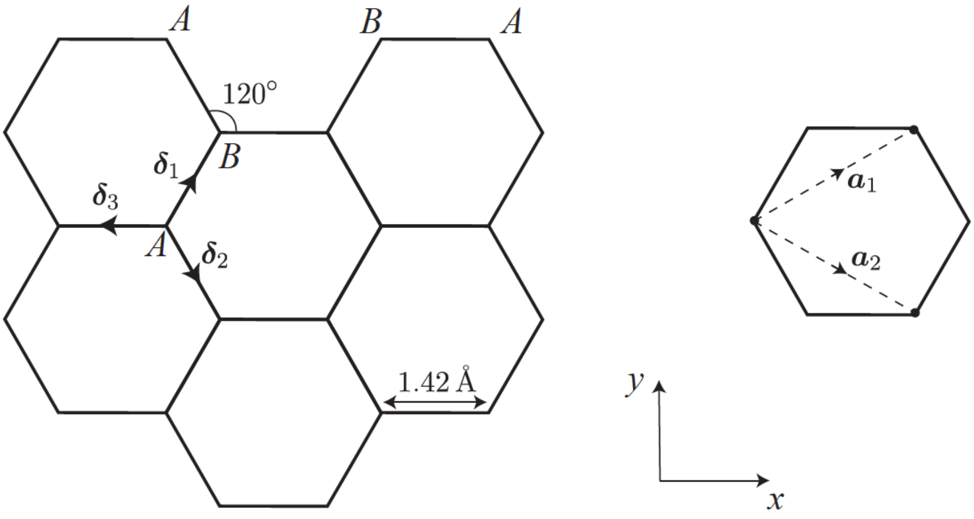

Figure 1.2: *Honeycomb lattice in real space. The lattice is made up of hexagonal cells with A and B inequivalent sub-lattices. The vectors $\boldsymbol{\delta}_n$ connect the nearest-neighborhoor cites, whereas $\boldsymbol{a}_1$ and $\boldsymbol{a}_2$ are unit cell vectors, such that any position vector can be expressed as $\boldsymbol{R} = n_1\boldsymbol{a}_1 + n_2\boldsymbol{a}_2$ with n_1 and n_2 real integers. $a = 1,42\text{Å}$ is the distance between two nearest neighborhood [8]*

From $\boldsymbol{a}_1$ and $\boldsymbol{a}_2$ it is possible to construct the reciprocal lattice basis vectors $\boldsymbol{b}_1$ and $\boldsymbol{b}_2$ which must satisfy $\boldsymbol{a}_i\boldsymbol{b}_j = 2\pi\delta_{ij}$, such that $\boldsymbol{b}_1 = \frac{2\pi}{3a}(1, \sqrt{3})$ and $\boldsymbol{b}_2 = \frac{2\pi}{3a}(1, -\sqrt{3})$. In a similar way to real lattice, every vector in the reciprocal space can be described by a linear combination of the basis $\boldsymbol{b}_1$ and $\boldsymbol{b}_2$, such that $\boldsymbol{k} = k_1\boldsymbol{b}_1 + k_2\boldsymbol{b}_2$ with k_1 and k_2 real integers. Hence, any generic exponential factor $e^{(i\boldsymbol{kR})}$ in Bloch wave functions with $\boldsymbol{k}$ a real vector, can be expressed restricting the wave number vector $\boldsymbol{k}$ to the First Brillouin Zone. It is geometrically parameterized by the same expression but with $\boldsymbol{k}_1$ and $\boldsymbol{k}_2$ defined in $[0,1]$. It follows that the FBZ has the same shape as the original hexagons of the honeycomb lattice, but it is rotated by a $\frac{\pi}{2}$ angle.

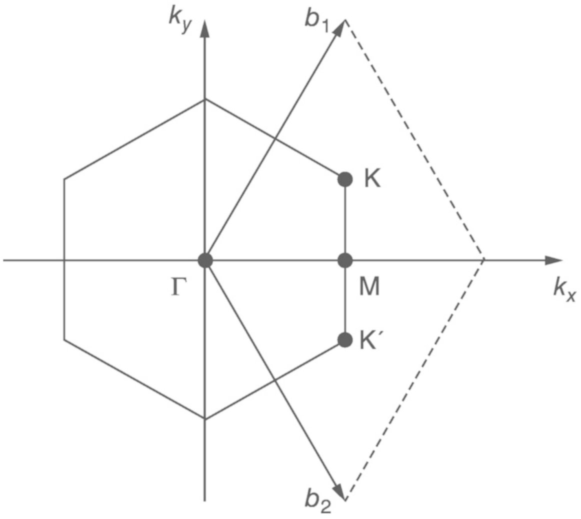

Figure 1.3: *Honeycomb lattice in reciprocal space. The figure shows the first Brillouin Zone.* $\boldsymbol{K}$ *and* $\boldsymbol{k'}$ *label the two inequivalent Dirac cones.* $\boldsymbol{b}_1$ *and* $\boldsymbol{b}_2$ *are the basis vectors, such that any vector in the reciprocal space can be written as* $\boldsymbol{k} = k_1\boldsymbol{b}_1 + k_2\boldsymbol{b}_2$ *with* k_1 *and* k_2 *real integers. To restrict* $\boldsymbol{k}$ *to the First Brillouin Zone* $\boldsymbol{k}_1$ *and* $\boldsymbol{k}_2$ *are defined in* $[0,1]$ *[9]*

The six vertices of the FBZ locate the Dirac cones that identify two set of three equivalent points. It is satisfactory then, to refer to just one point per group and to label it with K and K' respectively. These are located in the reciprocal space at position $\boldsymbol{K} = \frac{2\pi}{3a}(1, \frac{1}{\sqrt{3}})$ and $\boldsymbol{K'} = \frac{2\pi}{3a}(1, -\frac{1}{\sqrt{3}})$. Dirac cones are extremely important to describe the physics of graphene and to characterise its properties [9]. This is why a deep analysis of the shape of the energy bands close to those points is carried out in this work.

1.2 A tight-binding Hamiltonian

To study the non interacting-fermions band structure of graphene, it is sufficient to restrict the study to the analysis of electrons in the perpendicular p orbitals, the others in fact do not take place into its conductivity properties. A good description is given by a tight-binding Hamiltonian [10], in which electrons can hop to nearest-neighbor and to next nearest-neighbor atoms. The tight-biding Hamiltonian is

$$H = -t\sum_{\langle i,j\rangle}(a_i^\dagger b_j + h.c.) - t'\sum_{\langle\langle i,j\rangle\rangle}(a_i^\dagger a_j + b_i^\dagger b_j + h.c.) \tag{1.1}$$

where the spin index is understood. a_i and b_i are respectively the destruction operators of one electron in sub-lattice A and B; the angle brackets refer to nearest-neighbor, while the double ones to next to nearest-neighborhood atoms; h.c. stands for hermitian conjugate and in the end t and t' set the energy band scale of the two hopping processes. These last two terms have magnitude $t \approx 2.8$ eV and $0.02t \lesssim t' \lesssim 0.2t$ depending on the tight binding parameterization [9].

1.2.1 NEAREST NEIGHBOR HOPPINGS

It is convenient to start considering just the first piece of the Hamiltonian and neglecting the next nearest-neighbor hopping term. The expression thus assumes the form

$$H_0 = -\,t\sum_{\langle i,j\rangle}(a_i^\dagger b_j + h.c.) = -t\sum_{i\in A}\sum_{\delta}(a_i^\dagger b_{i+\delta} + h.c.)$$

where in the second equality the sum over n.n. is made explicit. The first summation contains all the $\boldsymbol{r}_i$ vectors pointing to sub-lattices A, while $\sum_\delta$ runs over the three vectors connecting the three B nearest neighborhood sites located at $\delta_1 = \frac{a}{2}(1, \sqrt{3})$, $\delta_2 = \frac{a}{2}(1, -\sqrt{3})$ and $\delta_3 = -a(1, 0)$. Since the lattice is periodic (no edges have been fixed and one can assume either infinite or periodic boundaries), a Fourier transform of the destruction and creation operator can be performed. Assuming the same number of A and B sites (N)

$$a_i = \frac{1}{N}\sum_{\boldsymbol{k}} e^{i\boldsymbol{k}\boldsymbol{r}_i} a_{\boldsymbol{k}}$$

$$b_i = \frac{1}{N}\sum_{\boldsymbol{k'}} e^{i\boldsymbol{k'}\boldsymbol{r}_i} b_{\boldsymbol{k'}}$$

the Hamiltonian becomes

$$
\begin{aligned}
H_0 =& -\frac{t}{N}\sum_{i\in A}\sum_{\boldsymbol{\delta}}\sum_{\boldsymbol{k},\boldsymbol{k}'}(e^{i(\boldsymbol{k}'-\boldsymbol{k})\boldsymbol{r}_i}e^{i\boldsymbol{k}'\boldsymbol{\delta}}a^\dagger_{\boldsymbol{k}}b_{\boldsymbol{k}'} + e^{i(\boldsymbol{k}-\boldsymbol{k}')\boldsymbol{r}_i}e^{-i\boldsymbol{k}'\boldsymbol{\delta}}b^\dagger_{\boldsymbol{k}'}a_{\boldsymbol{k}}) = \\
=& -t\sum_{\boldsymbol{\delta}}\sum_{\boldsymbol{k}}(e^{i\boldsymbol{k}\boldsymbol{\delta}}a^\dagger_{\boldsymbol{k}}b_{\boldsymbol{k}} + e^{-i\boldsymbol{k}\boldsymbol{\delta}}b^\dagger_{\boldsymbol{k}}a_{\boldsymbol{k}})
\end{aligned}
$$

where the sum over $\boldsymbol{r}_i$ in the exponential has been replaced with a Kronecker delta $\delta_{\boldsymbol{k},\boldsymbol{k}'}$ and N is the number of atoms in each sub-lattice A or B, to be kept large but finite for the moment. It follows that the Hamiltonian can be written as

$$
H_0 = \boldsymbol{\psi}^\dagger h(\boldsymbol{k})\boldsymbol{\psi} \quad \longrightarrow \quad h(\boldsymbol{k}) = -t\begin{pmatrix} 0 & \Delta_{\boldsymbol{k}} \\ \Delta^*_{\boldsymbol{k}} & 0 \end{pmatrix} \tag{1.2}
$$

with vectors

$$
\boldsymbol{\psi} = \begin{pmatrix} a_{\boldsymbol{k}} \\ b_{\boldsymbol{k}} \end{pmatrix} \qquad \boldsymbol{\psi}^\dagger = \begin{pmatrix} a^\dagger_{\boldsymbol{k}} & b^\dagger_{\boldsymbol{k}} \end{pmatrix}
$$

and

$$
\Delta_{\boldsymbol{k}} = \sum_{\boldsymbol{\delta}} e^{i\boldsymbol{k}\boldsymbol{\delta}} \quad \rightarrow \quad {\scriptstyle \boldsymbol{\delta}=\boldsymbol{\delta}_1,\boldsymbol{\delta}_2,\boldsymbol{\delta}_3}
$$

The eigenvalues of (1.2) are the two energy values

$$
\epsilon_\pm(\boldsymbol{k}) = \pm t\sqrt{\Delta_{\boldsymbol{k}}\Delta^*_{\boldsymbol{k}}} = \pm t\sqrt{3+f(\boldsymbol{k})} \tag{1.3}
$$

This result is obtained expanding $\Delta_{\boldsymbol{k}}$ as follows

$$
\begin{aligned}
\Delta_{\boldsymbol{k}} &= \sum_{\boldsymbol{\delta}} e^{i\boldsymbol{k}\boldsymbol{\delta}} = e^{i\boldsymbol{k}\boldsymbol{\delta}_1} + e^{i\boldsymbol{k}\boldsymbol{\delta}_2} + e^{i\boldsymbol{k}\boldsymbol{\delta}_3} = e^{i\boldsymbol{k}\boldsymbol{\delta}_3}(1 + e^{i\boldsymbol{k}(\boldsymbol{\delta}_1-\boldsymbol{\delta}_3)} + e^{i\boldsymbol{k}(\boldsymbol{\delta}_2-\boldsymbol{\delta}_3)}) = \\
&= e^{-iak_x}(1 + e^{i\frac{3a}{2}k_x}e^{-i\frac{\sqrt{3}a}{2}k_y} + e^{i\frac{3a}{2}k_x}e^{i\frac{\sqrt{3}a}{2}k_y}) = \\
&= e^{-iak_x}(1 + e^{i\frac{3a}{2}k_x}(e^{-i\frac{\sqrt{3}a}{2}k_y} + e^{i\frac{\sqrt{3}a}{2}k_y}) \times \tfrac{2}{2}) = \\
&= e^{-iak_x}(1 + 2e^{i\frac{3a}{2}k_x}\cos\left(\frac{\sqrt{3}a}{2}k_y\right))
\end{aligned} \tag{1.4}
$$

where the product $\boldsymbol{k}\boldsymbol{\delta}$ has been made explicit using $\boldsymbol{\delta}$ coordinates [11].

Hence from (1.4)

$$
\begin{aligned}
\Delta_{\boldsymbol{k}}\Delta^*_{\boldsymbol{k}} &= [e^{-iak_x}(1+2e^{i\frac{3a}{2}k_x}\cos\Big(\tfrac{\sqrt{3}a}{2}k_y\Big)][e^{iak_x}(1+2e^{-i\frac{3a}{2}k_x}\cos\Big(\tfrac{\sqrt{3}a}{2}k_y\Big)] = \\
&= 1+4\cos(\tfrac{3a}{2}k_x)\cos\Big(\tfrac{\sqrt{3}a}{2}k_y\Big)+4\cos^2(\tfrac{\sqrt{3}a}{2}k_y)^{**} = \\
&= 3+4\cos(\tfrac{3a}{2}k_x)\cos\Big(\tfrac{\sqrt{3}a}{2}k_y\Big)+2\cos\Big(\sqrt{3}k_y\Big) = \\
&= 3+f(\boldsymbol{k})
\end{aligned}
$$

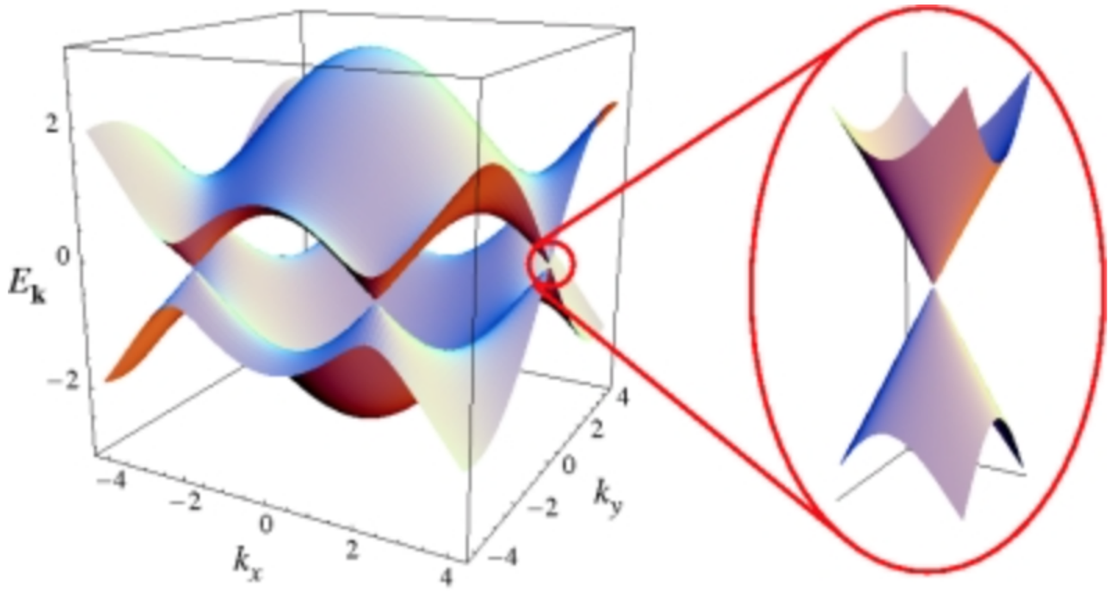

Figure 1.4: *Electronic dispersion of graphene. The figure shows a 3-D plot of the valence and conductance band of graphene, obtained solving a tight-binding model Hamiltonian with just first nearest-neighbors. The bands cross the Fermi level at the Dirac points, i.e. the six vertices of the First Brillouin Zone. (Left) Zoom of the energy bands close to one of the Dirac points. [12]*

From the second line of this expression it comes that the points at which the two

---

$$
\begin{aligned}
=&1+4\cos(\tfrac{3a}{2}k_x)\cos\Big(\tfrac{\sqrt{3}a}{2}k_y\Big)+4\cos\Big(\sqrt{3}ak_y\Big)+4\sin^2(\tfrac{\sqrt{3}a}{2}k_y) = \\
=&1+4\cos(\tfrac{3a}{2}k_x)\cos\Big(\tfrac{\sqrt{3}a}{2}k_y\Big)+4\cos\Big(\sqrt{3}ak_y\Big)+2\cos(0)-2\cos(3ak_x)
\end{aligned}
$$

energy bands touch, i.e. $\epsilon_{\boldsymbol{k}} = 0$, are set by the following conditions

$$\begin{aligned} \frac{3ak_x}{2} &= 2n\pi & \cos\left(\tfrac{\sqrt{3}a}{2}k_y\right) &= -\tfrac{1}{2} \\ \frac{3ak_x}{2} &= (2n+1)\pi & \cos\left(\tfrac{\sqrt{3}a}{2}k_y\right) &= \tfrac{1}{2} \end{aligned}$$

Within the first hexagonal Brillouin Zone there are six points (k_x, k_y) such that $\epsilon(\boldsymbol{k}) = 0$. These are exactly the loci of the six Dirac cones within the FBZ [8]. It should be noticed that, considering just nearest-neighbor hopping terms in the Hamiltonian the energy spectrum is exactly symmetric about the Dirac points ($\epsilon(\boldsymbol{k}) = 0$) and there is no gap between the two bands. This is not true anymore as soon as the second nearest-neighbor terms is counted.

1.2.2 Second nearest neighbor hoppings

Let's consider then the second term of the Hamiltonian (1.1)

$$H' = -t' \sum_{\ll i,j \gg} (a_i^\dagger a_j + b_i^\dagger b_j + h.c.)$$

moving to k-space and performing the same calculations done for H_0, the Hamiltonian can be written as

$$H' = \boldsymbol{\psi}^\dagger h'(\boldsymbol{k})\boldsymbol{\psi} \quad \longrightarrow \quad h'(\boldsymbol{k}) = -t' \begin{pmatrix} \sum\limits_{\boldsymbol{a}} 2\cos(\boldsymbol{ka}) & 0 \\ 0 & \sum\limits_{\boldsymbol{a}} 2\cos(\boldsymbol{ka}) \end{pmatrix} \tag{1.5}$$

showing that it is already in diagonal form. The $\sum\limits_{\boldsymbol{a}}$ is the summation over the lattice vectors $\boldsymbol{a}_1$, $\boldsymbol{a}_2$, $\boldsymbol{a}_3 = \boldsymbol{a}_2 - \boldsymbol{a}_1$. Thus one can now expand the cosine substituting the values of $\boldsymbol{a}_n$

$$\begin{aligned} \sum_{\boldsymbol{a}} 2\cos(\boldsymbol{ka}) &= 2[\cos\left(\tfrac{3a}{2}k_x + \tfrac{\sqrt{3}a}{2}k_y\right) + \cos\left(\tfrac{3a}{2}k_x - \tfrac{\sqrt{3}a}{2}k_y\right) + \cos\left(\sqrt{3}ak_y\right)] = \\ &= 2[2\cos\left(\tfrac{3a}{2}k_x\right)\cos\left(\tfrac{\sqrt{3}a}{2}k_y\right) + \cos\left(\sqrt{3}ak_y\right)] \end{aligned}$$

This leads to the expression

$$f'(\boldsymbol{k}) = 4\cos\left(\tfrac{3a}{2}k_x\right)\cos\left(\tfrac{\sqrt{3}a}{2}k_y\right) + 2\cos\left(\sqrt{3}ak_y\right) = f(\boldsymbol{k})$$

From this result the total energy spectrum of (1.1) is

$$E_{\pm}(\boldsymbol{k}) = \pm t\sqrt{3 + f(\boldsymbol{k})} - t'f'(\boldsymbol{k})$$

in fact (1.5) is already in diagonal form, so the $f'(\boldsymbol{k})$ gives always a negative contribution to (1.3). It follows that the energy spectrum is not symmetric about $E_{\pm}(\boldsymbol{k}) = 0$, instead the π band is lowered, while π^* is flattened around the Dirac point. Introducing the t' interaction energy, a gap cannot be opened between the Dirac cones because all the real symmetries of the system are preserved and what is broken is particle-hole symmetry. A deep analysis of the symmetries of the system will be performed in the section dedicated to the topological properties of graphene in the third chapter.

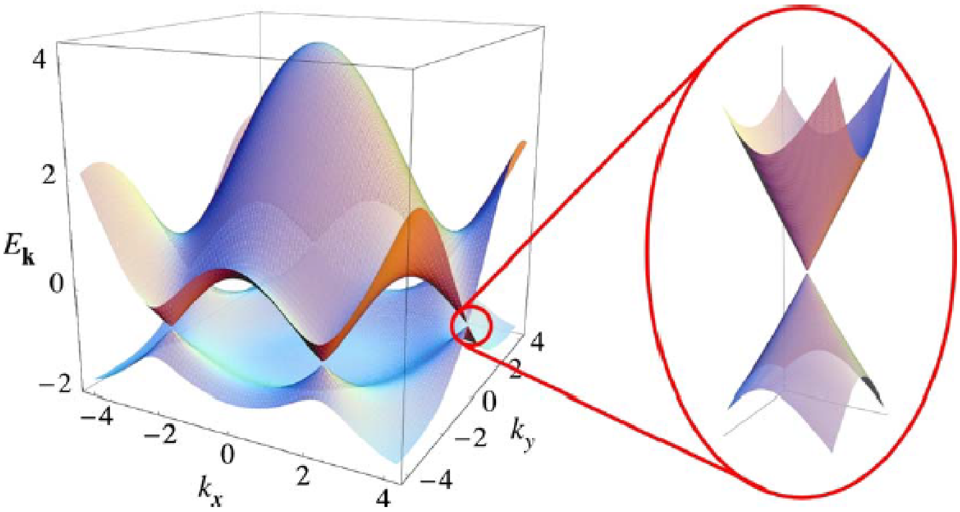

Figure 1.5: *Electronic dispersion of graphene. The figure shows a 3-D plot of the valence and conductance band of graphene, obtained solving a tight-binding model Hamiltonian with first and second nearest-neighbors. The bands cross the Fermi level at the Dirac points, i.e. the six vertices of the First Brillouin Zone. (Left) Zoom of the energy bands close to one of the Dirac points. One should notice that when second nearest-neighbors are taken into account the energy spectrum loses its symmetric behaviour about* $E_{\pm}(\boldsymbol{k}) = 0$*. Particle-hole symmetry is spoiled [9]*

1.3 DIRAC CONES AND CONTINUUM MODEL

It is interesting to analyse more in detail the behaviour of the energy spectrum where the two bands touch, i.e. close to the Dirac points. It is convenient to refer to the Hamiltonian (1.2) neglecting the second nearest-neighborhood hopping term. In order to expand close to the Dirac point $\boldsymbol{K} = \frac{2\pi}{3a}(1, \frac{1}{\sqrt{3}})$ let's introduce a 2-D vector $\boldsymbol{q}$, such that $\boldsymbol{k} = \boldsymbol{K} + \boldsymbol{q}$ with $\boldsymbol{q} \ll \boldsymbol{K}$. The Δ term (1.4) becomes

$$\begin{aligned}\Delta_{\boldsymbol{k}} = \sum_{\boldsymbol{\delta}} e^{i\boldsymbol{k}\boldsymbol{\delta}} &= e^{-iak_x}(1 + 2e^{i\frac{3a}{2}k_x}\cos\Big(\tfrac{\sqrt{3}a}{2}k_y\Big)) = \\ &= e^{-iaK_x}e^{-iaq_x}(1 + 2e^{i\frac{3a}{2}K_x}e^{i\frac{3a}{2}q_x}\cos\Big(\tfrac{\sqrt{3}a}{2}(K_y + q_x)\Big) = \\ &= e^{-iaK_x}e^{-iaq_x}(1 + 2e^{i\pi}e^{i\frac{3a}{2}q_x}\cos\Big(\tfrac{\pi}{3} + \tfrac{\sqrt{3}a}{2}q_y\Big))\end{aligned}$$

expanding to first order around $\boldsymbol{q} = 0$

$$\begin{aligned}\Delta_{\boldsymbol{k}} &= e^{-iaK_x}(1)(1 - 2(1 + \tfrac{3a}{2}q_x(\tfrac{1}{2} - \tfrac{\sqrt{3}a}{4}q_y)^{**}) = \\ &= e^{-iaK_x}(\tfrac{3a}{2}q_y - \tfrac{3a}{2}iq_x)\end{aligned}$$

[1] So the result is simply

$$\Delta_{\boldsymbol{K}+\boldsymbol{q}} = -\tfrac{3}{2}aie^{-i\frac{2\pi}{3}}(q_x + iq_y)$$

It is possible to fix a Gauge such that the phase $-ie^{-i\frac{2\pi}{3}}$ in front of the parenthesis does not appear in the equation. The Hamiltonian (1.2) becomes

$$H_0(\boldsymbol{k}) = \boldsymbol{\psi}^\dagger h(\boldsymbol{K}+\boldsymbol{q})\boldsymbol{\psi} \quad \longrightarrow \quad h(\boldsymbol{K}+\boldsymbol{q}) = \hbar v_f \begin{pmatrix} 0 & q_x + iq_y \\ q_x - iq_y & 0 \end{pmatrix} \tag{1.6}$$

In the expression of $h(\boldsymbol{K}+\boldsymbol{q})$ it has been introduced the Fermi velocity, which is defined as $v_f = \frac{3ta}{2\hbar}$.

---

[1]

$$\begin{aligned}\cos\Big(\tfrac{\pi}{3} + \tfrac{\sqrt{3}a}{2}q_y\Big)) &= \cos\Big(\tfrac{\pi}{3}\Big)\cos\Big(\tfrac{\sqrt{3}a}{2}q_y\Big) - \sin\Big(\tfrac{\pi}{3}\Big)\sin\Big(\tfrac{\sqrt{3}a}{2}q_y\Big) = \left(\frac{1}{2}\cos\Big(\tfrac{\sqrt{3}a}{2}q_y\Big) - \frac{\sqrt{3}}{2}\sin\Big(\tfrac{\sqrt{3}a}{2}q_y\Big)\right)_{\boldsymbol{q}\to 0} = \\ &= \tfrac{1}{2} - \tfrac{\sqrt{3}}{2}\tfrac{\sqrt{3}a}{2}q_y = \tfrac{1}{2} - \tfrac{\sqrt{3}a}{4}q_y\end{aligned}$$

This result can be expressed in terms of Pauli matrices,

$$h(\boldsymbol{K}+\boldsymbol{q}) = h_{\boldsymbol{K}} = \hbar v_f(\sigma_x q_x - \sigma_y q_y) = \hbar v_f \boldsymbol{\sigma}^* \boldsymbol{q} \tag{1.7}$$

where $\boldsymbol{\sigma} = (\sigma_x, \sigma_y, \sigma_z)$ and $\boldsymbol{\sigma}^* = (\sigma_x, -\sigma_y, \sigma_z)$. It follows that, diagonalizing the matrix, the energy spectrum is found to be linear in $\boldsymbol{q}$ and it depends only on the modulus of $\boldsymbol{q}$

$$E_{\pm}(\boldsymbol{k}) = \pm t\sqrt{\Delta_{\boldsymbol{K}+\boldsymbol{q}}\Delta^*_{\boldsymbol{K}+\boldsymbol{q}}} = \pm\hbar v_f|\boldsymbol{q}| \tag{1.8}$$

Thus the two energy bands are described by cones with the vertices lying at the Dirac points. Equation (1.8) in fact, characterises mass-less Dirac particles with spin $\frac{1}{2}$ and velocity $v_f \cong 10^6 m/s$. As a consequence the wave function of the Hamiltonian is given by a 2-component spinor with $\theta_{\boldsymbol{q}}$, the angle of $\boldsymbol{q}$ in momentum space with respect to the x axis

$$\boldsymbol{\psi}_{(\boldsymbol{K}),\pm}(\boldsymbol{q}) = \frac{1}{\sqrt{2}}\begin{pmatrix} e^{i\frac{\theta_{\boldsymbol{q}}}{2}} \\ \pm e^{-i\frac{\theta_{\boldsymbol{q}}}{2}} \end{pmatrix} \tag{1.9}$$

where $\theta_{\boldsymbol{q}} = tan^{-1}(\frac{q_x}{q_y})$ and ± refers to the two possible outcomes of the energy. This vector is such that the phase changes just by π when the phase of the vector $\boldsymbol{q}_x + i\boldsymbol{q}_y$ is rotated by 2π, as it should be for spinors. Nevertheless the two components of the wave-function are not referred to the two values of the spin, that has been implied since (1.1). In this case spinor components describe the distribution of the electrons in the two sub-lattices A and B, and this is why one should rather speak of pseudo-spin.

When the calculations are performed on $\boldsymbol{K'} = \frac{2\pi}{3a}(1, -\frac{1}{\sqrt{3}})$, the result for (1.4) becomes

$$\Delta_{\boldsymbol{K'}+\boldsymbol{q}} = -\tfrac{3}{2}a(q_x - iq_y)$$

with Hamiltonian

$$h_{\boldsymbol{K'}} = \hbar v_f(\sigma_x q_x + \sigma_y q_y) = \hbar v_f \boldsymbol{\sigma}\boldsymbol{q}$$

and wave-function

$$\boldsymbol{\psi}_{(\boldsymbol{K'}),\pm}(\boldsymbol{q}) = \frac{1}{\sqrt{2}}\begin{pmatrix} e^{i\frac{\theta_{\boldsymbol{q}}}{2}} \\ \pm e^{-i\frac{\theta_{\boldsymbol{q}}}{2}} \end{pmatrix}$$

Despite this result, the excitations near K and K' are not one another anti-particles. From equation (1.8) and (1.9) it is clear that the couple particle anti-particle is given respectively by the positive and negative outcomes of the energy $E = \pm\hbar v_f|\boldsymbol{q}|$. These two results come from the possible combinations of the excitations on the A and B sub-lattices near just one of the Dirac points and these are really what defines the particle anti-particle couple.

1.4 PROPERTIES OF GRAPHENE

As it was mentioned before, in graphene each atom has a p_z orbital perpendicular to the plane that is responsible for its electronic properties. It follows that within each unit cell, the two p_z orbitals form π bonding and π^* anti-bonding. The two electrons per-cell fill completely the π orbitals of the valence band, leaving empty the π^* orbitals of the conduction one. The electronic structure resembles that one of an insulator. Nevertheless at the Dirac points the two bands touch, so graphene ends up being a semi-metal. Close to these points, where the dispersion relation is linear $E_{\boldsymbol{q}} = \hbar v_f$, one can compute the density of states that is equal to the number of electronic states per unit cell area A_c and energy

$$\rho(E) = \frac{dN}{dE_{\boldsymbol{q}}} = \frac{dN}{dq}\frac{dq}{dE_{\boldsymbol{q}}} = \frac{1}{\hbar v_f}\frac{dN}{dq} = \frac{2A_c}{\pi}\frac{E}{(\hbar v_f)^2} \tag{1.10}$$

where the derivative of the number of states N

$$\frac{dN}{dq} = \frac{d}{dq}\int d^2q \frac{g}{4}\frac{A_c}{\pi^2} = \frac{d}{dq}\left(\frac{A_c}{\pi}q^2\right) = \frac{2A_c q}{\pi} = \frac{2A_c}{\pi}\frac{E}{\hbar v_f} \tag{1.11}$$

and $g = 4$ is the multiplicity, that gives a contribution of 2 for the spin and 2 for the two Dirac cones at K and K'.

From (1.10) it is clear that the density of state is symmetric about the point $E = 0$, where $\rho = 0$. Because of the linear dispersion relation in fact, $\rho(E) = \rho(-E)$ showing the electron-hole symmetry of the spectrum close to the Dirac points.

Equation (1.7) describes mass-less Dirac particle, so it is natural to introduce a cyclotron mass m^* which is defined in the semi-classical approximation as

$$m^* = \frac{1}{2\pi}\left[\frac{\partial A(E)}{\partial E}\right]_{E=E_f} \tag{1.12}$$

where $A = \pi q(E)^2 = \frac{\pi E^2}{(\hbar v_f)^2}$ is the area of an orbit enclosed by the momentum $\boldsymbol{q}$, and E_f is the Fermi energy. Substituting in (1.12) the expression for A

$$m^* = \frac{E_f}{(\hbar v_f)^2} = \frac{q_f}{\hbar v_f} \tag{1.13}$$

The electron density n, which is the number of filled states per unit volume, can be expressed in terms of the Fermi momentum $\boldsymbol{q}_f$, so from (1.11), $n = \frac{q_f^2}{\pi}$. It follows that the effective mass is

$$m^* = \frac{\sqrt{\pi n}}{\hbar v_f} \tag{1.14}$$

proportional to the $\sqrt{n}$. This result is used in experiments to proof that in graphene particles behaves as mass-less Dirac fermions close to the Dirac points [8] [9].

1.5 GAPPING DIRAC CONES

Coming back to the study of the Dirac Hamiltonian and looking at equation (1.6), one can think of adding a term proportional to σ_z. Given a generic parameter m, the Hamiltonian becomes

$$h_{\boldsymbol{K}} = \begin{pmatrix} m & \hbar v_f(q_x - iq_y) \\ \hbar v_f(q_x + iq_y) & -m \end{pmatrix} \equiv \hbar v_f(\sigma_x q_x - \sigma_y q_y) + m\sigma_z \tag{1.15}$$

This introduces an asymmetry between the two sites which should modify somehow the shape of the energy bands. Diagonalizing (1.15), the energy eigenvalues are

$$E_\pm = \pm\sqrt{(\hbar v_f|\boldsymbol{q}|)^2 + m^2}$$

From this result it is clear that there are not solutions with $E = 0$, so the two energy bands never touch.

The introduction of any asymmetry between sub-lattice A and B produces the opening of a gap between π and π^*, in such a way that the Dirac cones do not touch anymore. On the contrary, the addition of a term m proportional to the identity does not alter the shape of the Dirac cones, it just shift them of this same quantity. In this case the eigenvalues of the energy are in fact

$$E_{\pm} = v_f(m \pm |\boldsymbol{q}|)$$

that have $E_{\pm} = 0$ value for $m = \mp|\boldsymbol{q}|$

2

The effective model of TBG

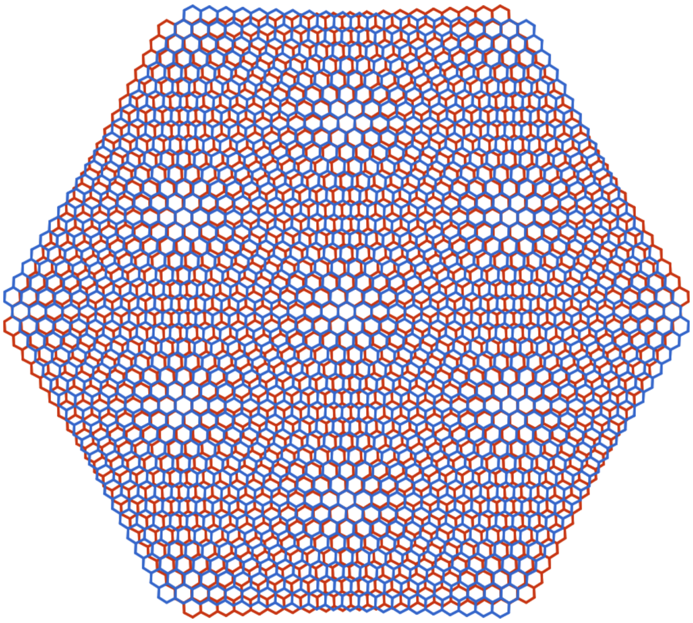

Figure 2.1: *Moiré pattern generated by two honeycomb lattices stacked one on top of the other with a certain rotation angle. [13]*

The analysis performed so far is about a 2-D single layer of graphene and its electronic properties. Many experiments have been performed in the last twenty years on graphene-based structures, meaning 0-D, 1-D or 2-D arrangements of carbon atoms on nano-structures. These can be imagined to be formed from the pristine 2-D carbon layer that is further stacked, or folded. These samples present different band-structures and transport characteristics that can be available for various carbon-based electronics.

A big contribution to this field has been the introduction of new preparation methods of multi-layer materials, that consent to create different stacking configurations with arbitrary small rotation angles. In general the lattice periods of the individual atomic layers are incommensurate, due to the misorientation between the sheets. Focusing just on a bilayer systems, the double-layers graphene configuration is particularly interesting and presents low-energy electronic properties strongly dependent on the stacking arrangement. For twist angles larger then few degrees, the two layers graphene are almost electronically isolated. On the contrary, as the angle becomes smaller, interlayer coupling strengthens and the Fermi velocity at the Dirac point begins to decrease. From the analysis of the problem performed by Allan H. MacDonald and colleagues [5], it turns out that for small angles of rotation ($\lesssim 10°$) and first order approximation at the Dirac cones, bilayer graphene presents always linear energy dispersion relation, exactly as it happens for single layer sheets. In addition to that, for what are called magic angles, Fermi velocity tends to zero at the Dirac points. It follows that, in these configurations, bilayer graphene presents extremely interesting electronic properties and phase states not yet totally explored.

Coming back to the general case and starting from a conventional stacking, the geometry of bilayer systems, which creates a Moiré pattern, is characterised by a twist angle θ and a translation vector $\boldsymbol{d}$. The commensurability depends only on the angle of rotation and a two dimensional crystal forms just for a discrete set of commensurate θ generating a Moiré periodic super-lattice. This implies that for generic angles of twist, Bloch's theorem cannot be applied and the electronic band structure of the bilayer material cannot be directly computed with usual band-theory methods.

The goal of this chapter is to retrace the solution of this problem proposed by Castro-Neto [14], MacDonald and colleagues for small angle rotation bilayer graphene and to give a first understanding of the meaning of magic angles. In particular it is shown that one can build a low-energy continuum model Hamiltonian at the Dirac points. Moreover it is allowed the construction of the electronic structure using Bloch bands even for incommensurate twist angles. It emerges that these bands depend on the numerical value of the rotation angle θ, which affects their shape [14] [5] [15] [16] [17].

2.1 THE MODEL

The low energy model of bilayer graphene close to the Dirac points, is constructed introducing just three terms:

- two Hamiltonians that describe each one of the single isolated sheet
- a tunnelling hopping matrix between the layers

The interactions between electrons are neglected similarly to the single layer case. The decoupled Hamiltonian is the one of a Dirac spinor, it has the same expression found in the previous chapter (equation (1.6)) close to $\boldsymbol{K}$ point

$$h_{\boldsymbol{k}}(\theta) = vk \begin{pmatrix} 0 & e^{i(\theta_{\boldsymbol{k}}-\theta)} \\ e^{-i(\theta_{\boldsymbol{k}}-\theta)} & 0 \end{pmatrix} \tag{2.1}$$

However the angle θ dependence is present here. It is, in fact, the rotation angle of one layer with respect to the other. $\boldsymbol{k}$ is, as before, the fluctuation in momentum at the Dirac point.

The inter-layer term is constructed considering hopping from each site in layer one to the closest sites of layer two. There is no coupling between different valleys $\boldsymbol{K}$ and $\boldsymbol{K}'$ [14]. An electronic state with a Bloch wave vector $\boldsymbol{k}$ on layer one and one with $\boldsymbol{k}'$ on layer two are coupled only when

$$\boldsymbol{k} + \boldsymbol{G}_1 = \boldsymbol{k}' + \boldsymbol{G}'_2 \tag{2.2}$$

where $\boldsymbol{G}_1$ and $\boldsymbol{G}'_2$ are reciprocal lattice vectors. This is accounted as a general Umklapp process between misoriented crystals and gives a necessary condition to find a non-zero hopping term [16]. Another remark that should be made, is that the model considered is the one of a π-band tight-binding Hamiltonian. For this model, in general, the hopping term $t(\boldsymbol{r})$ depends only on the planar projection $\boldsymbol{r}$ between two different layers sites. It follows that there is not dependence on the perpendicular distance between the sheets, nor on the nature of the hopping sub-lattice (respectively A and B) [15].

2.1.1 THE HOPPING MATRIX

The matrix hopping element between Bloch states within the two layers is defined as

$$< \Psi^{\alpha}_{\boldsymbol{k}} | H_{int} | \Psi^{\beta}_{\boldsymbol{k}'} > \tag{2.3}$$

where H_{int} is the inter-layer interacting Hamiltonian. Therefore, one should first understand how these $|\Psi^{\alpha}_{\boldsymbol{k}} >$ are constructed and how they are related.

The Bloch state for a single layer $j = 1, 2$, labelled by its momentum $\boldsymbol{k}$ and the band index n, can be written as

$$|\Psi^{(j),n}_{\boldsymbol{k}} >= a^{(j),n}_{\boldsymbol{k},A} |\psi^{(j)}_{\boldsymbol{k},A} > + a^{(j),n}_{\boldsymbol{k},B} |\psi^{(j)}_{\boldsymbol{k},B} >$$

where $a^{(j),n}_{\boldsymbol{k},\alpha}$ are the coefficients associated to each one of the two sub-lattices $\alpha = A, B$. These are referred to the result found in the previous chapter for the spinor eigenvectors $eqref\psi$ of the tight-binding Hamiltonian close to the Dirac point

$$\begin{pmatrix} a^{(j),n}_{\boldsymbol{k},A} \\ a^{(j),n}_{\boldsymbol{k},B} \end{pmatrix} = \frac{1}{\sqrt{2}} \begin{pmatrix} e^{-i\frac{\theta_{\boldsymbol{q}}}{2}} \\ \pm e^{i\frac{\theta_{\boldsymbol{q}}}{2}} \end{pmatrix}$$

The Bloch basis projected on a single sub-lattice $|\psi^{(j)}_{\boldsymbol{k},\alpha} >$, is simply defined as

$$|\psi^{(j)}_{\boldsymbol{k},\alpha} >= \frac{1}{\sqrt{N}} \sum_{\boldsymbol{R}} e^{i\boldsymbol{k}(\boldsymbol{R}+\boldsymbol{\tau}_{\alpha})} |\boldsymbol{R} + \boldsymbol{\tau}_{\alpha} > \tag{2.4}$$

where $\boldsymbol{k}$ is the two dimensional Bloch wave vector parallel to the lattice, N is the number of α sites (which is equivalent to the number of unit cells within the layer), $\boldsymbol{R}$ are the triangular Bravais lattice vectors and $\boldsymbol{\tau}_{\alpha}$ is fixed in a way that it connects the two atoms in the unit cell, meaning $\boldsymbol{\tau}_A = 0$ and $\boldsymbol{\tau}_B = \boldsymbol{\tau}$. As it was mentioned before, the second layer is rotated by a θ angle and displaced by a $\boldsymbol{d}$ vector with respect to the first one. By convention all the vectors referred to the second layer are labelled with prime $'$. It follows that $\boldsymbol{r}$ and $\boldsymbol{r}'$, and the the wave vectors $\boldsymbol{k}$ and $\boldsymbol{k}'$, are related by the transformation relations

$$\begin{aligned} \boldsymbol{r}' &= M(\theta)\boldsymbol{r} + \boldsymbol{d} \\ \boldsymbol{k}' &= M(\theta)\boldsymbol{k} \end{aligned} \tag{2.5}$$

where $M(\theta)$ is the rotation matrix. For the second layer, equation (2.4) becomes

$$|\psi^{(2)}_{\boldsymbol{k},\beta}>=\frac{1}{N}\sum_{\boldsymbol{R}'}e^{i\boldsymbol{k}(\boldsymbol{R}'+\boldsymbol{\tau}'_\beta)}|\boldsymbol{R}'+\boldsymbol{\tau}'_\beta> \tag{2.6}$$

where $\beta = A, B$.

(2.4) and (2.6) are constructed in a way that the number of unit cells in the two layers is the same (N), so the two Bloch states are simply related by

$$|\Psi^{(2),n}_{\boldsymbol{k}'}>=|\Psi^{(1),n}_{\boldsymbol{k}}>$$

with the replacements expressed in (2.5).

Coming back to equation (2.3), the matrix hopping term is

$$T^{nn'}_{\boldsymbol{k}\boldsymbol{p}'}=<\Psi^{(1),n}_{\boldsymbol{k}}|H_{int}|\Psi^{(2),n'}_{\boldsymbol{p}'}>=<\Psi^{(1),n}_{\boldsymbol{k}}|H_{int}|\Psi^{(1),n'}_{\boldsymbol{p}}> \tag{2.7}$$

where n and n' are the band indices. Substituting (2.4) and (2.6) in equation (2.7), and using the two-centre approximation

$$T^{nn'}_{\boldsymbol{k}\boldsymbol{p}'}=\frac{1}{N}\sum_{\alpha,\beta}(a^{(1),n}_{\boldsymbol{k},\alpha})^*a^{(1),n'}_{\boldsymbol{p},\beta}\sum_{\boldsymbol{R},\boldsymbol{R}'}e^{-i\boldsymbol{k}(\boldsymbol{R}+\boldsymbol{\tau}_\alpha)+i\boldsymbol{p}(\boldsymbol{R}'-\boldsymbol{d}+\boldsymbol{\tau}'_\beta)}t(\boldsymbol{R}'+\boldsymbol{\tau}'_\beta-\boldsymbol{R}-\boldsymbol{\tau}_\alpha)$$

with

$$<\boldsymbol{\tau}_\alpha+\boldsymbol{R}|H_{int}|\boldsymbol{R}'+\boldsymbol{\tau}'_\beta>=t(\boldsymbol{R}+\boldsymbol{\tau}_\alpha-\boldsymbol{R}'-\boldsymbol{\tau}'_\beta)$$

The expression for $T^{nn'}_{\boldsymbol{k}\boldsymbol{p}'}$ can be written performing a Fourier transform on $t(\boldsymbol{r})$

$$T^{nn'}_{\boldsymbol{k}\boldsymbol{p}'}=\frac{1}{N}\sum_{\alpha,\beta}(a^{(1),n}_{\boldsymbol{k},\alpha})^*a^{(1),n'}_{\boldsymbol{p},\beta}\sum_{\boldsymbol{R},\boldsymbol{R}'}\frac{1}{N}\sum_{\boldsymbol{q}}t(\boldsymbol{q})e^{-i\boldsymbol{k}(\boldsymbol{R}+\boldsymbol{\tau}_\alpha)+i\boldsymbol{p}(\boldsymbol{R}'-\boldsymbol{d}+\boldsymbol{\tau}'_\beta)}e^{i\boldsymbol{q}(\boldsymbol{R}'+\boldsymbol{\tau}'_\beta-\boldsymbol{\tau}_\alpha-\boldsymbol{R})} \tag{2.8}$$

It is convenient to work just with the second summation term of (2.8). Only this one in fact, is manipulated to find the final result

$$\begin{aligned}&\sum_{\boldsymbol{R},\boldsymbol{R}'}\frac{1}{N}\sum_{\boldsymbol{q}}t(\boldsymbol{q})e^{-i\boldsymbol{k}(\boldsymbol{R}+\boldsymbol{\tau}_\alpha)+i\boldsymbol{p}(\boldsymbol{R}'-\boldsymbol{d}+\boldsymbol{\tau}'_\beta)}e^{i\boldsymbol{q}(\boldsymbol{R}'+\boldsymbol{\tau}'_\beta-\boldsymbol{\tau}_\alpha-\boldsymbol{R})}=\\&=\sum_{\boldsymbol{R},\boldsymbol{R}'}\frac{1}{N}\sum_{\boldsymbol{q}}t(\boldsymbol{q})e^{-i\boldsymbol{k}(\boldsymbol{R}+\boldsymbol{\tau}_\alpha)}e^{i(\boldsymbol{p}+\boldsymbol{q})(\boldsymbol{R}'+\boldsymbol{\tau}'_\beta)}e^{-i\boldsymbol{p}\boldsymbol{d}}e^{-i\boldsymbol{q}(\boldsymbol{\tau}_\alpha+\boldsymbol{R})}\end{aligned} \tag{2.9}$$

Performing the Poisson summation formula with the Kronecker delta on the second layer $\boldsymbol{R}'$ and introducing $\boldsymbol{G}'_2$, which is a rotated reciprocal space vector [18]

$$\sum_{\boldsymbol{R}'} e^{i\boldsymbol{R}'(\boldsymbol{p}+\boldsymbol{q})} = N \sum_{\boldsymbol{G}'_2} \delta_{\boldsymbol{p}+\boldsymbol{q},\boldsymbol{G}'_2}$$

(2.9) becomes

$$\begin{aligned} &= \sum_{\boldsymbol{R},\boldsymbol{G}'_2} \frac{1}{N} N \sum_{\boldsymbol{q}} t(\boldsymbol{q}) e^{-i\boldsymbol{k}(\boldsymbol{R}+\boldsymbol{\tau}_\alpha)} e^{i(\boldsymbol{p}+\boldsymbol{q})\boldsymbol{\tau}'_\beta} e^{-i\boldsymbol{p}\boldsymbol{d}} e^{-i\boldsymbol{q}(\boldsymbol{\tau}_\alpha+\boldsymbol{R})} \delta_{\boldsymbol{p}+\boldsymbol{q},\boldsymbol{G}'_2} = \\ &= \sum_{\boldsymbol{R},\boldsymbol{G}'_2} t(-\boldsymbol{p}+\boldsymbol{G}'_2) e^{i\boldsymbol{G}'_2\boldsymbol{\tau}'_\beta} e^{-i\boldsymbol{p}\boldsymbol{d}} e^{i(\boldsymbol{p}-\boldsymbol{G}'_2-\boldsymbol{k})(\boldsymbol{\tau}_\alpha+\boldsymbol{R})} \end{aligned} \tag{2.10}$$

Applying again Poisson summation, but now on the first layer vector $\boldsymbol{R}$

$$\sum_{\boldsymbol{R}} e^{i(\boldsymbol{p}-\boldsymbol{G}'_2-\boldsymbol{k})\boldsymbol{R}} = N \sum_{\boldsymbol{G}_1} \delta_{\boldsymbol{p}-\boldsymbol{G}'_2,\boldsymbol{k}+\boldsymbol{G}_1}$$

equation (2.10) becomes

$$\begin{aligned} =& N \sum_{\boldsymbol{G}_1,\boldsymbol{G}'_2} t(-\boldsymbol{p}+\boldsymbol{G}'_2) e^{i\boldsymbol{G}'_2\boldsymbol{\tau}'_\beta} e^{-i\boldsymbol{p}\boldsymbol{d}} e^{i(\boldsymbol{p}-\boldsymbol{G}'_2-\boldsymbol{k})\boldsymbol{\tau}_\alpha} \delta_{\boldsymbol{p}-\boldsymbol{G}'_2,\boldsymbol{k}+\boldsymbol{G}_1} = \\ =& N \sum_{\boldsymbol{G}_1,\boldsymbol{G}'_2} t(\boldsymbol{k}+\boldsymbol{G}_1) e^{i\boldsymbol{G}'_2\boldsymbol{\tau}'_\beta} e^{-i\boldsymbol{G}'_2\boldsymbol{d}} e^{-i(\boldsymbol{k}+\boldsymbol{G}_1)\boldsymbol{d}} e^{i\boldsymbol{G}_1\boldsymbol{\tau}_\alpha} \delta_{\boldsymbol{p}-\boldsymbol{G}'_2,\boldsymbol{k}+\boldsymbol{G}_1} = \\ =& N \sum_{\boldsymbol{G}_1,\boldsymbol{G}'_2} t(\boldsymbol{k}+\boldsymbol{G}_1) e^{-i\boldsymbol{G}'_2\boldsymbol{\tau}'_\beta} e^{i\boldsymbol{G}'_2\boldsymbol{d}} e^{-i(\boldsymbol{k}+\boldsymbol{G}_1)\boldsymbol{d}} e^{i\boldsymbol{G}_1\boldsymbol{\tau}_\alpha} \delta_{\boldsymbol{p}+\boldsymbol{G}'_2,\boldsymbol{k}+\boldsymbol{G}_1} \end{aligned} \tag{2.11}$$

where in the last equality it has been set $\boldsymbol{G}'_2 = -\boldsymbol{G}'_2$ for symmetry.

The hopping term is such that, performing a Fourier transform

$$t(\boldsymbol{k}+\boldsymbol{G}_1) = \frac{1}{\Omega} \int d\boldsymbol{r}\ t(\boldsymbol{r}) e^{i\boldsymbol{r}(\boldsymbol{k}+\boldsymbol{G}_1)} \equiv \frac{1}{\Omega} t_{\boldsymbol{k}+\boldsymbol{G}_1} \tag{2.12}$$

and plugging (2.12) into (2.11) and the result so found, back to (2.8)

$$T^{nn'}_{\boldsymbol{k}\boldsymbol{p}'} = \frac{1}{\Omega} \sum_{\alpha,\beta} (a^{(1),n}_{\boldsymbol{k},\alpha})^* a^{(1),n'}_{\boldsymbol{p},\beta} \sum_{\boldsymbol{G}_1,\boldsymbol{G}'_2} t_{\boldsymbol{k}+\boldsymbol{G}_1} \delta_{\boldsymbol{p}+\boldsymbol{G}'_2,\boldsymbol{k}+\boldsymbol{G}_1} e^{-i\boldsymbol{G}'_2\boldsymbol{\tau}'_\beta} e^{i\boldsymbol{G}'_2\boldsymbol{d}} e^{-i(\boldsymbol{k}+\boldsymbol{G}_1)\boldsymbol{d}} e^{i\boldsymbol{G}_1\boldsymbol{\tau}_\alpha} \tag{2.13}$$

This result was obtained referring to [15], where the initial configuration is described by an AA stacked bilayer and the origin of vectors is at an honeycomb lattice point. It is convenient, for subsequent calculations, to refer to another article [5], where the initial configuration is an AB Bernal Stacking. The positions of the carbon atoms in the two layers are in this case related by $\boldsymbol{r}' = M(\theta)(\boldsymbol{r} - \boldsymbol{\tau}) + \boldsymbol{d}$, where $\boldsymbol{\tau}$ takes into account the initial Bernal stacking misalignment.

The hopping matrix element (2.13) is replaced with

$$\begin{aligned} T^{nn'}_{\boldsymbol{kp}'} =& \frac{1}{\Omega} \sum_{\alpha,\beta} (a^{(1),n}_{\bar{\boldsymbol{k}},\alpha})^* a^{(1),n'}_{\bar{\boldsymbol{p}},\beta} \sum_{\boldsymbol{G}_1,\boldsymbol{G}'_2} t_{\bar{\boldsymbol{k}}+\boldsymbol{G}_1} \delta_{\bar{\boldsymbol{p}}+\boldsymbol{G}'_2,\bar{\boldsymbol{k}}+\boldsymbol{G}_1} e^{-i\boldsymbol{G}_2(\boldsymbol{\tau}_\beta - \boldsymbol{\tau})} e^{-i\boldsymbol{G}'_2\boldsymbol{d}} e^{i\boldsymbol{G}_1\boldsymbol{\tau}_\alpha} = \\ =& \sum_{\alpha,\beta} (a^{(1),n}_{\bar{\boldsymbol{k}},\alpha})^* a^{(1),n'}_{\bar{\boldsymbol{p}},\beta} T^{\alpha\beta} \end{aligned} \tag{2.14}$$

where the bar notation stands for momentum computed with respect to the centre of the first Brillouin Zone.

2.1.2 THE NEW MOIRÉ PATTERN

The construction of the matrices that describe the interlayer interaction, hinges on the understanding of the geometrical structure of the bilayer. The wave vectors that figure in equation (2.14), are computed in each layer with respect to the Dirac point and are assumed to be small deviation compared to the First Brillouin wave vectors. The value of $t_{\boldsymbol{q}}$ is not exactly known. Thus, to find a numerical estimate, it has been considered the result proposed in reference [15], in which the following ansatz is made

$$t_{\boldsymbol{q}} = t_0 e^{-\alpha(\boldsymbol{q}\boldsymbol{d}_\perp)^\gamma} \tag{2.15}$$

$t_0 = 2eV\mathring{A}^2$, $\alpha = 0,13$, $\gamma = 1,25$, and $d_\perp = 3.34\mathring{A}$ is the distance between the layers. The fact that, the wave vectors in equation (2.14) are assumed to be small deviation on $\boldsymbol{K}$, is now understood. The amplitude of $t_{\boldsymbol{q}}$ in fact, bends to 0 rapidly with $\boldsymbol{q}$ defined in the Moiré first Brillouin Zone. The negative exponential $e^{-\alpha(\boldsymbol{q}\boldsymbol{d}_\perp)^\gamma}$ in equation (2.15), clearly forces $t_{\boldsymbol{q}}$ to zero for $\boldsymbol{q}\boldsymbol{d}_\perp > 1$. Given that k_D is the magnitude of the momentum at the corner of the BZ of a single layer, the biggest value $t_{\boldsymbol{q}}$ can reach is given by $|\boldsymbol{q}| \simeq k_D$. It corresponds to the three equivalent Dirac cones that are connected by reciprocal lattice vectors $\boldsymbol{G}_1^{(1)}$ and $\boldsymbol{G}_1^{(2)}$ (respectively $\mathcal{G}^{(2)}$ and $\mathcal{G}^{(3)}$ in figure (2.2)). This results in three different hopping processes.

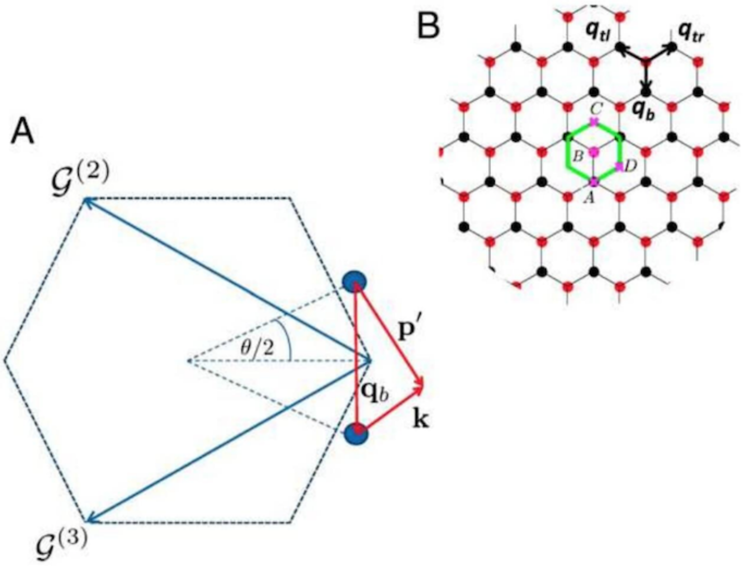

Figure 2.2: *Reciprocal-space geometry of a twisted bilayer. (A) Dashed lines locate the first Brillouin Zone of an unrotated layer, where* $\boldsymbol{G}^{(2)}$ *and* $\boldsymbol{G}^{(3)}$ *connect the three equivalent Dirac points. The blue circles are the new positions of the cones of the two stacked layers, after a rotation of* $\pm\theta/2$. *The dots are connected by the vector* $\boldsymbol{q}_b$ *of modulus* $k_\theta = 2k_D sin(\theta/2)$, *with* k_D *the magnitude of the Brillouin-zone corner wave vector of a single layer. (B) The three equivalent Dirac points in the first Brillouin zone result in three distinct hopping processes, defining a new reciprocal lattice. The green line marks the Moiré band Wigner–Seitz cell [5].*

The lattice generated by repeated translation of these hopping processes, form a new reciprocal space that one can imagine to be associated with the Moiré lattice. The Dirac cones are now identified by the vectors $\boldsymbol{q}_j$, with modulus $|\boldsymbol{q}_j| = 2k_D sin(\theta/2) = k_\theta$. This is clearly understood looking at the figure (2.2). Each layer is in fact rotated respectively of $\theta/2$ and $-\theta/2$, thus $\boldsymbol{q}/2$ is the height of the triangle with hypotenuse k_D and angle $\theta/2$. Because of momentum conservation, the interaction processes between the two layers must satisfy $\boldsymbol{k}_j = \boldsymbol{k} + \boldsymbol{q}_j$, where $\boldsymbol{k}$ is an excitation close to a Dirac point. $\boldsymbol{q}_j$ are the three vectors defined before that have modulus k_θ and identify the three tunnelling processes between the two layers at the three equivalent Dirac points $\boldsymbol{K}$. These vectors, in the following, will be labelled by $\boldsymbol{q}_b$, $\boldsymbol{q}_{tr}$, $\boldsymbol{q}_{tl}$ detecting respectively the three hopping directions $(0, -1)$, $(\frac{\sqrt{3}}{2}, \frac{1}{2})$, $(\frac{-\sqrt{3}}{2}, \frac{1}{2})$. These correspond to the three angles of rotation $\theta_{\boldsymbol{q}_1} = \frac{3\pi}{2}$, $\theta_{\boldsymbol{q}_2} = \frac{\pi}{6}$

and $\theta_{\boldsymbol{q}_3} = \frac{5\pi}{6}$. Now let's consider only the $T^{\alpha\beta}$ of the hopping expression (2.14) and perform a Fourier transform

$$T^{\alpha\beta}(\boldsymbol{r}) = \sum_{j=1}^{3} e^{i\boldsymbol{q}'_j\boldsymbol{r}} T_j^{\alpha\beta} \tag{2.16}$$

The only terms taken into account are the three $\boldsymbol{q}_j$ corresponding to the reciprocal lattice vectors $\boldsymbol{q}_b$, $\boldsymbol{q}_{tr}$, $\boldsymbol{q}_{tl}$ listed above. The other terms of the Fourier expansion in fact, are not relevant for $t_{\boldsymbol{q}}$. The three hopping matrices T_j are

$$T_1 = \frac{t_{k_D}}{\Omega}\begin{pmatrix} 1 & 1 \\ 1 & 1 \end{pmatrix} \tag{2.17}$$

$$T_2 = \frac{t_{k_D}}{\Omega} e^{-i\mathcal{G}^{(2)}\boldsymbol{d}} \begin{pmatrix} e^{-i\phi} & 1 \\ e^{i\phi} & e^{-i\phi} \end{pmatrix} \qquad T_3 = \frac{t_{k_D}}{\Omega} e^{-i\mathcal{G}^{(3)}\boldsymbol{d}} \begin{pmatrix} e^{i\phi} & 1 \\ e^{-i\phi} & e^{i\phi} \end{pmatrix}$$

The $\mathcal{G}^{(x)}$ terms are the two rotated reciprocal lattice vectors pointing at the equivalent $\boldsymbol{K}$ Dirac points in the second lattice. $t_{\boldsymbol{q}}$, in equation (2.15), has been replaced with the biggest value it can assume t_{k_D}. In fact $|\boldsymbol{k}_D| = |\boldsymbol{k}_D + \boldsymbol{G}_1|$ for every $\boldsymbol{G}_1$ reciprocal lattice vector, and from experiments for AB stacked bilayer $\frac{t_{k_D}}{\Omega} = w \approx 110meV$ [5]. The terms of the matrices are derived directly from the exponential of (2.14), so one easily finds that $\phi = \frac{2\pi}{3}$. Expression (2.16) is simply reduced to $3w\delta_{\alpha A}\delta_{\beta B}$ when $\boldsymbol{d}, \theta = 0$. This result is found directly substituting these values in (2.14) and shows that in this case the hopping term does not depend on position $\boldsymbol{r}$.

In the expression for T_j the dependence on the interlayer translation vector $\boldsymbol{d}$, can be neglected. The sliding between two layers, in fact, leads to a shift of the Moiré interference pattern that can be understood as a shift in the origin of phase space [16]. As a consequence, the dependence on $\boldsymbol{d}$ in the Hamiltonian, can be eliminated by a unitary transformation. It is convenient then to set always $\boldsymbol{d} = 0$.

This is not true anymore as soon as $\theta = 0$, in this case in fact the dependence on $\boldsymbol{d}$ cannot be neglected and the energy bands change with this vector.

2.2 THE CONTINUUM HAMILTONIAN

One can now put back together all the results found so far and try to write down the low energy Hamiltonian for the continuum model of TBG. The hopping term is local, it depends on $\boldsymbol{r}$, and it is periodic whether or not the angle of rotation is commensurate and the structure is crystalline. This consents to apply Bloch's theorem for every θ, at this level of approximation. The periodicity in fact, comes out of the local hopping process described by $\boldsymbol{q}_j$ vectors. The Fourier expansion of the hopping term (2.16), expressed as a superposition of waves vector of the reciprocal lattice, takes contributions only from the three $\boldsymbol{q}_j$ described before. It follows that $T(\boldsymbol{r})$ has the same periodicity of the lattice generated by the very $\boldsymbol{q}_j$. Referring to figure (2.2) it becomes clear that, by repeating the hopping processes, one generates a k-space honeycomb lattice whose real space identifies a Moiré pattern. It is precisely the green honeycomb in the figure that detects the Moiré Wigner-Seitz cell. Writing down the Hamiltonian in $\boldsymbol{k}$ and $\boldsymbol{k'}$ space, one can include only the single layer Hamiltonian described by equation (2.1), the three T_j hopping terms in the second layer and truncate $H_{\boldsymbol{k}}$ at the first honeycomb energy-shell of the super-lattice. The Hamiltonian then, is described by a 8×8 matrix including the sub-lattice degrees of freedom (A and B).

$$H_{\boldsymbol{k}} = \begin{pmatrix} h_{\boldsymbol{k}}(\theta/2) & T_b & T_{tr} & T_{tl} \\ T_b^{\dagger} & h_{\boldsymbol{k}_b}(-\theta/2) & 0 & 0 \\ T_{tr}^{\dagger} & 0 & h_{\boldsymbol{k}_{tr}}(-\theta/2) & 0 \\ T_{tr}^{\dagger} & 0 & 0 & h_{\boldsymbol{k}_{tl}}(-\theta/2) \end{pmatrix} \tag{2.18}$$

In this formulation one assumes that both layers are rotated of $\theta/2$ in opposite directions. This expression has been reported for conformity with MacDonald and Bistritzer, reference [5], nevertheless this clarification is irrelevant for further computations. This Hamiltonian acts on an eight-components spinor

$$\boldsymbol{\Psi} = \begin{pmatrix} \psi_0 \\ \psi_1 \\ \psi_2 \\ \psi_3 \end{pmatrix} \tag{2.19}$$

where ψ_0 refers to the first isolated layer near the Dirac point and ψ_j are related to the three momentum near $\boldsymbol{q}_j$ in the second layer.
In the equation for h_j the dependence on θ is negligible for small rotation angles. One can easily replace (2.1) with

$$h_j = vk_\theta \begin{pmatrix} 0 & e^{i\theta_{\boldsymbol{q}_j}} \\ e^{-i\theta_{\boldsymbol{q}_j}} & 0 \end{pmatrix}$$

lightening the notation. One should recall that $|\boldsymbol{q}_j| = k_\theta \; \forall \; j$ and $\theta_{\boldsymbol{q}_j}$ can assume the three rotation angles listed above. The Hamiltonian (2.18), where $\boldsymbol{k}_j = \boldsymbol{k} + \boldsymbol{q}_j$, can be written as the sum of

$$H_{\boldsymbol{k}} = H_0 + H'_{\boldsymbol{k}} \tag{2.20}$$

The first term is fixed by the condition $\boldsymbol{k} = 0$, while the second represents the k-dependence. $\boldsymbol{k}$ in fact can be considered as a fluctuation of the wave vector close to the Dirac point. Solving the Hamiltonian at leading order in the excitation, $H'_{\boldsymbol{k}}$ can be replaced with

$$H^{(1)}_{\boldsymbol{k}} = v \begin{pmatrix} \boldsymbol{\sigma}^*\boldsymbol{k} & 0 & 0 & 0 \\ 0 & \boldsymbol{\sigma}^*\boldsymbol{k} & 0 & 0 \\ 0 & 0 & \boldsymbol{\sigma}^*\boldsymbol{k} & 0 \\ 0 & 0 & 0 & \boldsymbol{\sigma}^*\boldsymbol{k} \end{pmatrix}$$

To find the elements of the matrix (2.20), one should start proving the assumption that H_0 has null energy eigenvalues

$$\begin{cases} h_0\psi_0 + T_j\psi_j = 0 \\ T_j^\dagger\psi_0 + h_j\psi_j = 0 \end{cases} \longrightarrow \begin{cases} h_0\psi_0 + T_j\psi_j = 0 \\ \psi_j = -h_j^{-1}T_j^\dagger\psi_0 \end{cases} \tag{2.21}$$

From direct calculation one finds that

$$T_j h_j^{-1} T_j^\dagger = 0$$

so multiplying on the left the second equation of (2.21) by T_j

$$T_j\psi_j = 0 \quad \longrightarrow \quad h_0\psi_0 = 0 \tag{2.22}$$

As it was mentioned before, ψ_0 is one of the two zero energy states, $\psi_0^{(1)}$ and $\psi_0^{(2)}$ of the isolated layer. Here the indices 1 and 2 are used to label the two degrees of freedom of the individual layer, namely A/B or electron/holes bands.

The two zero energy eigenstates of H_0, follow from (2.22) and the second equation of (2.21). From this result the elements of the Hamiltonian, up to leading order in $\boldsymbol{k}$, are

$$\frac{< \Psi^{(i)}|H_{\boldsymbol{k}}|\Psi^{(i)} >}{< \Psi^{(i)}|\Psi^{(j)} >} = \frac{< \Psi^{(i)}|H^{0}|\Psi^{(i)} >}{< \Psi^{(i)}|\Psi^{(j)} >} + \frac{< \Psi^{(i)}|H_{\boldsymbol{k}}^{(1)}|\Psi^{(i)} >}{< \Psi^{(i)}|\Psi^{(j)} >} \tag{2.23}$$

where Ψ are the eigenvalues of the unperturbed Hamiltonian H_0. From now on the upper indices (i) and (j) label the sub-lattice A and B.

The first term of equation (2.23) is null of course, so one is left with

$$\frac{< \Psi^{(i)}|H_{\boldsymbol{k}}|\Psi^{(i)} >}{< \Psi^{(i)}|\Psi^{(j)} >} = \frac{< \Psi^{(i)}|H_{\boldsymbol{k}}^{(1)}|\Psi^{(i)} >}{< \Psi^{(i)}|\Psi^{(j)} >} \tag{2.24}$$

The modulo of Ψ is

$$|\Psi|^2 = |\psi_0|^2 + |\psi_j|^2$$

in fact it can be set $|\psi_0|^2 = 1$, while ψ_j is such that

$$|\psi_j|^2 = \psi_j^{\dagger}\psi_j = \psi_0^{\dagger}T_j h_j^{-1\dagger} h_j^{-1} T_j^{\dagger}\psi_0$$

Using the fact that

$$h_j^{-1} = -\frac{1}{v k_\theta}\begin{pmatrix} 0 & e^{i\theta_{\boldsymbol{q}_j}} \\ e^{-i\theta_{\boldsymbol{q}_j}} & 0 \end{pmatrix} = -\frac{1}{\epsilon_\theta^2} h_j \tag{2.25}$$

it follows

$$h_j^{-1\dagger} h_j^{-1} = \mathbb{1}\frac{1}{v^2|q|_j^2}$$

leaving just

$$|\psi_j|^2 = \frac{1}{v^2|q|_j^2}\psi_0^{\dagger}T_j T_j^{\dagger}\psi_0$$

The product of the T_j terms, where the sum over j is superimposed, can be computed explicitly giving

$$\sum_j T_j T_j^{\dagger} = 6w^2\mathbb{1}$$

Finally, the modulo of Ψ is just

$$|\Psi|^2 = 1 + 6\alpha^2$$

where $\alpha = \frac{w}{v|q|_j}$.

One can compute now (2.24)

$$\begin{aligned}\frac{< \Psi^{(i)}|H^{(1)}_{\boldsymbol{k}}|\Psi^{(i)} >}{< \Psi^{(i)}|\Psi^{(j)} >} &= \frac{1}{6\alpha^2+1}\big(\Psi^{(i)\dagger}_0 h_{\boldsymbol{k}} \Psi^{(j)}_0 + \Psi^{(i)\dagger}_0 T_j h_j^{-1\dagger} h_{\boldsymbol{k_j}} h_j^{-1} T_j^\dagger \Psi^{(j)}_0\big) = \\ &= \frac{v}{6\alpha^2+1}\Psi^{(i)\dagger}_0 \big(\boldsymbol{\sigma}^*\boldsymbol{k} - \sum_j T_j h_j^{-1\dagger} \boldsymbol{\sigma}^*\boldsymbol{k} h_j^{-1} T_j^\dagger\big)\Psi^{(j)}_0\end{aligned} \tag{2.26}$$

From equation (2.25), where $\epsilon_\theta = vk_\theta$, (2.26) becomes

$$\frac{< \Psi^{(i)}|H^{1}_{\boldsymbol{k}}|\Psi^{(i)} >}{< \Psi^{(i)}|\Psi^{(j)} >} = \frac{v}{6\alpha^2+1}\Psi^{(i)\dagger}_0 \left(\boldsymbol{\sigma}^*\boldsymbol{k} - \frac{1}{(vk_\theta)^2}\sum_j T_j \boldsymbol{\sigma}^*\boldsymbol{k} T_j^\dagger\right)\Psi^{(j)}$$

where the last term of the sum is just [1]

$$\sum_j T_j \boldsymbol{\sigma}^*\boldsymbol{k} T_j^\dagger = 3w^2 \boldsymbol{\sigma}^*\boldsymbol{k}$$

Finally the result for (2.26) is

$$\frac{< \Psi^{(i)}|H^{(1)}_{\boldsymbol{k}}|\Psi^{(i)} >}{< \Psi^{(i)}|\Psi^{(j)} >} = v\left(\frac{1-3\alpha^2}{1+6\alpha^2}\right)\Psi^{(i)\dagger}_0 \boldsymbol{\sigma}^*\boldsymbol{k}\Psi^{(j)}_0 = v^*\Psi^{(i)\dagger}_0 \boldsymbol{\sigma}^*\boldsymbol{k}\Psi^{(j)}_0 \tag{2.27}$$

---

[1] Using that $\sum_j T_j T_j^\dagger = 6w^2\mathbb{1}$, it follows

$$\begin{aligned}&\sum_j T_j\sigma\boldsymbol{k}T_j^\dagger - 3\sigma\boldsymbol{k} = \sum_j T_j T_j^\dagger - 6\mathbb{1} = \sum_j T_j\sigma\boldsymbol{k}T_j^\dagger - \sum_j T_j T_j^\dagger = 3w^2\sigma\boldsymbol{k} - 6w^2\mathbb{1} = \\ &= \sum_j (T_j(\sigma\boldsymbol{k} - \mathbb{1})T_j^\dagger)^\dagger = \sum_j (3w^2(\sigma\boldsymbol{k} - 2\mathbb{1}))^\dagger \xrightarrow[\text{on the left}]{\times T_j^{-1}} \\ &\sum_j (\sigma\boldsymbol{k} - \mathbb{1})T_j^\dagger = \sum_j (3w^2 T_j^{-1}(\sigma\boldsymbol{k} - 2\mathbb{1})) \\ &\sum_j \sigma\boldsymbol{k}T_j^\dagger = \sum_j (3w^2 T_j^{-1}\sigma\boldsymbol{k} - 6w^2 T_j^{-1} + T_j^\dagger) \xrightarrow[\text{on the left}]{\times T_j} \\ &\sum_j T_j\sigma\boldsymbol{k}T_j^\dagger = \sum_j (3w^2 T_j T_j^{-1}\sigma\boldsymbol{k} - 6w^2 T_j T_j^{-1} + T_j T_j^\dagger) = 3\sum_j (T_j T_j^{-1}\sigma\boldsymbol{k}) = 3w^2\sigma\boldsymbol{k}\end{aligned}$$

Notice that the result obtained is analogous for $\sigma^*\boldsymbol{k}$

The Dirac velocity of this Hamiltonian is

$$v^* = v\frac{1-3\alpha^2}{1+6\alpha^2} \tag{2.28}$$

Equation (2.27) shows that the result obtained, has the same form of the continuum model Hamiltonian of a single layer of graphene $\epsilon^*_{\boldsymbol{k}} = v^* k$.

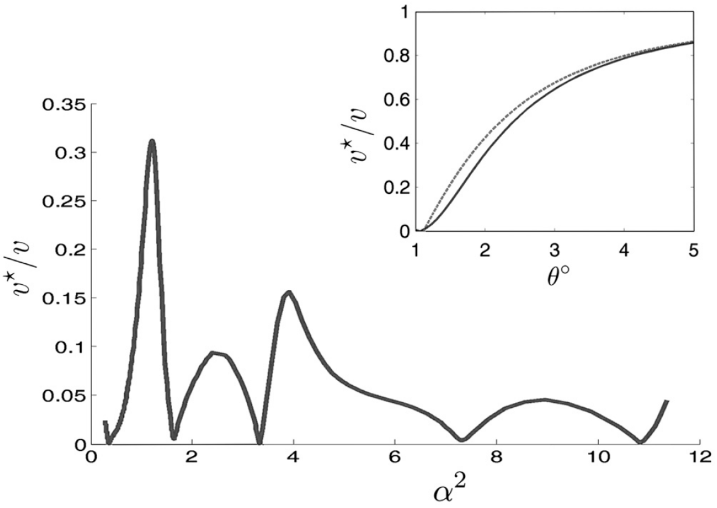

Figure 2.3: *Renormalized Fermi velocity for twisted bilayer.* v^* *is plotted as a function of* α^2, $\alpha = w/(vk_\theta)$, *for* $0.18^\circ < \theta < 1.2^\circ$. *Bigger values of* α *correspond to smaller angles. The first point where* $v^*/v = 0$, *is given by* $\alpha^2 = 1/3$ *and corresponds to the first magic angle* $\alpha^2 = 1/3$, $\theta = 1.05^\circ$. *(Inset) Renormalized velocity at larger twist angles. The solid line refers to numerical results and dashed line to analytic results based on the eight-band model [5]*

The renormalized Fermi velocity has the expression given in equation (2.28), which is different from the one found for the monolayer Dirac Hamiltonian. The fractional term $\frac{1-3\alpha^2}{1+6\alpha^2} < 1$, so v^* is always smaller then the single layer case. v^* depends on the rotation angle of the two lattices through α, which contains the $sin(\theta)$ in the denominator. As a consequence, from equation (2.28), it is possible to compute the angle for which $v^* = 0$. This is called *magic angles* and it is just the first of many others that can be found from numerical computations and occur for smaller values.

The first magic angle, computed precisely from (2.28), is $\theta = 1.05^\circ$. To find this result one should first recall that $\alpha = \frac{w}{v2k_D \sin(\theta/2)}$, so bigger values of α^2 correspond to smaller rotation angles. From (2.28) one can find $\alpha^2 = \frac{1}{3}$. Solving with the expressions for v_F and k_D (which is the modulus of $\boldsymbol{K}$ or $\boldsymbol{K}'$) and substituting the values of $t = 2,8\ eV$ [9] and $w = 0,11\ eV$, one finds exactly $\theta = 1.05°$.

The other smaller magic angles are shown in figure (2.3), exhibiting an ambiguous trend for the velocity. The inset in figure(2.3), instead, plots the trend of the velocity as a function of the rotation angle for analytic (dashes line) and numerical results (solid line) [5]. The only visible magic angle is $\theta = 1.05°$, revealing a monotonic behaviour for v^*/v which is totally lost for smaller θ.

2.2.1 The band structure

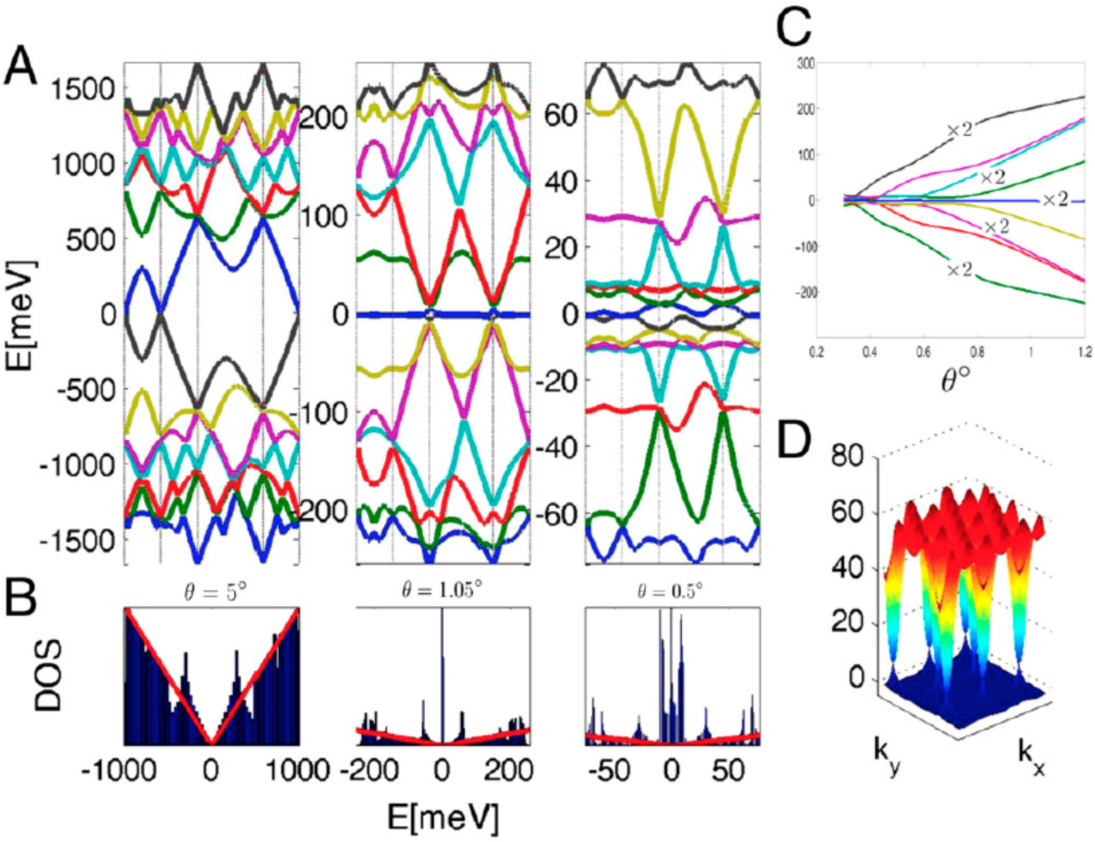

Figure 2.4: *Moiré bands. (A) Band structure in the continuum model for the 14 bands closest to the Dirac points plotted along the k-space trajectory* $A \to B \to C \to D$ *(2.2). Three different rotation angles* θ*, show different energy dispersion. In particular the second figure represents the magic angle configuration with the two flat bands at 0 energy. (B) These are the corresponding plot of the density of states. (C) It is the plot of the energy as a function of twist angles for the* $\boldsymbol{k} = 0$ *states. It shows that the band separation decreases with the rotation angle* θ*. (D) Full dispersion of the flat bands at the magic angle* $\theta = 1.05°$

To get a better understanding of what happens for small twist angles, it is convenient to analyse the graph in figure (2.4). These plots, together with (2.3), were obtained by McDonald and colleagues [5]. The figures (2.4) A, show the energy dispersion for the 14 bands closer to the Dirac points for the three different angles of twist $\theta = 5°$, $\theta = 1.05°$ and $\theta = 0.5°$ (only the second one is "magic"). The bands are plotted following the line A→B→C→D in figure (2.2), meaning their shape along the Moiré band Wigner-Seitz cell (green honeycomb cubicle in the figure (2.2) B). These band structures are recovered throughout numerical calculations. It is sufficient, in fact, to include in the computations of the bilayer Hamiltonian, not just the three summation values of equation (2.16), but higher order terms. It is clear now that formally, the effective model corresponds to an infinite-band problem for each valley [19]. From figure (2.4) A, one can neatly see that, as the twist angle is reduced, the number of bands in a given energy range increases and the bands at the Dirac points flatten. In particular, at the magic angle $\theta = 1.05°$ the two bands closer to charge neutrality, are almost totally flat and even though it is not visible from the picture, they are well separated from the other bands.

The fact that only a certain number of terms are considered in the construction of these bands, implies that the plot in (2.4) A is just an approximation. Nevertheless it is sufficiently accurate even far away from the Dirac points. This is a consequence of the way the Brillouin Zone was constructed. Recalling figure (2.2) B, the relevant hopping processes within the two bands, $\boldsymbol{q}_j$, are the very vectors that define the FBZ of "super-lattice" and its unit-cell. Thus the band structure in (2.4) A is referred to this fictitious Moiré periodic super-lattice and this is why it can be considered an accurate plot.

The geometry of the Brillouin zone of the "super-lattice", implies that the states near the Dirac points in either layer couple only to the states of energies vk_θ. This is the main difference with respect to the unrotated case in which the Dirac points, of both layers, occur at the same momentum and the inter-layer hopping couples two doublets of zero energy states [14]. For twisted graphene instead, the doublet ($\psi_0^{(1)}$ and $\psi_0^{(2)}$, defined by (2.22)), couples to three pairs of states at energy vk_θ.

For big angles of rotation the two structures behaves as isolated layers, for small angles, instead, the coupling just described implies the persistence of the Dirac cones. These can be shifted (second image of figure (2.4) A) or lifted (third image of figure (2.4) A) depending on θ and the fluctuations in $\boldsymbol{k}$.

3

TOPOLOGY OF MONOLAYER GRAPHENE

Classically matter is characterised by states such as liquid, solid and so on. Nevertheless there are many other phases that are intensively studied by condensed matter physics and go far behind the classical ones. Quantum theory predicts the existence of states such as superconductivity, ferromagnetism, Bose-Einstein condensation and many others that are defined by symmetry breaking properties. More in detail, these are described throughout the mechanism of spontaneous symmetry breaking (SSB), which is studied by Ginzburg-Landau theory. In this sense, a phase transition occurs when a symmetry is broken and a local order parameter, with observable consequences, acquires an expectation finite value. The order of the transition (first, second and so on) depends on the higher coefficient of the expansion of the free energy in the order parameter, meaning the value for which it vanishes.

In the last twenty years other kinds of phases of matter have been intensively studied, namely topological ones. These are states with non-local order parameters that cannot be described by Ginzburg-Landau theory, giving rise to a new research field. This originated from the discovery of the Quantum Hall Effect (QHE) in 1980, in which electrons confined to two dimensions acquire a quantized conductance in the presence of a perpendicular magnetic field. This state is characterised by no SSB and no variations with smooth changes in the system parameters, but it is classified by topological order.

With topological phases of matter, one refers to phases that do take into account symmetry in their classification, but phase transitions occur even without breaking it. The label topological implies the existence of a bulk invariant, usually an integer, that changes within two different phases that present the same symmetry. To understand how these invariants are constructed and what is their meaning, one should first define the set up.

Given two Hamiltonians, $H_{(1)}$ and $H_{(2)}$ at zero temperature and dependent on a parameter $\boldsymbol{R}$, if one of them can be continuously deformed into the other, the two are topologically equivalent. One can restrict to systems with an energy gap, meaning with a gap between the ground and the first excited state. This implies that now connecting the two Hamiltonians with a continuous transformation is not trivial. In this case $H_{(1)}$ and $H_{(2)}$ are said to be topologically equivalent if the transition happens without ever closing the gap. In this case one says that it is the ground state of the two systems that is in the same topological phase. Here it comes the concept of topological invariant. It is a number that cannot change under continuous transformations classifying all quantum Hamiltonians according to its value. In this way one creates classes of Hamiltonians which are all topologically equivalent. At this point it is clear that the invariance under smooth transformations, implies that topology refers to global properties of the system.

Since the systems described have a gap in their spectrum, they are identified as insulators. What makes them topological are particular configurations of the band structure, such as the appearance of gap-less edge states. As a consequence these systems are described by a *topological band theory* characterised by those invariants appointed before, which are for example the *Chern number* and the *Berry phase*. Restricting only to systems with non-interacting fermions and considering translational invariance, one can apply Bloch's theorem and find the eigenstates of the corresponding Bloch Hamiltonians, where the fully filled bands will be separated by a gap from the empty ones. It is clear that the periodicity of the lattice space implies that one of the reciprocal lattice, so that crystal momenta lies in a periodic Brillouin zone. These clarifications about *topological band theory* are relevant for the subsequent computations of topological invariants and the analysis of the band structure in the topological phases.

To conclude this brief introduction, one should recall that topological insulators can be classified using their symmetries, in particular time-reversal, particle-hole (charge conjugation) and chiral symmetry. These are important because they lead to particular and different behaviours of the ground states. [20] [21]

3.1 TOPOLOGICAL INVARIANTS

The Berry phase was initially introduced to study the general idea of adiabatic transport. Only later on, it was realised the importance of this concept in the studying of Bloch periodic systems. It became clear that Berry phase is one of the most important ingredients of topological band theory.

Let's consider an Hamiltonian $H(\boldsymbol{R})$, which depends on time through the parameter $\boldsymbol{R}(t)$, and consider its adiabatic evolution along a closed path C, such that $\boldsymbol{R}(0) = \boldsymbol{R}(T)$. The adiabatic evolution is defined by the *Adiabatic Theorem*, which states that a quantum mechanical system subjected to gradually changing external conditions, adapts its functional form. This means that the system remains in its instantaneous eigenstate if a given perturbation is acting on it slowly enough and if there is a gap between the eigenvalue and the rest of the Hamiltonian spectrum [22]. At the end of this slow deformation along the closed path $\mathcal{C}$, the wave functions gain two terms, the first one is a dynamical phase, the second is the Berry phase. To obtain their mathematical expression, one should first introduce an instantaneous orthonormal basis for the instantaneous eigenstates $|n(\boldsymbol{R})\rangle$ of $H(\boldsymbol{R})$. Hence the Hamiltonian is diagonalized for each value of $\boldsymbol{R}$. It follows that the basis is defined by

$$H(\boldsymbol{R})\,|n(\boldsymbol{R})\rangle = E_n(\boldsymbol{R})\,|n(\boldsymbol{R})\rangle$$

up to a phase. Thus $|n(\boldsymbol{R})\rangle$ is not unique and one can make a Gauge choice in such a way that, along $\mathcal{C}$, the phase θ of the basis is single valued and smooth.

In the following, it will be shown that this is not always possible. The initial eigenstate $|n(\boldsymbol{R}(0))\rangle$ will evolve with the Hamiltonian throughout the process into $|n(\boldsymbol{R}(T))\rangle$. During the adiabatic evolution the phase $\theta(t)$ is the only degree of freedom, so that the state is $|\psi(t)\rangle = e^{-i\theta(t)}\,|n(\boldsymbol{R}(t))\rangle$ and its time evolution is given by

$$H(\boldsymbol{R})\,|\psi(t)\rangle = i\hbar\frac{d}{dt}\,|\psi(t)\rangle \tag{3.1}$$

Assuming that the states are normalized $\langle n(\boldsymbol{R}(T))|n(\boldsymbol{R}(T))\rangle = 1$, one can obtain the expression for θ translating (3.1) into a differential equation [20]

$$\theta = \frac{1}{\hbar}\int_0^T E_n(\boldsymbol{R}(t'))dt' - i\int_0^T \langle n(\boldsymbol{R}(t'))|\frac{d}{dt'}|n(\boldsymbol{R}(t'))\rangle\, dt' = \frac{1}{\hbar}\int_0^T E_n(\boldsymbol{R}(t'))dt' - \gamma_n \tag{3.2}$$

The dynamical phase, which is the first integral in equation (3.2), can be removed by a Gauge transformation while the Berry phase γ_n cannot. To understand why γ_n cannot be removed and what is its physical meaning, it is convenient to rewrite it making implicit the dependence on time. Hence

$$\begin{aligned}\gamma_n &= i\int_0^T \langle n(\boldsymbol{R}(t'))|\boldsymbol{\nabla_R}|n(\boldsymbol{R}(t'))\rangle\,\frac{d\boldsymbol{R}}{dt'} = \\ &= i\oint_{\mathcal{C}} \langle n(\boldsymbol{R}|\boldsymbol{\nabla_R}|n(\boldsymbol{R})\rangle\, d\boldsymbol{R} = \\ &= \oint_{\mathcal{C}} A_n(\boldsymbol{R})d\boldsymbol{R}\end{aligned} \tag{3.3}$$

The Berry phase is then a path integral on the parameter space and it represents a *geometrical phase* whose value depends on the path $\mathcal{C}$ but not on how it is performed in time. The term

$$A_n(\boldsymbol{R}) = i\,\langle n(\boldsymbol{R})|\boldsymbol{\nabla_R}|n(\boldsymbol{R})\rangle \tag{3.4}$$

is a vector potential in analogy with the transport of an electron in an EM field. (3.4) is called *Berry connection* or *Berry potential* and it is defined in such a way that the Berry phase is real.

The Berry potential is a Gauge dependent quantity. For $|n(\boldsymbol{R})\rangle \to e^{i\zeta(\boldsymbol{R})}\,|n(\boldsymbol{R})\rangle$ one finds $A_n(\boldsymbol{R}) \to A_n(\boldsymbol{R}) - \nabla_{\boldsymbol{R}}\zeta(\boldsymbol{R})$ with $\zeta(\boldsymbol{R})$ a smooth, single-valued function. The Berry phase then acquires an extra term as well

$$\gamma_n \to \gamma_n - \oint_{\mathcal{C}} \zeta(\boldsymbol{R})d\boldsymbol{R} = \gamma_n + \zeta(\boldsymbol{R}(0)) - \zeta(\boldsymbol{R}(T)) \tag{3.5}$$

After the closing of the path, one expects that the basis comes back to its original value. So $e^{i\zeta(\boldsymbol{R}(0))}\,|n(\boldsymbol{R}(0))\rangle = e^{i\zeta(\boldsymbol{R}(T))}\,|n(\boldsymbol{R}(T))\rangle = e^{i\zeta(\boldsymbol{R}(T))}\,|n(\boldsymbol{R}(0))\rangle$. This implies that

$$\zeta(\boldsymbol{R}(0)) - \zeta(\boldsymbol{R}(T)) = 2\pi m \tag{3.6}$$

with m an integer. Thus on a close path, the Berry phase is a Gauge invariant quantity and it cannot be removed unless γ_n is an integer itself.

One can define a Gauge field tensor from the Berry potential such that

$$(V_n(\boldsymbol{R}))_{ij} = \frac{\partial}{\partial_i}(A_n(\boldsymbol{R}))_j - \frac{\partial}{\partial_j}(A_n(\boldsymbol{R}))_i \tag{3.7}$$

which is called *Berry curvature*. Considering now a 3-D parameter space, such that $\boldsymbol{R} = (R_x, R_y, R_z)$, equation (3.7) recasts into

$$\boldsymbol{V}_n(\boldsymbol{R}) = \boldsymbol{\nabla}_{\boldsymbol{R}} \times A_n(\boldsymbol{R}) \tag{3.8}$$

Stokes' theorem can be applied to equation (3.3). γ_n becomes

$$\gamma_n = i\int < \nabla n(\boldsymbol{R})| \times |\nabla n(\boldsymbol{R}) > d\boldsymbol{\mathcal{S}} = \int (\boldsymbol{\nabla}_{\boldsymbol{R}} \times A_n(\boldsymbol{R}))d\boldsymbol{\mathcal{S}} = \int \boldsymbol{V}_n(\boldsymbol{R})d\boldsymbol{\mathcal{S}} \tag{3.9}$$

From this formulation, Berry curvature can be viewed as the magnetic field in the parameter space. It is in fact the curl of the Berry vector potential $A_n(\boldsymbol{R})$.

Making use of the equality [23]

$$\langle m|\nabla n\rangle = \frac{\langle m|(\nabla_{\boldsymbol{R}} H(\boldsymbol{R}))|n\rangle}{E_n - E_m}$$

one can find a manifestly Gauge independent expression for the Berry phase that contains the derivatives of the Hamiltonian and not that one of the wave function.

Equation (3.3) becomes

$$\gamma_n = i\int \sum_{m\neq n} \frac{\langle n(\boldsymbol{R})|\nabla_{\boldsymbol{R}} H(\boldsymbol{R})|m(\boldsymbol{R})\rangle \times \langle m(\boldsymbol{R})|\nabla_{\boldsymbol{R}} H(\boldsymbol{R})|n(\boldsymbol{R})\rangle}{(E_n - E_m)^2} d\boldsymbol{\mathcal{S}}$$

From this expression one finds out that, given that with the adiabatic approximation the dynamic of the system has been restricted to the first *n-th* level of the energy, the Berry curvature can be thought as the interaction of $|n\rangle$ with the other $|m\rangle$ states that have been projected out. Thus the Berry curvature sums up to zero if one adds all the filled bands, $\sum_n (V_n(\boldsymbol{R}))_{ij} = 0\ \forall\ \boldsymbol{R}$.

Another property of γ_n is that it consents to classify degeneracies. In fact, if two energy levels are such that $E_n - E_m \approx 0$ for some $\boldsymbol{R}$, this point corresponds to a monopole in parameter space. The degeneracy points act as sources and drains of the Berry curvature flux. Integrating the Berry curvature over a closed manifold, one finds a quantized number which is equal to the number of monopoles inside it times 2π. This is called Chern number [20][23].

All the analysis performed so far can now be applied to crystals, meaning structures that are described by a periodic lattice and can be studied with the support of Bloch's theorem. In this case the Bloch Hamiltonian depends on the crystal momentum $\boldsymbol{k}$, not on a generic parameter $\boldsymbol{R}$ and parameter space can be replaced with the first Brillouin zone. It follows that equation (3.3) can be expressed as a function of $\boldsymbol{k}$

$$\gamma_n = i \oint_{\mathcal{C}} \langle n(\boldsymbol{k}) | \boldsymbol{\nabla}_{\boldsymbol{k}} | n(\boldsymbol{k}) \rangle \, d\boldsymbol{k}$$

where $\mathcal{C}$ is a closed path in momentum space.

The Berry phase and curvature depend strongly on the dimensionality of the system and on its electronic properties (metal or insulator). Since the Berry phase is the integral of the Berry potential over a closed curve, for 1-D systems with filled bands (insulators), $\mathcal{C}$ can be the Bloch momentum defined in the FBZ from $-\pi \leq k_x \leq \pi$.

For 2-D metals the integration is performed over 1-D Fermi surfaces. On the other hand, since the Berry curvature is integrated over a manifold, for 3-D metals one can integrate over the 2-D Fermi surface.

For 2-D materials with filled bands (insulators), the surface of integration can be the full Brillouin Zone. In this case, the resulting number is related to the Hall conductance and it is identical to the Chern number of the filled bands. One should recall that the FBZ can be mapped into a torus, which is a boundless manifold. So applying the Stokes' theorem to the calculation of the Chern number, one reduces to the integral of the Berry potential $A_n(\boldsymbol{R})$ over the boundary of a boundary-less surface. It follows that, if the Chern number is not null there is not a global Gauge that is continuous and single valued and that can be defined over the entire Brillouin zone [20].

3.2 GRAPHENE

The Hall Conductance is a topological quantity that is not affected by small changes in the energy of the occupied bands, but it is just dependent on its eigenstates. Applying a magnetic field on an insulator with periodic boundary conditions, it appears a Hall conductance even in the presence of a gapped band structure. This is explained by the occurrence of gap-less edge modes that connect the two separated valence and conductance bands. Even though the system is a bulk insulator, it can transport electrons having a Hall conductance different from zero and it behaves as a metal at the boundaries. This double nature of the system reflects in what is called *bulk-edge correspondence*, meaning the topological invariants associated to the bulk and to the edges have the same value. The sum of the Chern numbers C_n of the filled bands in fact, is equal to the number of edge modes in the gap. Usually it is the presence of these edge states that determines the topological nature of an insulator, meaning its triviality or non-triviality. It is clear that there must be a connection between a non-null Chern number and the detection of a Hall conductivity in the sample. This is expressed by TKNN formula [24]

$$\sigma_{xy} = \frac{e^2}{2\pi\hbar}\sum_n C_n \;\rightarrow C = \frac{1}{2\pi}\int_{FZB=torus} dk_x dk_y V(k)_{xy} \tag{3.10}$$

where σ_{xy} is the Hall conductivity and the sum in the second equation is over n, the filled bands. Recalling that, the integral of the Berry curvature over a closed manifold is equal to the number of monopoles inside it, for a non-zero Chern number it is impossible to define a smooth Gauge on the entire torus. One must pick different phases convention inside the regions that surround the monopoles and the integration over the full torus will be split into different patches. The result then, gives the winding numbers of the Gauge transformations on the boundaries of the patches. Thus, another way to picture C_n is as the sum of all the vorticities (windings) inside the Brillouin Zone. This is a quantity that is always conserved.

It can happen that a system presents Hall conductivity even without applying an external magnetic field, showing Quantum Anomalous Hall Effect (QAHE). These structures are called Chern insulators and the first model presented to describe them was *Haldane model.* This was invented in 1988 by Duncan Haldane to explain QAHE in the presence of Bloch band structure and time reversal broken symmetry. It was first introduced for graphene lattice structures and then generalised to time reversal invariant topological insulators.

The focus of this chapter will be the understanding of graphene from a topological point of view and the study of how the shape of its bands changes modifying the symmetries of the Hamiltonian.

From the study of graphene in the first chapter, one should recall that this material presents a band structure characterised by the presence of Dirac cones. Close to this points, electrons behave as mass-less Dirac particles with Fermi velocity v_f. It follows that graphene is a semi-metal with the valence and conductance bands that touch for the simple tight-binding model Hamiltonian. One can discuss the robustness of the Dirac points once perturbations are applied and its symmetries are broken.

3.2.1 GRAPHENE SYMMETRIES

The two main symmetries that prevent Dirac cones from being altered by small perturbations are time-reversal and inversion symmetry. The first one consists in the exchange of the two inequivalent Dirac cones, sending $\boldsymbol{K}$ into $\boldsymbol{K}'$.

Time reversal acts inverting the sign of time, $\boldsymbol{k} \to -\boldsymbol{k}$. Thus one expects that $h(\boldsymbol{k}) \to h(-\boldsymbol{k})$. On the other hand, the expressions for the Hamiltonian at the Dirac points are

$$\begin{aligned} \tilde{h}(\boldsymbol{K}+\boldsymbol{k}) =& \hbar v_f h(\boldsymbol{k}) = \hbar v_f \boldsymbol{\sigma}^* \boldsymbol{k} \\ \tilde{h}(\boldsymbol{K}'+\boldsymbol{k}) =& \hbar v_f h'(\boldsymbol{k}) = \hbar v_f \boldsymbol{\sigma} \boldsymbol{k} \end{aligned} \tag{3.11}$$

Time reversal on Pauli matrices acts as complex conjugation

$$\mathcal{T} : (\sigma_x, \sigma_y, \sigma_z) \to (\sigma_x, -\sigma_y, \sigma_z)$$

It follows that the operator $\mathcal{T}$ can be expressed

$$\mathcal{T} = \sigma_0 \mathcal{K}_c$$

where $\mathcal{K}_c$ is the complex conjugation operator and $\mathcal{T}^2 = 1$ for Hamiltonians that describe particles with zero physical spin [25] [26].

From this outcomes, the first expression of (3.11) $h(\boldsymbol{k}) = (k_x\sigma_x - k_y\sigma_y)$, transforms

$$\mathcal{T}h(\boldsymbol{k})\mathcal{T}^{-1} = h(-\boldsymbol{k}) \rightarrow h(-\boldsymbol{k}) = h(\boldsymbol{k})^*$$

$$\Downarrow$$

$$\mathcal{T}h(\boldsymbol{k})\mathcal{T}^{-1} = (-k_x\sigma_x + k_y\sigma_y) = h(-\boldsymbol{k}) = h^*(\boldsymbol{k}) = (k_x\sigma_x - k_y\sigma_y)^* = (k_x\sigma_x + k_y\sigma_y) \tag{3.12}$$

So

$$\mathcal{T}h(\boldsymbol{k})\mathcal{T}^{-1} = h'(\boldsymbol{k})$$

The equalities in (3.12) become clear if one takes into account the correspondence between Dirac cones, figure (3.1) b), [20].

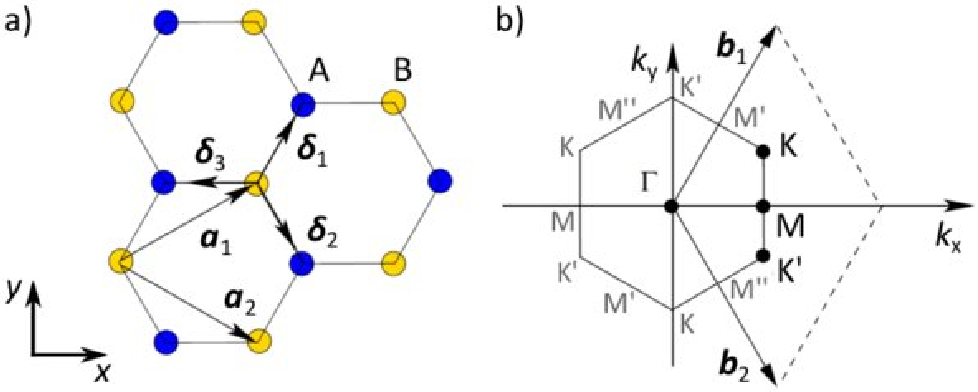

Figure 3.1: *Honeycomb lattice and its Brillouin zone. (a) is the lattice structure of graphene, with δ_1, δ_2 and δ_3 the thee vectors connecting nearest-neighborhood sites, and $\boldsymbol{a}_1$ and $\boldsymbol{a}_2$ the two basis lattice vectors. (b) represents the first Brillouin Zone with the two inequivalent Dirac cones $\boldsymbol{k}$ and $\boldsymbol{K'}$ in alternate positions. $\boldsymbol{b}_1$ and $\boldsymbol{b}_2$ are the two reciprocal basis vectors [9]*

The other important symmetry of the honeycomb lattice, is inversion $\mathcal{I}$. It switches the sub-lattice A and B. The action of the operator $\mathcal{I}$ on Pauli matrices is

$$\mathcal{I} : (\sigma_x, \sigma_y, \sigma_z) \rightarrow (\sigma_x, -\sigma_y, -\sigma_z) \tag{3.13}$$

So it can be represented by

$$\mathcal{I} = \sigma_x$$

Acting on the Dirac spin-less Hamiltonian (3.11), one finds

$$\mathcal{I}h(\boldsymbol{k})\mathcal{I}^{-1} = \sigma_x(k_x\sigma_x - k_y\sigma_y)\sigma_x = (k_x\sigma_x + k_y\sigma_y) = h'(\boldsymbol{k}) = h(-\boldsymbol{k}) \tag{3.14}$$

The equalities become clear referring to figure (3.1) b).

Inversion and time reversal look very similar but their different behaviour comes clear when a term proportional to σ_z is added to the Hamiltonian.

Considering $\mathcal{T}$ and $\mathcal{I}$ separately, Dirac cones are not preserved. It is, in fact, their combination that is the true symmetry that does not allow the system from opening a gap at $\boldsymbol{K}$ and $\boldsymbol{K}'$. This becomes clear studying what happens to the band structure of graphene adding terms to the Hamiltonian that spoil $\mathcal{T}$ and $\mathcal{I}$ separately.

It is always possible to introduce a mass term of the form $m\sigma_z$ in such a way that (3.11) becomes

$$h(\boldsymbol{k}) = k_x\sigma_x - k_y\sigma_y + m\sigma_z \tag{3.15}$$

This term breaks sub-lattice (inversion) symmetry, assigning opposite on-site energy to A and B, respectively m and $-m$. As a consequence the spectrum is gapped and Dirac cones are not preserved

$$E_{\pm}(\boldsymbol{k}) = \pm\sqrt{|\boldsymbol{k}|^2 + m^2} \rightarrow \Delta E = 2m \tag{3.16}$$

This mass is usually called *Semenoff mass* and it appears in structures that presents different sub-lattice atoms.

It is possible to add a mass term in the Hamiltonian that respects inversion but not time-reversal. Let's try again with a mass proportional to σ_z. From inversion, $\sigma_x h(-\boldsymbol{k})\sigma_x = h(\boldsymbol{k})$, meaning

$$\sigma_x h(-\boldsymbol{k})\sigma_x = \begin{pmatrix} -m(-\boldsymbol{k}) & -k_x + ik_y \\ -k_x - ik_y & m(-\boldsymbol{k}) \end{pmatrix} = h(\boldsymbol{k}) = \begin{pmatrix} m(\boldsymbol{k}) & k_x + ik_y \\ k_x - ik_y & -m(\boldsymbol{k}) \end{pmatrix}$$

One finds that m must satisfy

$$m(-\boldsymbol{k}) = -m(\boldsymbol{k}) \tag{3.17}$$

so it must be momentum-dependent. Adding this mass term to (3.11), one finds

$$\begin{aligned} \boldsymbol{K} &\longrightarrow \; h(\boldsymbol{k}) = k_x\sigma_x - k_y\sigma_y + m(\boldsymbol{k})\sigma_z \\ \boldsymbol{K}' &\longrightarrow h'(\boldsymbol{k}) = h(-\boldsymbol{k}) = k_x\sigma_x + k_y\sigma_y - m(\boldsymbol{k})\sigma_z \end{aligned} \tag{3.18}$$

From this result one can see that the term (3.17) breaks time reversal. $\boldsymbol{K}$ is not mapped to $\boldsymbol{K}'$ anymore.

To have both $\mathcal{T}$ and $\mathcal{I}$ preserved, a mass proportional to σ_z cannot be in the Hamiltonian and the small perturbations allowed are terms proportional to σ_x and σ_y (and the identity of course). The fact that, upon small perturbation, the Chern number does not change and the two poles are preserved, follows from the requirement that time reversal and inversion must be *robust symmetries*. One finds that the two Dirac cones, as long as they remain gap-less, carry a vortex giving a Berry phase equal to $\pm\pi$. $\boldsymbol{K}$ and $\boldsymbol{K}'$ are in fact the two poles where the two bands touch. For a generic gap-less Dirac Hamiltonian of the form $H(\boldsymbol{k}) = k_i\mathcal{A}_{ij}\sigma_j$, the Berry phase is equal to

$$\int_{FS} d\boldsymbol{k}A(\boldsymbol{k}) = \pi sign(det\mathcal{A})$$

[20]. The integration is performed over the Fermi surface and $\mathcal{A}$ is a 2×2 matrix. For $\boldsymbol{K}$, one has $\mathcal{A}_{11} = 1$ and $\mathcal{A}_{22} = -1$, while for $\boldsymbol{K}'$, $\mathcal{A}_{11} = 1$ and $\mathcal{A}_{22} = 1$. It follows that $det\mathcal{A}(\boldsymbol{K}) = -1$, giving a Berry phase negative, while for $det\mathcal{A}(\boldsymbol{K}') = -1$ the Berry phase is positive.

It can be concluded that time reversal and inversion protect Dirac cones only locally, preventing from the opening of a gap. There is another interesting symmetry, namely C_3, that makes Dirac cones globally stable. It prevents, in fact, $\boldsymbol{K}$ and $\boldsymbol{K}'$ from changing position within the Brillouin Zone. C_3 is a rotational symmetry, it allows the system to be invariant under a turning of $\frac{2\pi}{3}$ about the centre of one of the hexagon cells or the vertices A/B. It follows that under C_3 the hopping matrix elements must be invariant under the cyclic permutation of $\boldsymbol{\delta}_1 \rightarrow \boldsymbol{\delta}_2 \rightarrow \boldsymbol{\delta}_3$ (with $\boldsymbol{\delta}_x$ n.n. vectors given in chapter 1). Under C_3 the hopping parameters are equal for the three nearest-neighbor hoppings.

The position of the two gap-less Dirac cones, for a n.n. Hamiltonian with either time reversal, inversion and C_3 symmetry (chapter 1), is given by the values of $\boldsymbol{k}$ for which

$$(1 + e^{i\boldsymbol{k}\boldsymbol{a}_1} + e^{i\boldsymbol{k}\boldsymbol{a}_2}) = 0 \tag{3.19}$$

It is derived from the off-diagonal term of the Hamiltonian $-t(e^{i\boldsymbol{k}\boldsymbol{\delta}_1} + e^{i\boldsymbol{k}\boldsymbol{\delta}_2} + e^{i\boldsymbol{k}\boldsymbol{\delta}_2}) = -te^{i\boldsymbol{k}\boldsymbol{\delta}_1}(1 + e^{i\boldsymbol{k}\boldsymbol{a}_1} + e^{i\boldsymbol{k}\boldsymbol{a}_2})$. From (3.19) and solving

$$\begin{aligned} \boldsymbol{K}\boldsymbol{a}_1 &= \frac{4\pi}{3} \qquad & \boldsymbol{K'}\boldsymbol{a}_1 &= \frac{2\pi}{3} \\ \boldsymbol{K}\boldsymbol{a}_2 &= \frac{2\pi}{3} \qquad & \boldsymbol{K'}\boldsymbol{a}_1 &= \frac{4\pi}{3} \end{aligned} \tag{3.20}$$

one finds the only two solutions $\boldsymbol{K} = \frac{2\pi}{3a}(1, \frac{1}{\sqrt{3}})$ and $\boldsymbol{K'} = \frac{2\pi}{3a}(1, -\frac{1}{\sqrt{3}})$.

The absence of C_3 symmetry implies anisotropy of the hopping terms ($t_1 \neq t_2 \neq t_3$). It follows that the Dirac cones can move within the first Brillouin Zone changing position. Nevertheless the Chern number, meaning the sum of all vorticities in the first BZ, must be unchanged as long as the Dirac cones remain gap-less [20].

3.2.2 EDGE MODES

One of the goal in the study of the topological properties of graphene, is to understand under which conditions chiral edge states appear. These can reveal quantum Hall phase of graphene, meaning its non-trivial topological phase.

The analysis of graphene performed so far goes on two levels: the studying of its honeycomb lattice and the construction of a continuum model at the Dirac cones. Focusing now on the discrete lattice model, one can see that distinct boundary conditions can determine the appearance of different edge states.

Let's introduce a generic tight-binding Hamiltonian in real space with just nearest neighborhood hopping

$$H = -t \sum_{<i,j>} c_i^\dagger c_j + h.c.$$

It is customary to introduce periodic boundary conditions only in one direction, x-axis in this case, and open boundaries in the other (y-axis).

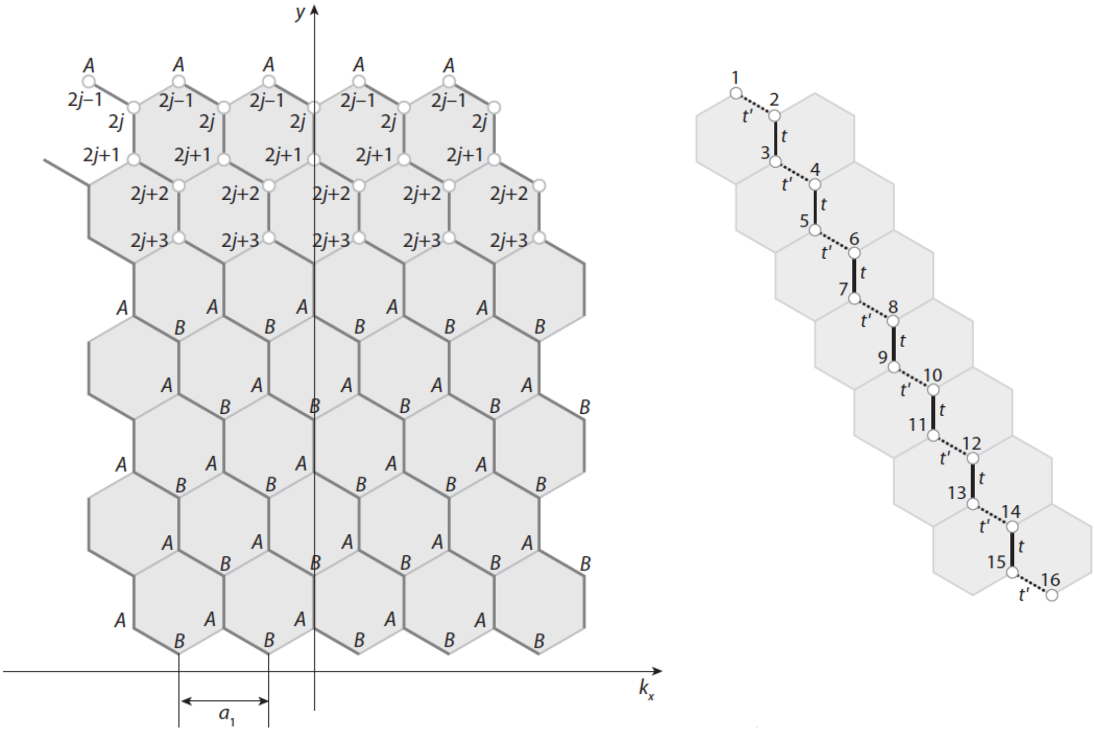

Figure 3.2: *Graphene edge lattice. (Left) shows the honeycomb graphene lattice with open-boundary conditions in the y-direction and periodic conditions in the x-direction. A and B label the sub-lattice sites. k_x along the abscissa, refers to the fact that along x there are periodic boundary condition and can be performed a Fourier transformation that maps x the to momentum space abscissa k_x. (Right) labels the position of the different sites. t and t' refer to different hopping energies [20]*

Referring to figure (3.2), the lattice presents "zigzag" chains oriented at an angle of $\frac{\pi}{6}$ with respect to the horizontal. It is possible then, to perform a Fourier transform on the x direction and work out the following Hamiltonian [20]

$$
\begin{aligned}
H = & -t\sum_j (c^\dagger_{2j,k_x} c_{2j+1,k_x} + c^\dagger_{2j,k_x} c_{2j-1,k_x}(1+e^{-ik_x a_1})) = \\
= & -\sum_j [t(c^\dagger_{2j,k_x} c_{2j+1,k_x}) + t'(c^\dagger_{2j,k_x} c_{2j-1,k_x})]
\end{aligned}
\tag{3.21}
$$

with $a_1 = \frac{a\sqrt{3}}{2}$ and a the spacing lattice constant.

In equation (3.21), for $k_x = \frac{\pi}{a_1}$ and $t' = 0$, one can obtain different energy dispersion relations depending on the even or odd number of sites of the zig-zag chain shown in figure (3.2).

Studying the solutions of the Hamiltonian for different values of k_x and different lattice configurations, the band structures is the one represented in image (3.3).

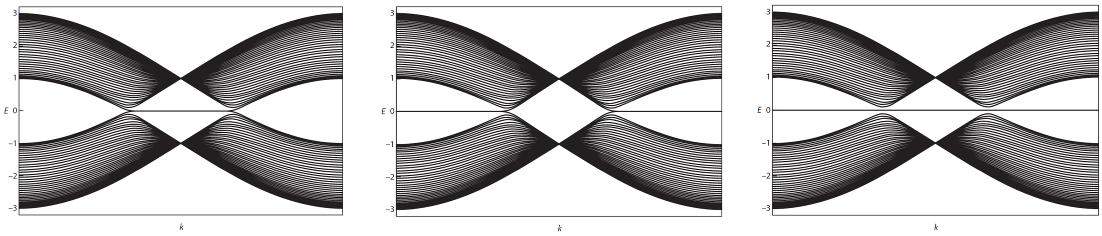

Figure 3.3: *Band structure of graphene tight-binding with edge modes and no mass term in the Hamiltonian (time reversal and inversion symmetry are preserved). (First) the boundaries are sites A and B, the chain has an even number of sites, corresponding to zig-zag edges. (Second) the boundaries are sites B and A, the chain has an even number of sites, corresponding to bearded edges. (Third) the boundaries are sites A and A, the chain has an even number of sites, corresponding to zig-zag and bearded edges at the two opposite borders [20]*

The first two plots show the dispersion relation for a lattice with an even number of sites along the y-direction, while the third corresponds to an odd number. In the first figure there are an A type sub-lattice in the first site and B type in the last position (respectively B-A configuration in the second figure). The band structure shows that, besides the two Dirac cones, there are other 0 energy states. These are the edge modes obtained from an explicit computation of the energy spectrum. In the even lattice configuration there is a double degeneracy for each zero energy value, corresponding to the edge modes at each one of the two borders. These degeneracies cannot be lifted since it would require a perturbation going through the whole sample. For the last figure instead, there is not degeneracy and the $E = 0$ modes go along the entire Brillouin Zone.

When a mass term m, of the kind described above, appears in the Hamiltonian, the edge modes can be modified in different ways, depending on the symmetry that m breaks. If the Semenoff mass is added in the Hamiltonian, one of the band structure in figure (3.4) can show up. The edge modes that terminate on sites A go up in energy, whereas those on sites B go down. No gap-less states appear.

The edge modes in fact, never cross the gap connecting the valence and conduction bands. This implies that these band structures preserve, from a topological point of view, their trivial nature. The extra modes, shaped by the boundaries of the sample, can never count as gap-less edge states. One can check that the Chern number is null, and no Hall conductance can be detected.

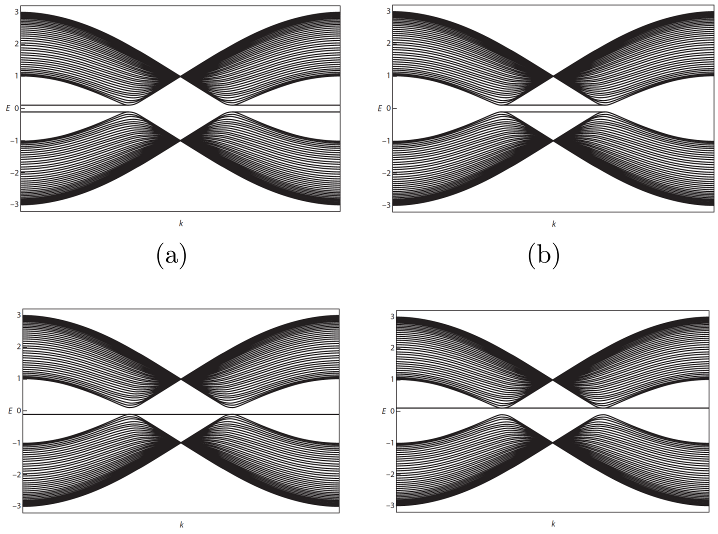

(a) (b)

(c) (d)

Figure 3.4: *Band structure of graphene tight-binding with edge modes and Semenoff mass* $m = 0.3t$ *(t is the hopping energy). (a) The boundaries are sites B and A, the chain has an even number of sites and the boundaries have a bearded shape. (b) The boundaries are sites A and B, the chain has an even number of sites and the boundaries have a zig-zag shape. (c) The boundaries are sites B and B, the chain has an odd number of sites and the boundaries have a zig-zag and bearded shape on the opposite sides. (d) Same configuration of (c) but the edges are A and A sites [20].*

The other mass that can be added to the Hamiltonian, is the kind that spoils time reversal. This is called *Haldane mass* since it was Duncan Haldane who first proposed this model. As mentioned before, a system with such broken symmetry, presents interesting topological properties that are addressed in the next paragraph.

3.2.3 Haldane model

The goal of this model is to construct quantum Hall phases in the absence of a magnetic field and Landau levels, starting from a standard Bloch band structure with time reversal broken symmetry. The lattice is the standard graphene honeycomb one with the two Dirac cones in the first Brillouin zone. To break time reversal, leaving the translation symmetries of the lattice unchanged, one can add a complex second nearest neighborhood hopping term.

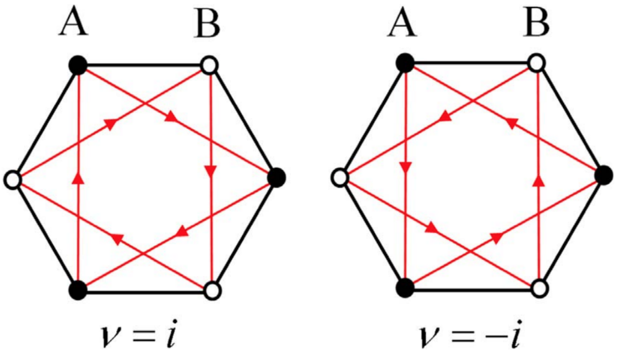

Figure 3.5: *Honeycomb cell of graphene. The arrows show the second nearest-neighborhood hoppings. The clockwise or anti-clockwise rotations give a phase contribution of different sign that, in the Hamiltonian, is represented by the hopping energy* t'_2 *and its complex conjugate* $(t'_2)^2 \neq t'_2$ *[27].*

The presence of n.n. hopping spoils particle-hole symmetry that though, is not a real symmetry of graphene. On the other side, the fact that this term is complex, meaning it carries a uni-modular phase, breaks time reversal. This phase simulates the presence of a periodic local magnetic flux normal to the lattice plane and with zero total flux through each unit cell. It follows that, the periodicity of the lattice and so the translation symmetry, is preserved [4]. To be more clear, this phase factor is defined by $\frac{ie}{\hbar}\int A d\boldsymbol{r}$, with $A(\boldsymbol{r})$ the vector potential of the magnetic field and with the integration performed along the hopping path. The fact that this phase factor does not appear in the first n.n. term, is because in this case the integration goes along all the unit cell, so the net flux is equal to 0. In the case of second n.n. the hopping direction can go clockwise or anti-clockwise giving a phase contribution of different sign. Thus, for clockwise rotations, the hopping is described by t'_2, while for anticlockwise ones by its complex conjugate $(t'_2)^* \neq t'_2$, corresponding to different chiralities of the system (figure (3.5)).

The Hamiltonian can be written

$$H = t_1 \sum_{\langle i,j \rangle} (a_i^\dagger b_j + h.c.) + t_2 \sum_{\ll i,j \gg} (e^{-i\phi} a_i^\dagger a_j + e^{+i\phi} b_i^\dagger b_j + h.c.) + m \sum_i (a_i^\dagger a_i - b_i^\dagger b_i) \quad (3.22)$$

This has the same expression of the Hamiltonian in the first equation of the first chapter, with the addition of the mass term with different sign in the two sub-lattices and the $e^{\pm i\phi}$ term. The sign of the phase refers to the convention in figure (3.6). It shows that, fixed a hopping direction $e^{\pm i\phi}$, it is opposite for A and B.

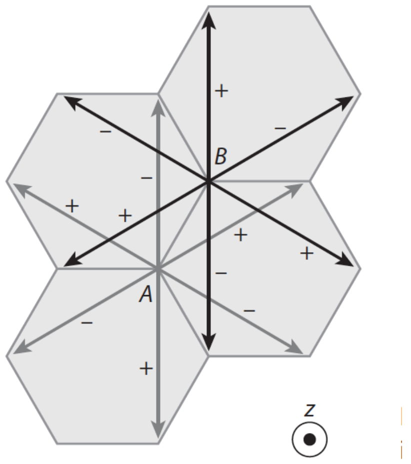

Figure 3.6: *Phase convention for second nearest-neighborhood hopping in the Haldane model, for a Chern insulator [20].*

Without fixing any boundaries, but just appealing to translation symmetry, let's perform a Fourier transform in a similar way to what is done in the first chapter. The resulting Hamiltonian is

$$h(\boldsymbol{k}) = \epsilon(\boldsymbol{k}) + d(\boldsymbol{k})_i\sigma_i$$

where the sum over i is understood and $d(\boldsymbol{k})$ dependents on the wave function. In particular

$$\begin{aligned} d_1(\boldsymbol{k}) =& cos(\boldsymbol{k\alpha}_1) + cos(\boldsymbol{k\alpha}_2) + 1 \\ d_2(\boldsymbol{k}) =& sin(\boldsymbol{k\alpha}_1) + sin(\boldsymbol{k\alpha}_2) \\ d_3(\boldsymbol{k}) =& m - 2t_2 sin(\phi)(sin(\boldsymbol{k\alpha}_1) - sin(\boldsymbol{k\alpha}_2) + (sin(\boldsymbol{k\alpha}_3)) \\ \epsilon(\boldsymbol{k}) =& 2t_2 cos(\phi)\sum_{\boldsymbol{a}} cos(\boldsymbol{k\alpha}) \end{aligned} \tag{3.23}$$

where $\sum\limits_{\boldsymbol{a}}$ is the summation over the lattice vectors $\boldsymbol{a}_1$, $\boldsymbol{a}_2$, $\boldsymbol{a}_3 = \boldsymbol{a}_2 - \boldsymbol{a}_1$ defined in chapter 1.

The term $\epsilon(\boldsymbol{k})$ is proportional to the identity, so it just lifts the energy bands and it does not add any interesting property. To keep time reversal from (3.12), one must have that $d_1(\boldsymbol{k}) = d_1(-\boldsymbol{k})$, $d_2(\boldsymbol{k}) = -d_2(-\boldsymbol{k})$, $d_3(\boldsymbol{k}) = d_3(-\boldsymbol{k})$ and $\epsilon(\boldsymbol{k}) = \epsilon(-\boldsymbol{k})$. The condition for $d_3(\boldsymbol{k})$ is fulfilled only when the $sin(\phi) = 0$, namely $\phi = 0, \pi$. Inversion symmetry is instead defined by equation (3.13) and (3.14), giving the following conditions $d_1(\boldsymbol{k}) = d_1(-\boldsymbol{k})$, $d_2(\boldsymbol{k}) = -d_2(-\boldsymbol{k})$, $d_3(\boldsymbol{k}) = -d_3(-\boldsymbol{k})$ and $\epsilon(\boldsymbol{k}) = \epsilon(-\boldsymbol{k})$. Thus, the terms (3.23) satisfy inversion symmetry only for $m = 0$, imposing again a constrain only on $d_3(\boldsymbol{k})$.

The Hamiltonian described by (3.23) is invariant under C_3. It is not affected by the permutation of the nearest neighborhood vectors and it has the same value of t for the three hoppings. It follows that the position of the Dirac cones is fixed and the opening and closing of the gap can happen only at those exact points within the first Brillouin Zone.

To see what happen at $\boldsymbol{K}$ and $\boldsymbol{K}'$, one should first expand $d_3(\boldsymbol{k})$ close to them. For $\boldsymbol{k} \simeq \boldsymbol{K}$, using (3.20) together with $\boldsymbol{K}\boldsymbol{a}_3 = \frac{4\pi}{3}$ and $\boldsymbol{K}'\boldsymbol{a}_3 = \frac{2\pi}{3}$, one finds that the sum in parenthesis in $d_3(\boldsymbol{k})$ gives back $\frac{-3\sqrt{3}}{2}$ for $\boldsymbol{K}$ and $\frac{3\sqrt{3}}{2}$ for $\boldsymbol{K}'$. So

$$\begin{aligned} d_3(\boldsymbol{k} \simeq \boldsymbol{K}) &= m + 3\sqrt{3}\ t_2 sin(\phi) \\ d_3(\boldsymbol{k} \simeq \boldsymbol{K}') &= m - 3\sqrt{3}\ t_2 sin(\phi) \end{aligned} \tag{3.24}$$

Fixing initially the system on a configuration with $m \neq 0$ and $t_2 = 0$, it results gapped. But, increasing/decreasing t_2, the system becomes gap-less for the two values $\pm\frac{\sqrt{3}m}{3t_2 sin(\phi)}$. For the minus sign only $\boldsymbol{K}$ closes, vice versa for the plus.

To study the topological phase transitions close to the Dirac points, one should first study what changes in the results, obtained so far, when the system is studied in the continuum limit, meaning going close to $\boldsymbol{K}$ and $\boldsymbol{K}'$. In this case by definition, there is not a lattice and the momentum is defined over the whole Euclidean space. The Hall conductance is an integer only if the base manifold is compact, which is a property that the Euclidean space does not have. This explains why in the continuum, massive Dirac fermions exhibit half-integer quantum Hall effect

$$\begin{aligned} \sigma_{xy} =& \frac{e^2}{2\pi\hbar}\int dk_x dk_y V(k)_{xy} = \frac{e^2}{2\pi\hbar}\int dk_x dk_y \frac{m'}{2(m'^2 + k^2)^{3/2}} = \\ =& \frac{e^2}{\hbar}\frac{sign(m')}{2} \end{aligned} \tag{3.25}$$

In particular for a generic Dirac Hamiltonian $h(\boldsymbol{k}) = k_i \mathcal{A}_{ij}\sigma_j + m\sigma_3$ (A_{ij} are numbers with $i, j = 1, 2$), equation (3.25) becomes

$$\sigma_{xy} = \frac{e^2}{\hbar}\left(\tfrac{1}{2} sign(m) sign(det(\mathcal{A}))\right) \tag{3.26}$$

The equation shows that the Hall conductance is equal to $\frac{1}{2}$ times the sign of the mass of the fermions. In the continuum, the bandwidth of the spectrum is infinite and there are some fermions, called *spectators* [20], that do not enter in the computation of (3.25), thereby to this fractional factor. On a periodic lattice, the bandwidth is forced within a range of values. It follows that, the points where the bands bend down, give the contribution of another half to the Hall conductance that comes back to its integer value. So the study of the problem in the continuum corresponds to confine the computations to a small part of the filled bands. Nevertheless, even though one cannot have a complete picture of the problem, it is still possible to collect information about the topological phase transition and the change in the Hall conductance just focusing close to the transition points.

There is a way to overcome this incompleteness in the results and compute the quantized integer value of the Hall conductance even in the continuum. Looking at (3.25), it is clear that if the opening and closing of the gap is accompanied by the change in the sign of the mass, the Hall conductance changes by 1

$$\Delta\sigma_{xy} = \frac{e^2}{\hbar}\left(\frac{sign(m' > 0)}{2} - \frac{sign(m' < 0)}{2}\right) = \frac{e^2}{\hbar} \tag{3.27}$$

Knowing the value of σ_{xy} before the transition, one can find the Hall conductance after the gap closing and reopening, summing to σ_{xy} the value of (3.27) [20].

Coming back to Haldane model, to construct the topological phase diagram of graphene, one should start from the lattice with a well known configuration, for which it is possible to compute the integer value of the Hall conductance. Let's consider the Hamiltonian in the discrete representation of equation (3.22) and (3.23). For $m \to \pm\infty$ the hopping terms can be neglected and the system describes a trivial topological situation with the wave functions localized at the A and B sites. One can conclude that $\sigma_{xy} = 0$, and so the Chern number, is null. Setting $t_2 > 0$ and $0 < \phi < \pi$, one can increase the value of $m \to -\infty$ up to $m = -3\sqrt{3}\ t_2 sin(\phi)$, which is the point where $\boldsymbol{K}$ goes through closing and opening of the gap. To compute σ_{xy}, one should refer to equation (3.26), this is again the continuum limit since the problem is studied close to the Dirac point. In gap closing and reopening, the Hall conductance goes from $\frac{e^2}{\hbar}\left(\frac{1}{2}sign(m + 3\sqrt{3}t_2 sin(\phi)\right) = -\frac{1}{2}$ to $\frac{e^2}{\hbar}\left(\frac{1}{2}sign(m + 3\sqrt{3}t_2 sin(\phi)\right) = \frac{1}{2}$, so

$$\Delta\sigma_{xy} = \frac{e^2}{\hbar}$$

Adding this result to the previous value of the conductance, one finds $\sigma_{xy} = \frac{e^2}{\hbar}$ and the Chern number $C = +1$. The topological phase is non-trivial.

The value of m can now be increased to $3\sqrt{3}\ t_2 sin(\phi)$ where $\boldsymbol{K}$ remains gapless, while $\boldsymbol{K'}$ closes. The Hall conductance at $\boldsymbol{K'}$, goes from $\frac{e^2}{\hbar}\left(\frac{1}{2}sign(m - 3\sqrt{3}t_2 sin(\phi)\right) = \frac{1}{2}$ to $\frac{e^2}{\hbar}\left(\frac{1}{2}sign(m - 3\sqrt{3}t_2 sin(\phi)\right) = -\frac{1}{2}$, so

$$\Delta\sigma_{xy} = -\frac{e^2}{\hbar}$$

Adding this result to the previous value of the conductance $\sigma_{xy} = \frac{e^2}{\hbar} - \frac{e^2}{\hbar} = 0$. Thus, the system comes back to a trivial phase with $C = 0$. (3.7).

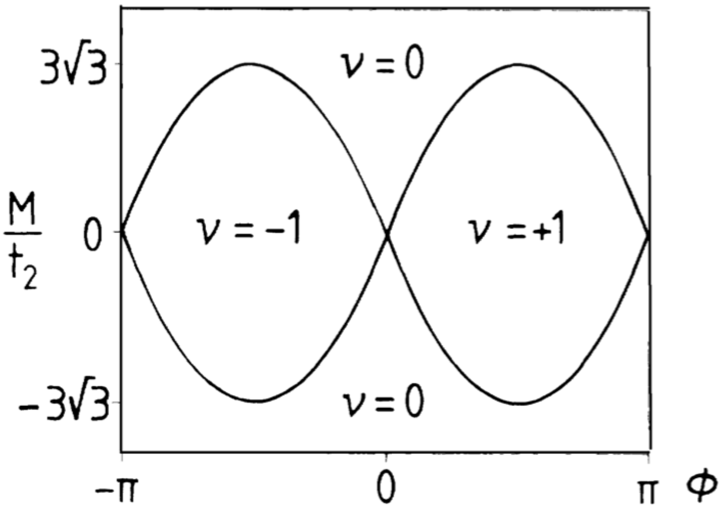

Figure 3.7: *Phase diagram of the Haldane model for graphene. In the $x-axis$ there is ϕ, the phase associated to the t'_2 hopping energy to the second nearest-neighborhood, in the the $y-axis$ there is the mass ($m = M$) over t_2. ν represents the Chern number C, labelling the three different topological phases with $C = 0, \pm 1$ respectively [4].*

To complete the phase diagram of the Haldane model, the same calculations must be performed for $\phi < 0$. One obtains the opposite result, giving rise to the diagram in figure.

At this point it is clear that, from bulk-edge correspondence one should expect the appearance of edge states, whose features should depend in part from the boundaries of the sample. Before it was shown that the introduction of a Semenoff mass, in the tight bonding Hamiltonian of a zigzag boundaries lattice, leads to the appearance of edge states that remain attached to the valence or the conduction bands after the gap opens ((3.4)). With the same set up for the graphene Hamiltonian, if one now introduces the Haldane mass, the new edge states that arise connect two distinct Dirac cones located at opposite bands (the conduction and the valence one (3.8)). Thus, these modes become a conduit that consent to transfer states between the two bands. Because of the chirality, only one direction of travel is allowed, depending on the sign of the Hall conductance, meaning the sign of the fictitious magnetic flux through the bulk. The appearance of these states travelling from the valence to the conductance band and vice-versa and a non zero Hall conductance, become together with a Chern number $C = \pm 1$, the main ingredients that describe topological phases in graphene.

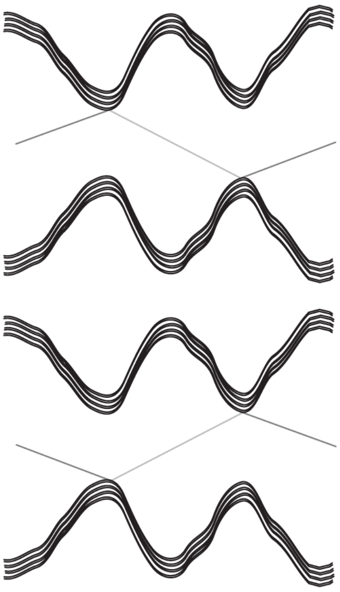

Figure 3.8: *Sketch of graphene gap-less edge states with Haldane mass. (Up) The boundaries are sites A and A, the chain has an odd number of sites. (Down) The boundaries are sites B and B, the chain has an even number of sites. The two different figures show opposite chirality, in one case the charge carriers can flow only from the conduction to the valence band, vice versa in the other [20].*

4

TOPOLOGY OF THE CONTINUUM MODEL

The topological properties of monolayer graphene and related 2-D models, such as the Haldane one, show the intriguing features of this material. On the other side, the introduction of the continuum model for small angle twisted bilayer, exhibits the analogy between the two structures close to the Dirac cones. This inevitably pushed people in the attempt to apply the topological results for single layer graphene, to the bilayer case. Particular interest falls to the two flat bands at the lowest energy that appear at the magic angle. In the simplest case, thus without the effect of any relaxation, nor on-site asymmetry between the two layers, these are gap-less states. The possibility for phase transitions to occur, requires the opening of a gap in correspondence to the two Dirac cones of the "super-lattice" Brillouin Zone and the breaking of the symmetries that protect those points.

The goal, here, is to combine the results from second and third chapter, in the attempt to construct a topological phase diagram of twisted bilayer graphene. The continuum model is initially perturbed with a small mass and the Berry curvature, for the Dirac cones of a single valley, is computed. It follows the study of the phase transitions in dependence to the different features of the perturbation. This analysis leads to interesting results. Nevertheless it cannot be complete, but requires the final landing to a tight-binding model that includes more then just the two low-energy flat bands.

4.1 Symmetries of the continuum model

The continuum model is independent of the commensurability or inconmmensurability of the rotation angle between the two graphene sheets for small θ. The electronic properties of the two flat bands, in fact, do not depend on the exact geometrical setting of the problem [28].

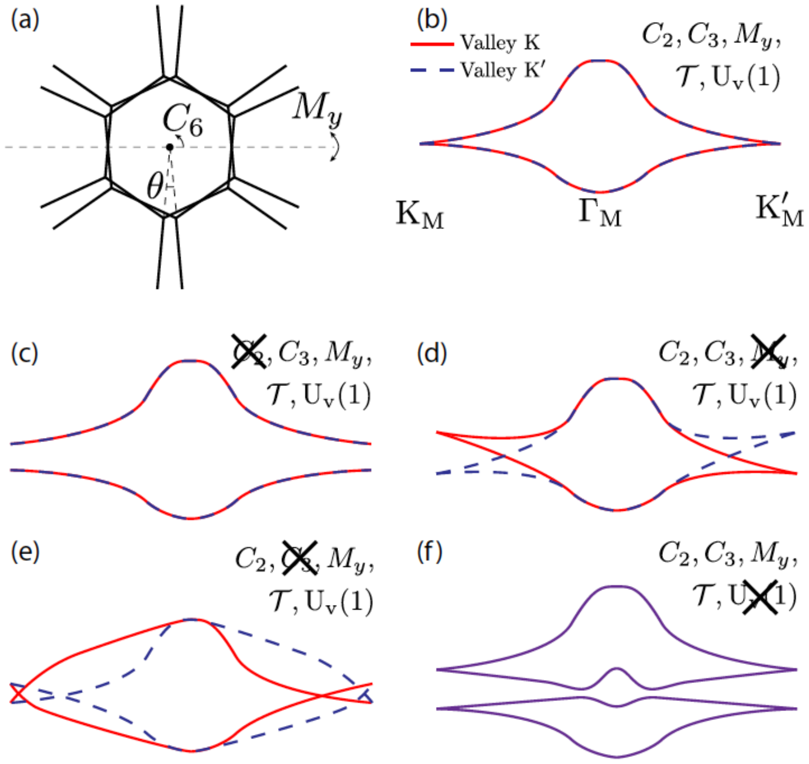

Figure 4.1: *The effect of symmetry breaking in the continuum model of TBG is shown. (a) The plot represents the FBZs of the two graphene layers rotated about the common centre of the hexagon. (b) The low energy mini-bands of the two inequivalent valleys are sketched, with respectively dashed black lines and red continuous ones. The labelled sites refer to the high symmetry points of the FBZ. (c) C_2, in-plane rotation of* 180°*, is broken with the opening of a gap at the Dirac cones. (d) The effect of an external perpendicular electric field is shown. Mirror symmetry M_y, namely C_{2y}, is broken and the two Dirac cones, in the same valley, are not degenerate in their energy eigenvalues anymore. (e)C_3, in-plane rotation of* 120°*, is broken. The cones are still protected because of $C_2\mathcal{T}$, but they are free to move around in the FBZ. (f) Valley charge conservation $U_v(1)$ is broken. The two valleys can interact between each other and the degeneracy is lifted.* [19]

The formation of a reciprocal lattice pattern and the presence of the Dirac cones, anticipate that the symmetries of the continuum theory must be almost the same as the monolayer ones. The effective model for a single valley, $H_{\boldsymbol{k}} = H_D^b + H_D^t + T_{\boldsymbol{k}}$ (t and b stand for top and bottom layer), implies moiré translation symmetry and C_3 rotation that, as in the monolayer case, inhibits Dirac cones from moving around within the Brillouin Zone. Particularly interesting it is $C_2\mathcal{T}$, that prevents the Dirac points from opening a gap. This symmetry can be expressed with the operator form

$$C_2\mathcal{T} = \sigma_x \mathcal{K}_c$$

which is the analogous of applying inversion symmetry and time reversal in monolayer. This operator leaves invariant the effective Hamiltonian, $h(\boldsymbol{k}) = (k_x\sigma_x - k_y\sigma_y)$, of the two low-energy mini-bands. In fact

$$(C_2\mathcal{T})h(\boldsymbol{k})(C_2\mathcal{T})^{-1} = \sigma_x(k_x^*\sigma_x + k_y^*\sigma_y)\sigma_x = (k_x\sigma_x - k_y\sigma_y) = h(\boldsymbol{k})$$

mapping one Dirac cone into the other analogous one of the Moiré Brillouin Zone. Another interesting symmetry is C_{2y}. It consist in a two-fold rotation of the twisted bilayer in the 3-D space, meaning it flips the two layers. This is why, it is also accounted as mirror symmetry M_y, [28]. It can be broken by an electric magnetic field applied perpendicular to the lattice. Doing so, in fact, the two almost flat bands are modified at the Dirac cones, as shown in the figure (4.1). After all, the role of this symmetry is to ensure that the two Dirac cones of the super-lattice are at the same energy.

Lastly there is valley charge conservation that corresponds to the independent conservation of the charge in the two valleys. In the continuum model in fact, the interaction between inequivalent Dirac points is neglected. In figure (4.1) it is shown how the low energy bands in the continuum model are modifies by the different symmetries breaking [19]. The two set of mini-bands, that identify the two valleys, are superimposed and sketched respectively with black dashed lines and solid red ones.

4.2 Berry phase of the super-lattice BZ

Following the steps of [29] and the first chapter, one can try to introduce small variations in the continuum model twisted bilayer Hamiltonian and see how the band structure for low energy changes. The discussion from now on, will involve the two almost flat bands that become gradually thinner closer to the magic angle [1]. To get an idea, for an angle of $\theta = 1.08°$ the bandwidth is $U = 12meV$ for the $E > 0$ branch and $U = 2meV$ for the $E < 0$ one, showing a good spacing from the upper bands (almost $20meV$), as one can see from the plot (4.2).

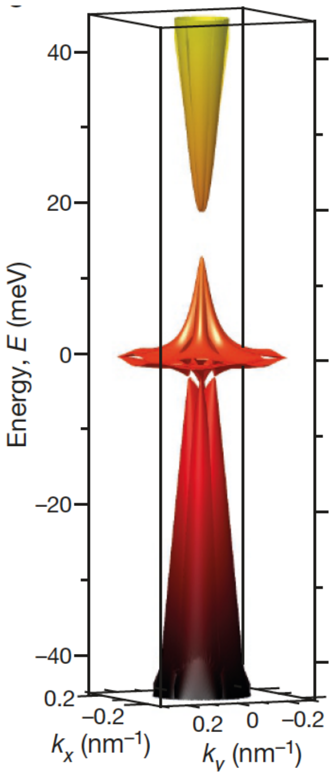

Figure 4.2: *The image plots the energy bands of TBG at $\theta = 1.05°$ for the first mini Brillouin zone of the super-lattice. The figure, by Jarillo-Herrero and colleagues, is made using the continuum model Hamiltonian.* [2]

The energy dispersion relation of the continuum model at the Dirac cones, is equal to the monolayer one. For two layers rotated by a $\theta/2$ angle in opposite directions, the Hamiltonian in momentum space, truncated at the first honeycomb cell of the super-lattice, is described by (2.18). The easiest attempt to open a gap within the two flat bands is the introduction of a mass term, such as an on-site potential different for the two layers, respectively m_1 and m_2. Working in the hypothesis that $m_1, m_2 \ll v_f k_\theta$, with k_θ the modulus of the hopping momentum between $\boldsymbol{K}_1$ and $\boldsymbol{K}_2$, one can consider the two masses just as small corrections to the Hamiltonian. These implies that the first order perturbation matrix, introduced in the second chapter, can now be replaced with

$$H^{(1)}_{\boldsymbol{k}} = \begin{pmatrix} h_{1,\boldsymbol{k}} & 0 \\ 0 & h_{2,\boldsymbol{k}} \end{pmatrix}$$

where $h_{1,\boldsymbol{k}} = v_f \boldsymbol{\sigma}^* \boldsymbol{k} + m_1 \sigma_z$ for the first layer and $h_{2,\boldsymbol{k}} = v_f \boldsymbol{\sigma}^* \boldsymbol{k} + m_2 \sigma_z$ for the second. For now, it is convenient to set $m_1 = m_2 = m$ and only later study the behaviour for $m_1 \neq m_2$.
Once again, one can check that

$$H_0 = \begin{pmatrix} h_0(\theta/2) & T_b & T_{tr} & T_{tl} \\ T_b^\dagger & h_{\boldsymbol{q}_b}(-\theta/2) & 0 & 0 \\ T_{tr}^\dagger & 0 & h_{\boldsymbol{q}_{tr}}(-\theta/2) & 0 \\ T_{tr}^\dagger & 0 & 0 & h_{\boldsymbol{q}_{tl}}(-\theta/2) \end{pmatrix}$$

has zero energy eigenstates. Neglecting the rotation angle θ in the expression for h_j, one can make use of the almost-exact perturbation theory and find

$$\frac{< \Psi^{(i)} | H^{(1)}_{\boldsymbol{k}} | \Psi^{(i)} >}{< \Psi^{(i)} | \Psi^{(j)} >} = \frac{1}{< \Psi^{(i)} | \Psi^{(j)} >} \left[\Psi_0^{(i)\dagger} h_{1,\boldsymbol{k}} \Psi_0^{(j)} + \Psi_0^{(i)\dagger} (T_j h_j^{-1\dagger} h_{2,\boldsymbol{k}} h_j^{-1} T_j^\dagger) \Psi_0^{(j)} \right] =$$
$$= \frac{1}{< \Psi^{(i)} | \Psi^{(j)} >} \left[\Psi_0^{(i)\dagger} \big(\boldsymbol{\sigma}^* \boldsymbol{k} + m\sigma_z \big) \Psi_0^{(j)} - \Psi_0^{(i)\dagger} \big(\sum_j T_j h_j^{-1\dagger} \big(\boldsymbol{\sigma}^* \boldsymbol{k} + m\sigma_z \big) h_j^{-1} T_j^\dagger \big) \Psi_0^{(j)} \right]$$

The last expression in the second equality gives

$$\sum_j T_j h_j^{-1\dagger} m \sigma_z h_j^{-1} T_j^\dagger = 3m(1 - \beta^2)\sigma_z \tag{4.1}$$

with $\beta = \frac{w_{AA}}{w_{AB}}$. The renormalization instead

$$|\Psi|^2 = 1 + |\psi_j|^2 = 1 + \psi_0^\dagger T_j h_j^{-1\dagger} h_j^{-1} T_j^\dagger \psi_0 = 1 + 3(1 + \beta^2)\alpha^2 \tag{4.2}$$

Assuming the hopping is homogeneous for all sub-lattices, $\beta = 1$. Therefore the result is

$$\frac{< \Psi^{(i)}|H^{(1)}_{\boldsymbol{k}}|\Psi^{(i)} >}{< \Psi^{(i)}|\Psi^{(j)} >} = \frac{1}{6\alpha^2+1}\Psi_0^{(i)\dagger}\big(v(1-3\alpha^2)\boldsymbol{\sigma}^*\boldsymbol{k}+m\sigma_z\big)\Psi_0^{(j)} \tag{4.3}$$

In addition to the renormalized velocity one finds a renormalized mass

$$\begin{aligned} v^* &= v\frac{1-3\alpha^2}{1+6\alpha^2} \\ m^* &= \frac{m}{1+6\alpha^2} \end{aligned}$$

Thus the Hamiltonian for the two lowest bands close to $\bar{\boldsymbol{K}}$ is simply

$$H_{\bar{\boldsymbol{K}}} = v^*(\boldsymbol{\sigma}^*\boldsymbol{k}) + m^*\sigma_z \tag{4.4}$$

The bar notation stands for the Dirac cones in the super-lattice Brillouin Zone.

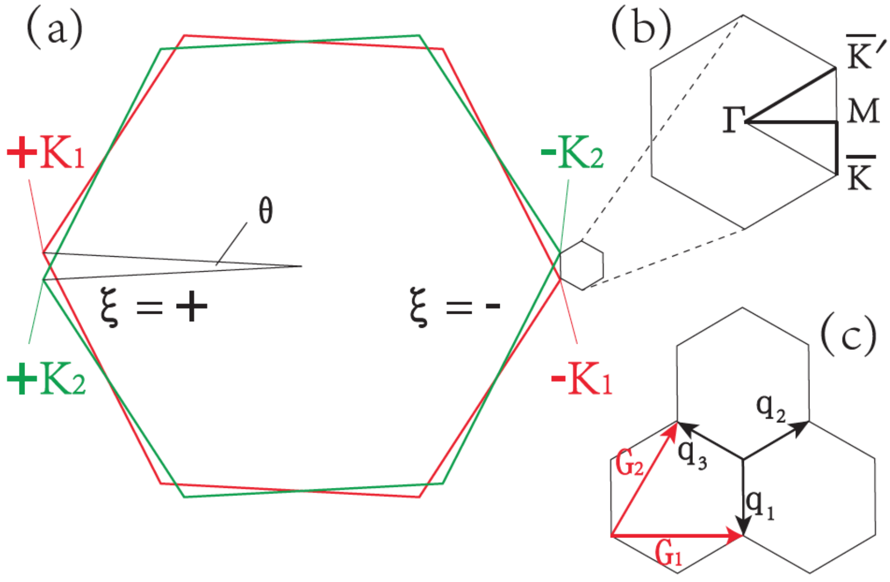

Figure 4.3: *Honeycomb cell for TBG. (a) The figure shows the FBZ of the two rotated layers of graphene. ξ refers to the two inequivalent valleys. (b) The Dirac cones are folded to the mini Brillouin Zone of the super-lattice. The labelled sites are the high symmetry points. $\boldsymbol{K}_{1/2}$ are the valleys of the monolayer lattice, $\bar{\boldsymbol{K}}$ and $\bar{\boldsymbol{K}}'$ the Dirac cones in bilayer graphene. (c) $\boldsymbol{q}_i$ are the momentum transfers that correspond to the three interlayer hopping processes. $\boldsymbol{G}_{1/2}$ are the reciprocal basis vectors.* [29]

Equation (4.4) is equal to (3.15), that describes a Dirac spin-less Hamiltonian with a Semenoff mass that breaks sub-lattice symmetry, assigning opposite on-site energy to A and B. It follows that the band structure of (4.4) is gapped at the Dirac cones. In analogy to the monolayer case one might conclude that (4.4) describes a trivial phase. This is not the case.

To understand the topological properties of this Hamiltonian it is useful to pay attention to figure (4.3). The two layer honeycomb cells are shown with a relative rotation angle of $\theta/2$ (caption (a)), forming a new Brillouin zone with different features from the monolayer case. The adjacent cones in figure (4.3) (b), in fact, describe two equivalent Dirac points $\boldsymbol{K}_1$ and $\boldsymbol{K}_2$. In the previous chapter, in monolayer graphene in correspondence to $\boldsymbol{K}$ and $\boldsymbol{K}'$ (respectively $\boldsymbol{K}_1$ and $-\boldsymbol{K}_1$ in the figure), it was found that the Berry phase has values $\pm\pi$. In this case instead, dealing with two equivalent cones, one should aspect the same contribution to the Berry phase coming from $\bar{\boldsymbol{K}}$ and $\bar{\boldsymbol{K}}'$, leading to a total non-zero Chern number.

Let's examine at first the monolayer case. Equation (4.4) describes a 2-D Dirac Hamiltonian in the continuum. It is possible then, to compute the Chern number of the valence band for each of the two Dirac cones. Following reference [20], one first finds the eigenvalues of the valence band. Diagonalizing the Hamiltonian (4.4), $E = \pm\sqrt{|\boldsymbol{k}|^2 + m^2}$ and

$$\Psi_{\boldsymbol{K}} = \frac{1}{\sqrt{2E}(\sqrt{E} - m)} \begin{pmatrix} m - E \\ k_x - ik_y \end{pmatrix} \tag{4.5}$$

From equation (3.4), the components of the Berry potential are

$$\begin{aligned} A_x &= -\frac{k_y}{2E(E-m)} \\ A_y &= \frac{k_x}{2E(E-m)} \end{aligned}$$

Follows the Berry curvature

$$V_{xy} = \partial_x A_y - \partial_y A_x = -\frac{m}{2(m^2 + |\boldsymbol{k}|^2)^{3/2}} \tag{4.6}$$

Close to the other inequivalent valley, $\boldsymbol{K}'$, the Hamiltonian is $H_{\boldsymbol{K}'} = v(\boldsymbol{\sigma}\boldsymbol{k}) + m\sigma_z$, with eigenvector for the valence band

$$\Psi_{\boldsymbol{K}'} = \frac{1}{\sqrt{2E}(\sqrt{E} - m)} \begin{pmatrix} m - E \\ k_x + ik_y \end{pmatrix}$$

The result is a Berry curvature with opposite sign with respect to (4.6)

$$V'_{xy} = \frac{m}{2(m^2 + |\boldsymbol{k}|^2)^{3/2}} \tag{4.7}$$

The Berry phase at the Dicac cones gives opposite contributions ±π that sum up to zero.

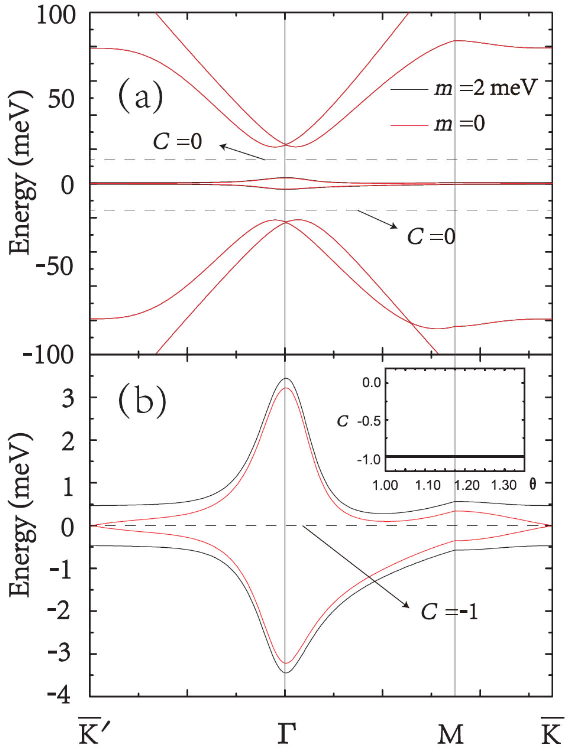

Figure 4.4: *Electronic band structure of twisted bilayer graphene. (a) the figure shows the flat bands together with the ones above and below, for the magic angle* $\theta = 1.05°$*. C labels the Chern number of the filled bands. If the Fermi energy lies above or below the mini-bands,* $C = 0$*. (b) is a zoom in to the flat bands. The red lines refer to a mass-less Hamiltonian, the black ones to a* $m = 2meV$*. In the latter case the Chern number of the filled valence band* $C = -1$*, providing a topological phase. (Inset) shows that the value of C is stable for a range of θ close to the magic angle* [29].

In the bilayer case instead, the two valleys are described by the same Hamiltonian (4.4), thus they have the same chirality. This implies that now, the two curvatures sum up to a value different from zero, giving back a Chern number for the valence band $C_v = -1$.

Figure (4.4) [29], is constructed in analogy to (2.2) throughout numerical computation of the continuum model Hamiltonian, where higher order terms are taken into account. It shows the lower energy bands with a zoom in on the flat ones in the image below. The red lines refer to an Hamiltonian with a mass term $m = 0meV$, the black ones to an Hamiltonian with $m = 2meV$ that gaps the Dirac cones. C is the Chern number whose value depends on the position of the chemical potential. If the Fermi energy lies above or below the almost flat bands $C = 0$. Recalling equation (3.10), in fact, the Chern number can be computed as a summation over the filled bands, so the conduction one with $C_c = 1$ sums up to a zero Chern number with $C_v = -1$. Lastly, the inset in the figure shows the value of the Chern number for different values of twisting, $0.99° \leq 1.35°$. At early stage one can conclude that the topology is well controlled by the curvature close to $\bar{\boldsymbol{K}}$ and $\bar{\boldsymbol{K}}'$ and that, even moving away from the first magic angle, there is not sign of topological phase transitions.

4.3 PHASE DIAGRAM OF THE FLAT BANDS

In the following the analysis and results proposed in reference [29] are presented. It is shown the phase diagram constructed from numerical calculation of the continuum model Hamiltonian when corrugation and different values of the two masses m_1 and m_2 are accounted.

In the second chapter it has been introduced $w = \frac{t_{k_D}}{\Omega} = 110meV$, the effective interaction parameter between layers, that has been handled as a constant. Ω is the unit cell area, while $t_{\boldsymbol{q}}$ is the hopping amplitude that depends on the wave function $\boldsymbol{q}$ and decays steadily in terms of the excitation momentum. k_D is the magnitude of the momentum at the corner of the Brillouin zone of a single layer, thus the biggest value $t_{\boldsymbol{q}}$ can reach, is given by $|\boldsymbol{q}| \simeq k_D$ and corresponds to the three equivalent Dirac cones that are connected by reciprocal lattice vectors (equation (2.15)).

Nevertheless, moving to real space one should take into account the possible

effect of corrugation in the out of plane direction. From theoretical research and experimental evidence, the regions with AA stacking have a bigger interlayer spacing then AB and BA ones. This implies that the value of w cannot be considered site-independent, but it must rely on the stacking region. In particular, one can fix a couple of more refined values $w_{AA} = 80meV$ and $w_{AB} = 100meV$ [29].
Equations (2.17) become

$$T_1 = \begin{pmatrix} w_{AA} & w_{AB} \\ w_{AB} & w_{AA} \end{pmatrix} = w_{AB} \begin{pmatrix} \beta & 1 \\ 1 & \beta \end{pmatrix}$$

$$T_2 = w_{AB} e^{-i\mathcal{G}^{(2)}\boldsymbol{d}} \begin{pmatrix} \beta e^{-i\phi} & 1 \\ e^{i\phi} & \beta e^{-i\phi} \end{pmatrix} \qquad T_3 = w_{AB} e^{-i\mathcal{G}^{(3)}\boldsymbol{d}} \begin{pmatrix} \beta e^{i\phi} & 1 \\ e^{-i\phi} & \beta e^{i\phi} \end{pmatrix}$$

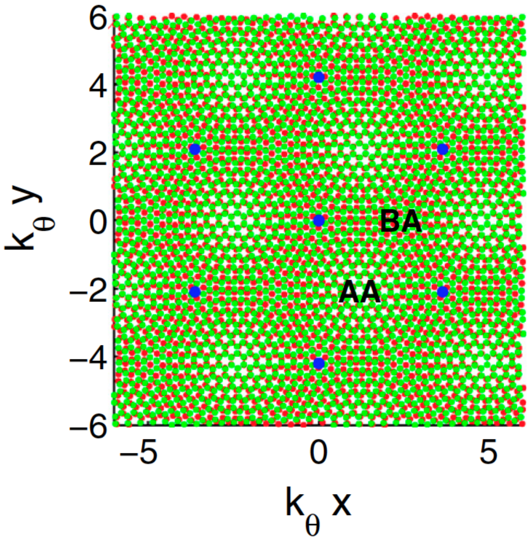

Figure 4.5: *The figure shows the Moiré lattice of twisted bilayer for small rotation angles. The distances are measured in unit of k_θ^{-1}, with $k_\theta = 2k_D \sin(\theta/2)$. One can still see the formation of an hexagonal pattern with AA in the centre and AB/BA sites at the vertices. Regions with AA stacking show more distance between the two layers.* [5]

In figure (4.5) it is plotted the Moiré lattice of twisted bilayer for small rotation angles. The local monolayer pattern is reproduced on a macroscopic scale. One can still see the formation of an hexagonal pattern with AA in the centre and AB/BA sites at the vertices. In AB stacking regions, there is a small gap within the two layers produced by the higher energy value of the tunneling matrix, vice versa in

AA the gap is maximum.

This clarification is important for the construction of the phase diagram. In particular from (4.1), it comes clear that w_{AA} and w_{AB} take action in the form of the effective mass and a phase transition might be tuned by the effect of corrugation.

In this regard, the role of the sign of m_1 for the Berry curvature, and thus for the Chern number, is evident. For a negative mass term the valence band eigenvector of the Hamiltonian (4.4) is

$$\Psi_{\boldsymbol{K}} = \frac{1}{\sqrt{2E}(\sqrt{E}+m)} \begin{pmatrix} -m-E \\ k_x - ik_y \end{pmatrix} \tag{4.8}$$

The components of the Berry potential are

$$\begin{aligned} A_x =& -\frac{k_y}{2E(E+m)} \\ A_y =& \frac{k_x}{2E(E+m)} \end{aligned}$$

it follows the value for the Berry curvature

$$V_{xy} = \frac{m}{2(m^2+|\boldsymbol{k}|^2)^{3/2}} \tag{4.9}$$

From equation (4.9), taking into account the two cones $\bar{\boldsymbol{K}}$ and $\bar{\boldsymbol{K}}'$, the total Chern number of the valence band is $C = 1$. A change in the sign of the mass term m determines topological non trivial states with opposite chirality.

One can now introduce both the corrugation with $w_{AA} \neq w_{AB}$ and different values for the two mass terms in the two layers, respectively m_1 and m_2. Making use of equation (4.1) and (4.2), (4.3) becomes

$$\begin{aligned} &\frac{<\Psi^{(i)}|H^{(1)}_{\boldsymbol{k}}|\Psi^{(i)}>}{<\Psi^{(i)}|\Psi^{(j)}>} = \\ &= \frac{1}{1+3(1+\beta^2)\alpha^2}\Psi_0^{(i)\dagger}\big(v(1-3\alpha^2)\boldsymbol{\sigma}^*\boldsymbol{k} + \big(m_1 + 3m_2(1-\beta^2)\big)\sigma_z\big)\Psi_0^{(j)} \end{aligned} \tag{4.10}$$

Here $\alpha = \frac{w_{AB}}{vk_\theta}$ depends only on the AB hopping parameter and not on β. This implies the important result that the value of the first magic angle, $\alpha^2 = \frac{1}{3}$, is independent of the corrugation. On the other side, recalling (2.28), the renormalized velocity v^*

does depend on β and it can be modifies by the out of plane corrugation

$$v^* = v\frac{1-3\alpha^2}{1+3(1+\beta^2)\alpha^2} \tag{4.11}$$

Similarly for the effective mass

$$m^* = \frac{m_1+3m_2(1-\beta^2)}{1+3(1+\beta^2)\alpha^2} \tag{4.12}$$

The sign of (4.12) depends only on the numerator and it is identically zero close to $\bar{\boldsymbol{K}}$, when $m_1+3m_2(1-\beta^2)=0$.

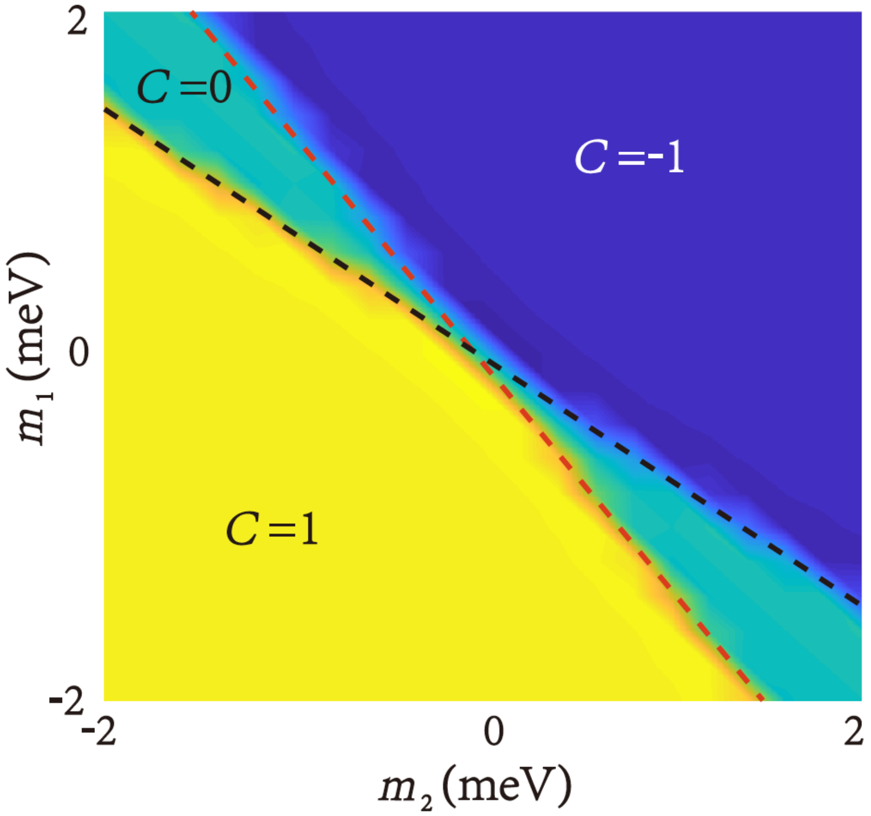

Figure 4.6: *Phase diagram of the continuum model of TBG as a function of the the mass terms* m_1 *and* m_2 *of the two layers. The red line represents equation* $m_1+3(1-\beta^2)m_2=0$, *while the black one* $m_2+3(1-\beta^2)m_1=0$. *These are found imposing the condition for the vanishing of the effective mass* m^*, *respectively at* $\bar{\boldsymbol{K}}$ *and* $\bar{\boldsymbol{K}}$. *The lines represent the boundary of the phase transition, with* C *labelling the Chern number of the valence band, and* β *fixed at* $0,8$. [29]

Similarly at the other Dirac cone $\bar{\boldsymbol{K}}'$, one finds the condition $m_2 + 3m_1(1-\beta^2) = 0$. Fixing $\beta = 0,8$ [29], and plotting the two lines corresponding to $m^* = 0$, red for equation $m_1 + 3m_2(1-\beta^2) = 0$ and black for the other, one can construct the phase diagram in figure (4.6). There is no dependence of the m^* mass term on the twisting angle. Hence one can expect that phase transitions occur even for different angles of rotation, as mentioned before.

For opposite masses in the two layers $m_1 = -m_2$, the Chern number $C = 0$ and the phases are trivial. This is clear from the previous analysis. The two eigenvectors of the valence band for the two Dirac cones $\bar{\boldsymbol{K}}$ and $\bar{\boldsymbol{K}}'$, are described by equation (4.5) and (4.8), giving opposite curvatures that cancel out. Lastly, it can happen that only one layer presents a mass term, giving rise to a Chern valley insulator [29].

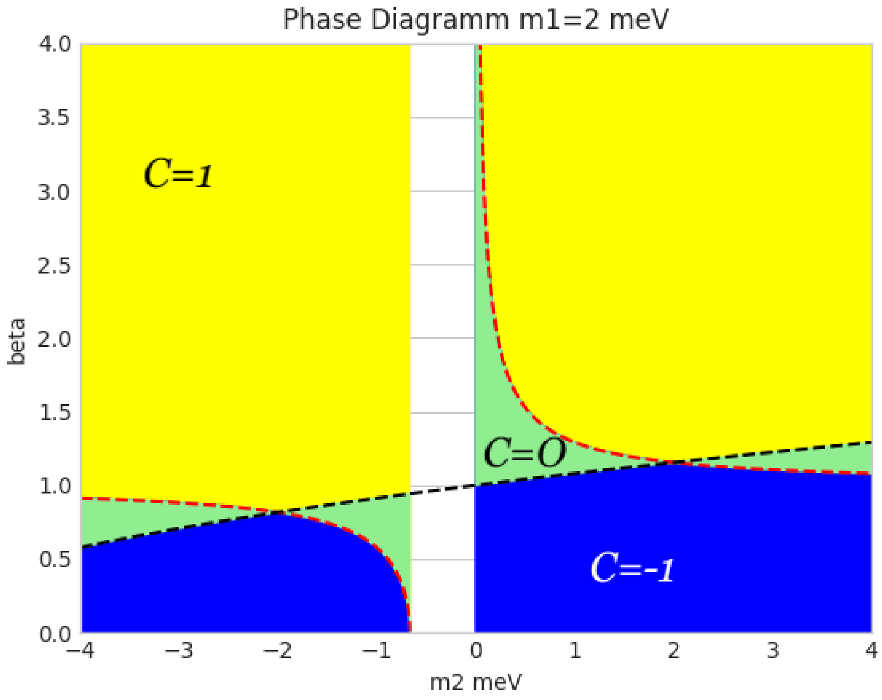

Figure 4.7: *This plot is made along the line of figure (4.6). The phase , this time, is represented as a function of* m_2 *and* β*, while* $m_1 = 2meV$ *is fixed. The two lines that track the boundaries of the phase transitions are still defined by* $m^* = 0$ *at the two Dirac cones,* $\bar{\boldsymbol{K}}$ *and* $\bar{\boldsymbol{K}}'$*. The white spot shows the values where the equations are not defined, because of a negative square root. From this plot it is clear that corrugation has an important role even in the topological properties of TBG. In particular it can induce phase transitions even for fixed values of the masses.*

To see how the corrugation changes the topology of the bilayer, one can fix the masses and change β^2. In figure (4.7), it is plotted the phase diagram as a function of m_2 and β, while $m_1 = 2meV$ is fixed. The two lines, that track the boundaries of the phase transitions, are still defined by $m^* = 0$ at the two Dirac cones, $\bar{\boldsymbol{K}}$ and $\bar{\boldsymbol{K}}'$. From the plot, it is clear that corrugation has an important role in the topological properties of the continuum model. In particular it can induce face transitions even for fixed values of the masses.

To conclude, there are two values of β that should be quoted, since they account for interesting results. When $\beta = \sqrt{\frac{4}{3}}$ the only possible phase is the trivial one, vice versa when $\beta = \sqrt{\frac{2}{3}}$, the two dashed lines in figure (4.6) merge and there are only two states available $C = \pm 1$. In this case the non-trivial topology of the flat bands cannot be altered by any broken symmetry.

This is absurd in a tight binding model. Giving a strong lattice on-site energy the system is described by isolated atoms with almost zero interaction potential. In this case it is meaningless to talk about topological phases and the state must be trivial in a tight-binding description. This is a first warning of the fact that an exhaustive and faithful explanation of the problem requires more then just two bands for a tight-binding model.

4.4 Flipped Haldane model

The continuum model gives interesting insight regarding the topology of the flat bands and good predictions on the shape of the band structure, even far away from the Dirac cones. Nevertheless, a complete understanding of the problem requires the introduction of a lattice model. The bulk-edge correspondence predicts the appearance of edge states for non-trivial topological phases. It is not obvious how the flat bands at the magic angle con induce superconductive states alternated with insulating ones at the boundaries. It is primary then, the construction of a tight-binding model that incorporates the features of the discrete super-lattice. However, the passage from the continuum to the discrete, in the description of the low energy almost-flat bands, is not trivial.

The easiest way to understand it from a physical point of view, is the description of what has been called *flipped Haldane model* [28]. For a mass term m proportional to σ_z and different for the two sub-lattices A and B, twisted bilayer graphene is in a topological phase. It follows that inducing a phase transition, spoiling time reversal, one can either go to a more complex phase or vice versa come to a trivial one.

Recalling the study of Haldane model in the previous chapter, the first step is to identify a well known configuration. In the monolayer case it was recognised with equation (3.23), when the mass $m \to -\infty$. In that case, in fact, the Chern number is $C = 0$. For TBG instead, the Hamiltonian (4.4), even with a strong onsite potential, has $C = -1$. This is a consequence of the same chirality of $\bar{\boldsymbol{K}}$ and $\bar{\boldsymbol{K}}'$ and a curvature equal to (4.6). The different Chern number of the initial configurations for the monolayer and bilayer structure, determines an opposite behaviour when an Haldane-like term is introduced in the Hamiltonian. In the former case, in fact, the closing and reopening of $\boldsymbol{K}$ caused a variation in the Hall conductance that brought the sample into a topological phase with $C = 1$. Vice versa, assuming the analogous set up in the bilayer with the Dirac cones at the same positions and the analogous form for the $d_3(\boldsymbol{k})$ term, one can imagine that a closing and reopening at $\bar{\boldsymbol{K}}$ induces a $\Delta\sigma_{xy} = \frac{e^2}{\hbar}$ that brings the total Chern number to $C = 0$. In this sense, one can think of TBG as a flipped Haldane model where the onsite potential produces a non-zero Chern number and the trivial insulator is obtained by the second neighborhood Haldane hopping.

The contradiction in the construction of the two bands tight-binding model is more clear now. For strong on-site potential, TBG is described by an atomic insulator with a non-zero Chern number. This conclusion clearly does not make sense. A possible solution is the introduction of extra bands, in such a way that the potential is no longer a purely onsite term and the non trivial topology can be explained [28].

5

RELEVANT SYMMETRIES AND WANNIER OBSTRUCTIONS

The continuum model furnishes a good description of TBG for small angles of rotation. It allows to construct, with excellent approximation, the band structure of graphene showing the appearance of Dirac points and the flattening of the valence and conduction bands close to the magic angle. More important, this model implements all the approximate symmetries listed in the previous chapter, that are essential in protecting Dirac crossing points. For a general lattice with incommensurate twist angle, one cannot even assume translational invariance, while for a general commensurate one $U_v(1)$, associated to separate conservation of electrons in the two valleys, is absent. Nevertheless, these symmetries are fundamental in the description of Dirac cones stability and excluding them implies the failure of the model. On the other side, the continuum description does not offer a totally satisfying treatment of the problem. This, in fact, implies the natural landing to a more complex tight-binding model and the construction of Wannier functions, namely wavefunctions in real space that are well-localised in lattice regions where the electrons can hop. The approximate symmetries, so important for protecting the cones, constitute an obstacle to this attempt. In particular, the construction of well localised Wannier functions is prevented by the presence of symmetries that are not exact microscopic ones.

In the literature, one can find many attempts to construct a satisfying tight-binding model for small angle TBG, nevertheless the problem is still open. This knot is connected to a bigger issue, which is the obstruction in the creation of Wannier representations for bands with *fragile topology* [30].

5.1 BAND REPRESENTATION

First of all, let's do a brief introduction on band representation to better understand the salient points of this chapter analysis.

The *space group* G contains all the symmetry operations of a crystalline lattice. The element $g \in G$, that acts in real space, is defined by the action of $g = \{\mathcal{R}|\boldsymbol{v}\}$ as $\boldsymbol{r} \rightarrow \mathcal{R}\boldsymbol{r} + \boldsymbol{v}$ $\{\mathcal{R}|\boldsymbol{v}\}$, with $\mathcal{R}$ a point group operation and $\boldsymbol{v}$ a translation vector. Decomposing $\{\mathcal{R}|\boldsymbol{v}\} = \{\mathcal{R}|\boldsymbol{t}+\boldsymbol{v}'\} = \{\mathcal{E}|\boldsymbol{t}\}\{\mathcal{R}|\boldsymbol{v}'\}$, the first term of the last equality is an operation of Bravais lattice translation group with $\boldsymbol{t}$ proportional to the basis vectors, while $\{\mathcal{R}|\boldsymbol{v}'\}$ is an element of the *point group* with $\boldsymbol{v}'$ a generic translation vector. The *site-symmetry group* on the other side, is the set of operations that leave a position $\boldsymbol{q}$ in the Bravais lattice fixed. It is even called the little group of G and it is such that $G_{\boldsymbol{q}} \equiv \{g \mid g\boldsymbol{q} = \boldsymbol{q}\} \subset G$.

One can now introduce the *Wyckoff position* through the following definition:

"Any two sites whose site-symmetry groups are conjugate are said to lie in the same Wyckoff position. Given a site in the Wyckoff position, the number of sites in its orbit that lie in a single unit cell defines the multiplicity $n_{\boldsymbol{q}}$ of the position" [31].

This means that Wyckoff positions are sites of high symmetry, meaning their position is preserved by a sub-group or the total space group of the lattice. In particular the following holds:

"A site-symmetry group is non-maximal if there exists a finite group $H \neq G_{\boldsymbol{q}}$, such that $G_{\boldsymbol{q}} \subset H \subset G$. A site-symmetry group that is not non-maximal is maximal. A Wyckoff position containing $\boldsymbol{q}$ is maximal if the stabilizer group $G_{\boldsymbol{q}}$ is maximal" [31].

These definitions are important because the symmetry-adapted Wannier functions centred at a Wyckoff position $\boldsymbol{q}$, are basis functions of irreducible representations (irreps) of the little group $G_{\boldsymbol{q}}$.

A Wannier functions can be noted by $W_{i,1}^{(\beta)}(\boldsymbol{r}) = W_i^{(\beta)}(\boldsymbol{r} - \boldsymbol{q})$, where $i = 1, ..n_\beta$ is the degeneracy of the representation $d^{(\beta)}$. The action of an element $g_{\boldsymbol{q}} \in G_{\boldsymbol{q}}$

transforms the Wannier functions as

$$g_{\boldsymbol{q}} W_{i,1}^{(\beta)}(\boldsymbol{r}) = \sum_{i'=1}^{n_\beta} d_{i'i}^{\beta}(\mathcal{R}_{\boldsymbol{q}}) W_{i',1}^{(\beta)}(\boldsymbol{r}) \tag{5.1}$$

where $d_{i'i}^{\beta}(\mathcal{R}_{\boldsymbol{q}})$ is the matrix representation of group representation $d^{(\beta)}$ of the element $g_{\boldsymbol{q}}$. A group G_d of linear operators $\widehat{g}$ in fact, is a representation of G in some vector space L, in such a way that every element $g \in G$ is in correspondence with one and only one element in G_d. The space L, is the space of the representation, and its dimension n is the dimension of the representation. If ψ_i, with $i_1, ..n$, is a basis in L then $\widehat{g}$ is defined by the matrix

$$\widehat{g}\psi_i = \sum_{j=1}^{n} d(g)_{ij}\psi_j$$

One can generate the other Wannier functions at the symmetry equivalent point $\boldsymbol{q}_j$ of $\boldsymbol{q}$, using the transformation g_{j0} of the coset decomposition

$$W_{i,j}^{(\beta)} \equiv g_{j0} W_{i,1}^{(\beta)}(\boldsymbol{r}) = W_i^{(\beta)}(\mathcal{R}_j^{-1}(\boldsymbol{r} - \boldsymbol{q}_j))$$

Let's see now what is the action of a generic space group symmetry operation g on the Wannier functions. For an arbitrary $g = \{\mathcal{R}|v\} \in G$ and the transformation g_{j0} of the coset decomposition $G = \sum_{j,n} g_{jn} G_{\boldsymbol{q}}$ with $g_{jn} = \{\mathcal{R}_j|\boldsymbol{v}_j' + \boldsymbol{t}_n\}$, it exists only one $g_{j'n'}$ and one $g_{\boldsymbol{q}} = \{\mathcal{R}_q|\boldsymbol{v}_{\boldsymbol{q}} + \boldsymbol{t}_{\boldsymbol{q}}\} \in G_{\boldsymbol{q}}$ such that

$$g = g_{j'n'} g_{\boldsymbol{q}} g_{jn}^{-1}$$

and $\mathcal{R} = \mathcal{R}_j' \mathcal{R}_{\boldsymbol{q}} \mathcal{R}_j^{-1}$ (point group operation), and $\boldsymbol{t}_{n'} = \mathcal{T}_{j'j} + \mathcal{R}\boldsymbol{t}_n$ (translation vector). The action of the element g of the space group G on the Wannier functions is

$$g W_{ij}^{\beta}(\boldsymbol{r} - \boldsymbol{t}_n) = \sum_{i'=1}^{n_\beta} d_{(i'i)}^{\beta} W_{i'j'}^{\beta}(\boldsymbol{r} - \mathcal{T}_{j'j} - \mathcal{R}\boldsymbol{t}_n) \tag{5.2}$$

where $W_{ij}^{\beta}(\boldsymbol{r} - \boldsymbol{t}_n)$ is the function in another unit cell obtained applying a translation $\boldsymbol{t}_n$ on the original one. Equation (5.2) is a representation of G, whose space is labelled by $(\boldsymbol{q}, \beta)$. This representation is induced by the irrep $d^{(\beta)}$ of the site symmetry group $G_{\boldsymbol{q}}$ of the Wyckoff position $\boldsymbol{q}$. The number of Wannier basis functions obtained, is equal to $n_\beta \times n_{\boldsymbol{q}} \times N$, where $n_{\boldsymbol{q}}$ is the multiplicity of the Wyckoff position and N is the number of unit cells. One should notice though, that the Wannier functions calculated in reality are centred within one primitive cell because the rest are just periodic translations.

Performing a Fourier transform on the Wannier basis, the corresponding Bloch functions are obtained

$$\psi^{(\beta)}_{i,j}(\boldsymbol{k},\boldsymbol{r}) = \frac{1}{\sqrt{N}} \sum_n e^{i\boldsymbol{k}\boldsymbol{t}_n} W^{(\beta)}_{i,j}(\boldsymbol{r}-\boldsymbol{t}_n)$$

The result is that, the infinite dimensional Wannier basis $n_\beta \times n_{\boldsymbol{q}} \times N$, is now substituted with a finite dimensional one $n_\beta \times n_{\boldsymbol{q}}$ for each one of the N $\boldsymbol{k}$ vectors of the First Brillouin Zone, that correspond to the $n_\beta \times n_{\boldsymbol{q}}$ energy bands. Now, acting with the element g on the Bloch functions

$$g\psi^{(\beta)}_{i,j}(\boldsymbol{k},\boldsymbol{r}) = \frac{1}{\sqrt{N}} e^{i\mathcal{R}\boldsymbol{k}\boldsymbol{t}_{j'j}} \sum_{i'} d^{\beta}_{(i'i)} \psi^{(\beta)}_{i',j'}(\mathcal{R}\boldsymbol{k},\boldsymbol{r}) W^{(\beta)}_{i,j}(\boldsymbol{r}-\boldsymbol{t}_n)$$

This is called *band representation.*

Restricting to the little group of symmetry $G_{\boldsymbol{k}}$ of a fixed wave vector $\boldsymbol{k}$ in reciprocal space, $\psi^{(\beta)}_{i,j}(\boldsymbol{k},\boldsymbol{r})$ span the space of the representation of $G_{\boldsymbol{k}}$ with character $\chi^{(\beta)}(g) = \sum_j^{n_q} e^{-i\boldsymbol{k}\boldsymbol{t}_{jj}} \tilde{\chi}^{(\beta)}(\mathcal{R}_j^{-1}\mathcal{R}\mathcal{R}_j)$. From this result one can obtain the number of times that the small irrep (k,α) of $G_{\boldsymbol{k}}$ with character $\chi^{(\alpha)}$ is contained in this induced representation $(\boldsymbol{q},\beta)$, subduced on $G_{\boldsymbol{k}}$. So, given the centres of the Wannier functions and the irreducible representations of their symmetry group, one can determine the corresponding irreps at each $\boldsymbol{k}$ point and vice versa [31] [32] [33].

The goal of this paragraph was to provide a small introduction to band representation and to create a bridge between the symmetry properties of Wannier functions centred at a fixed Wyckoff position, and those ones of the corresponding Bloch functions at a point of high symmetry $\boldsymbol{k}$ of the first Brillouin Zone.

5.2 SYMMETRIES

To construct nice Wannier functions for the problem on hand, one should first define the correct symmetries of the system. Starting with an initial configuration described by an AA stacking of two layers of graphene, the formation of a crystalline lattice does not depend on the displacement between the two sheets, neither on the centre of the rotation. It relies only on the angle of twist.

5.2.1 VALLEY CHARGE CONSERVATION

Based on how the primitive lattice vectors of the unrotated layer, are related to the Moiré lattice ones, one can obtain two classes of commensurate angles for the bilayer. These correspond to two different configurations of the folding of the monolayer Brillouin Zone into the mini-cell of the Moiré reciprocal lattice space. The two possible outcomes are shown in figure (5.1), and give an intuitive explanation of what happens in the folding.

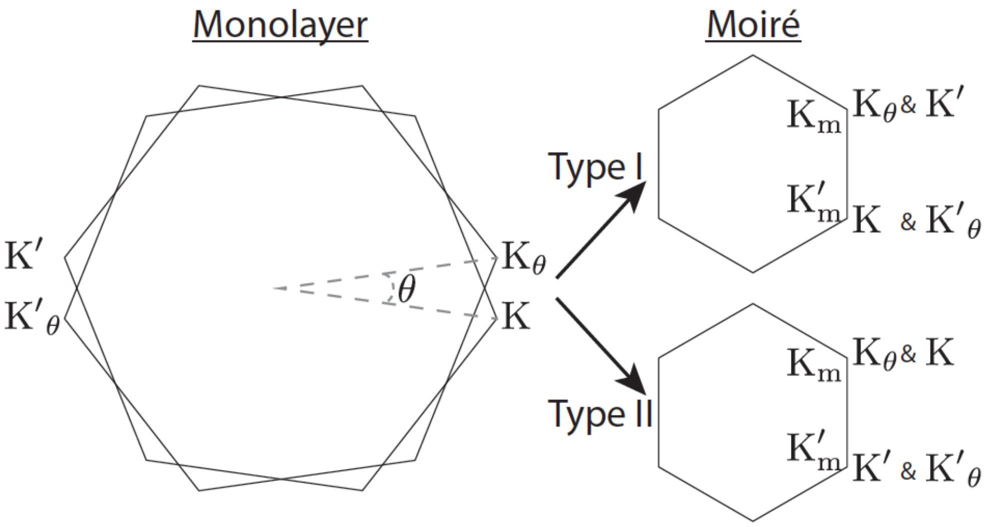

Figure 5.1: *The first Brillouin Zone of two graphene layers are rotated about their common centre of an angle θ. The mapping of the momentum in the new moiré BZ can be of two types, depending on the rotation. For type I, $\boldsymbol{K}'$ and $\boldsymbol{K}_\theta$ are folded into the same moiré $\boldsymbol{K}_m$ point, while for type II, they are $\boldsymbol{K}$ and $\boldsymbol{K}_\theta$ that are folded into the same $\boldsymbol{K}_m$* [28].

$\boldsymbol{K}$ and $\boldsymbol{K}'$ are the two inequivalent cones in the first layer, while $\boldsymbol{K}_\theta = R(\theta)\boldsymbol{K}$ and $\boldsymbol{K}'_\theta$ are the two in the second layer, with $R(\theta)$ the rotation matrix. This difference, in the analysis performed in chapter 2, was irrelevant because of the small value of θ. In type I, $\boldsymbol{K}'$ and $\boldsymbol{K}_\theta$ are folded into the same moiré $\boldsymbol{K}_m$ point, while for type II they are $\boldsymbol{K}$ and $\boldsymbol{K}_\theta$ that are folded into the same $\boldsymbol{K}_m$. These are the only two possible configurations allowed. In fact, because of time reversal, one can never have that two inequivalent Dirac cones of the same layer are folded into the same $\boldsymbol{K}_m$. From this construction, it seems that at least for type I configuration, valley charge conservation $U_v(1)$ is unreasonable. Even if, for type I the two inequivalent Dirac cones are folded into the same position, restricting to small angles of rotation, $\boldsymbol{K}'$ and $\boldsymbol{K}_\theta$ cannot couple. For small θ one finds that $|\boldsymbol{K} - \boldsymbol{K}_\theta| = |\boldsymbol{K}(\mathbb{1} - R(\theta))| \sim \mathcal{O}(\theta/a)$ (recalling $K \sim 1/a$), while $|\boldsymbol{K}' - \boldsymbol{K}_\theta| = |-\boldsymbol{K}(\mathbb{1} + R(\theta))| \sim \mathcal{O}(1/a)$. It follows that $|\boldsymbol{K} - \boldsymbol{K}_\theta| \ll |\boldsymbol{K}' - \boldsymbol{K}_\theta|$, so the coupling between inequivalent Dirac cones requires bigger reciprocal lattice vectors and this is why these hopping processes are suppressed for small angles of twist. It follows that $\boldsymbol{K}$ and $\boldsymbol{K}_\theta$ are grouped into a single valley and they do not interact with the time reversal cones in the other inequivalent valley.

One can easily construct the operator associated with this symmetry. In particular if $\widehat{N}_1$ is the operator associated to the number of electrons in the first valley, and $\widehat{N}_2$ in the second, the generator of $U_v(1)$ can be written as $\Delta\widehat{N}_v = \widehat{N}_1 - \widehat{N}_2$, finding $e^{-i\theta\Delta\widehat{N}_v}$.

The arguments made so far are independent of the commensurability of the lattice and perfectly apply to the effective model. The interlayer hopping term constructed in the second chapter, in fact, tends to zero rapidly with the reciprocal lattice vectors. The higher order processes are suppressed and $U_v(1)$ symmetry perfectly fits into the model.

5.2.2 POINT-GROUP SYMMETRIES

For a commensurate lattice, the exact point group symmetries do depend on the centre of the rotation. If it is performed about a generic point of space, one obtains a crystalline lattice with just translational invariance. To form high symmetry structures, one can twist the two sheets about the centre of one hexagonal cell or one of the honeycomb sites.

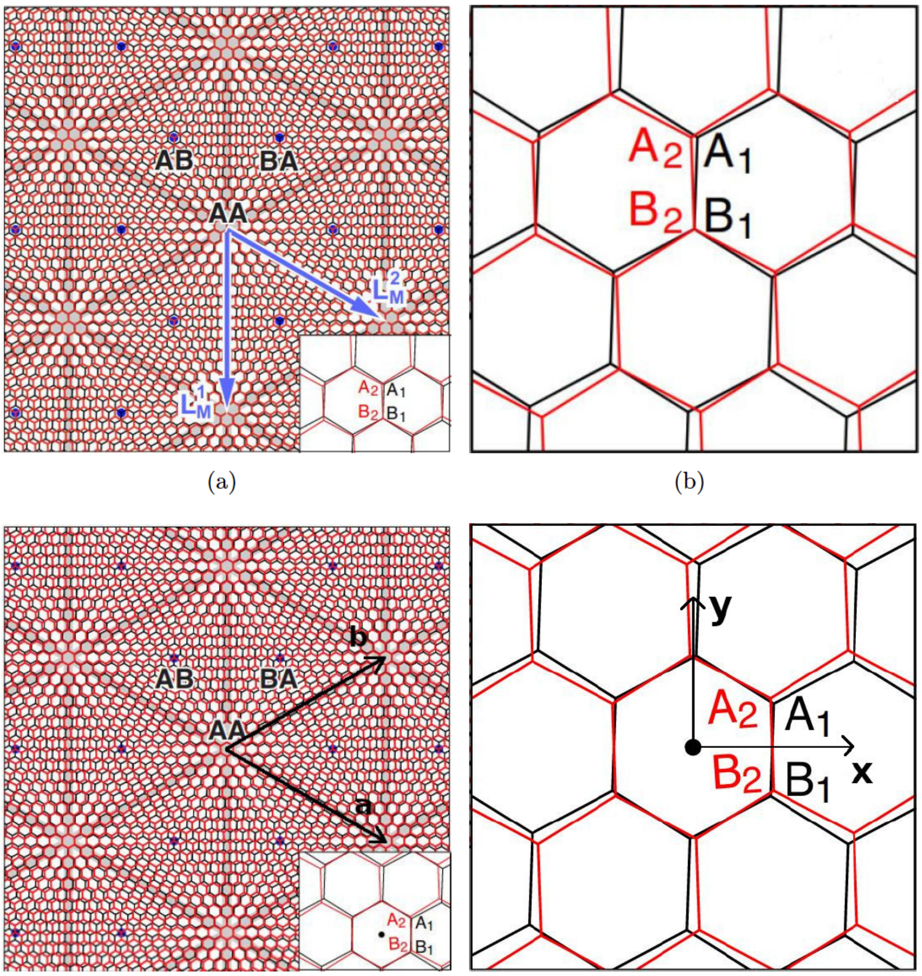

(a) (b)

(c) (d)

Figure 5.2: *Two stacked lattices of graphene with a twist. In (a) it is shown the formation of the hexagonal super-cell of the moiré lattice for two sheets of graphene rotated about a common atom site. The arrows represent the basis vectors and AA and AB the different stacking regions. In (b) a zoom in to the lattice rotation. In (c) it is shown the formation of the honeycomb super-cell of the moiré lattice for two sheets of graphene, rotated about a common centre of two overlapping hexagons. The arrows represent the basis vectors and AA and AB the different stacking regions. In (b) a zoom in to the lattice rotation.* [6] [34]

In the first case the system is invariant under D_6 point group. It contains the elements of the group C_6 and the other six rotations of angle π about the secondary axes parallel to the 2-D surface. C_6 contains all the rotations on the plane of 60°, 120° and 180° clockwise and counterclockwise, plus the identity E.

All the group operations of D_6 can be constructed combining the three generators C_{3z}, C_{2x} and C_{2y}. Studying the action of these symmetries on the indices that label the two layers, 1 and 2, the two sub-lattices within each layer, A and B and the two sub-lattices AB and BA of the moiré superlattice, one finds

- C_{3z} is the rotation about the z axis perpendicular to the 2-D plane of 120° that leaves invariant all indices
- C_{2x} is the rotation about the x axis of 180° that leaves invariant the AB and BA and exchanges the layers, the valleys and the sub-lattice indices
- C_{2y} is the rotation about the y axis of 180° that leaves invariant the A and B, and exchanges the layer, the moiré sub-lattice and the valley indices

The irreducible representations of the space group D_6 and the action of the three generators on them, are shown in the following table.

Irreps	C_{3z}	C_{2x}	C_{2y}
$A_1(1)$	$+1$	$+1$	$+1$
$A_2(1)$	$+1$	-1	-1
$B_1(1)$	$+1$	$+1$	-1
$B_2(1)$	$+1$	-1	$+1$
$E_1(2)$	$\begin{pmatrix}\cos(\phi) & -\sin(\phi)\\ \sin(\phi) & \cos(\phi)\end{pmatrix}$	$\begin{pmatrix}+1 & 0\\ 0 & -1\end{pmatrix}$	$\begin{pmatrix}-1 & 0\\ 0 & +1\end{pmatrix}$
$E_2(2)$	$\begin{pmatrix}\cos(\phi) & -\sin(\phi)\\ \sin(\phi) & \cos(\phi)\end{pmatrix}$	$\begin{pmatrix}+1 & 0\\ 0 & -1\end{pmatrix}$	$\begin{pmatrix}+1 & 0\\ 0 & -1\end{pmatrix}$

In parenthesis, next to each irreducible representation, it is written the corresponding order of degeneracy. The first four rows list the characters of the matrix representation, that for the first four rows coincide with the matrix itself. The angle $\phi = 2\pi/3$, [35].

When the rotation centre of the two layers of graphene is one of the honeycomb sites, the point group rotation shrinks to D_3. This implies that among others, C_6 is lost. In this case the character table for the generators of the group is

Irreps	C_{3z}	C_{2x}
$A_1(1)$	$+1$	$+1$
$A_2(1)$	$+1$	-1
$E(2)$	$\begin{pmatrix} \cos(\phi) & -\sin(\phi) \\ \sin(\phi) & \cos(\phi) \end{pmatrix}$	$\begin{pmatrix} +1 & 0 \\ 0 & -1 \end{pmatrix}$

There are only three irreps and two generators [36], [37] [38].

The configurations for the two different rotation centres are exhibited in figure (5.2). The plot refers to small angles of twist showing that in this case AA and AB/BA stacking-like regions appear.

5.2.3 HIGH SYMMETRY POINTS IN THE FBZ

It is now time to find the symmetry representations of the high symmetry points in the First Brillouin zone. These can be used to define the low-energy eigenvalues of the four minibands of the moiré lattice (two for each valley).

First one should understand the symmetry representations at the Dirac cones in the monolayer. These points are symmetric under the point group D_3, in fact a C_6 rotation would map $\boldsymbol{K}$ into the inequivalent point $\boldsymbol{K'}$. Following the analysis performed in reference [28], let's consider the action of C_{3z} about the centre of one hexagonal cell. The rotation acting on a Bloch state $\left|\psi^{\sigma}_{\boldsymbol{K}/\boldsymbol{K'}}\right\rangle$ at the Dirac point momentum $\boldsymbol{K}/\boldsymbol{K'}$, with $\sigma = \pm 1$ labelling the two sub-lattices A and B, is

$$\begin{aligned} C^{H}_{3z} \left|\psi^{\sigma}_{\boldsymbol{K}}\right\rangle &= \left|\psi^{\sigma}_{\boldsymbol{K}}\right\rangle \omega^{\sigma} \\ C^{H}_{3z} \left|\psi^{\sigma}_{\boldsymbol{K'}}\right\rangle &= \left|\psi^{\sigma}_{\boldsymbol{K'}}\right\rangle \omega^{-\sigma} \end{aligned} \tag{5.3}$$

with $\omega = e^{i2\pi/3}$.

Graphene lattice is still C_3 symmetric when the rotation is performed about a carbon site. This operation can be decomposed into translations about the basis lattice vectors $\boldsymbol{a}_1$ and $\boldsymbol{a}_2$, plus a rotation about the centre of the hexagon, $C^{c}_{3z} =$

$T_{\boldsymbol{a}_1}T_{\boldsymbol{a}_2}C_{3z}$. It follows

$$\begin{aligned} C^c_{3z}\left|\psi^\sigma_{\boldsymbol{K}}\right\rangle &= \left|\psi^\sigma_{\boldsymbol{K}}\right\rangle \omega^{\sigma-1} \\ C^c_{3z}\left|\psi^\sigma_{\boldsymbol{K}'}\right\rangle &= \left|\psi^\sigma_{\boldsymbol{K}'}\right\rangle \omega^{1-\sigma} \end{aligned} \tag{5.4}$$

These results can be used to understand what happens in the small rotation angle bilayer case. Let's take as reference type I configuration in figure (5.1). At the corner of the moiré Brillouin zone the Dirac point $\boldsymbol{K}_m$, corresponds to the folding position of $\boldsymbol{K}_\theta$ and $\boldsymbol{K}'$. These means that the Bloch state at $\boldsymbol{K}_m$ can be written

$$\begin{aligned} \left|\psi^\sigma_{\boldsymbol{K}_m},+\right\rangle &\propto \left|\psi^\sigma_{\boldsymbol{K}_\theta}\right\rangle \\ \left|\psi^\sigma_{\boldsymbol{K}_m},-\right\rangle &\propto \left|\psi^\sigma_{\boldsymbol{K}'}\right\rangle \end{aligned} \tag{5.5}$$

with ± that denotes the two decoupled valleys. The twisting centre, within the two lattices, implies either D_6 or D_3 point symmetry group, that corresponds to different irreducible representations. In the first case, taking as centre of C_{3z} rotation an AA cite

$$\begin{aligned} C^c_{3z}\left|\psi^\sigma_{\boldsymbol{K}_m},+\right\rangle &= \left|\psi^\sigma_{\boldsymbol{K}_m},+\right\rangle \omega^{\sigma} \\ C^c_{3z}\left|\psi^\sigma_{\boldsymbol{K}_m},-\right\rangle &= \left|\psi^\sigma_{\boldsymbol{K}_m},-\right\rangle \omega^{-\sigma} \end{aligned} \tag{5.6}$$

The representation of C^c_{3z} at $\boldsymbol{K}_m$ for the two sub-lattices and the two valleys is $(\omega,\omega^*)\cup(\omega,\omega^*)$. These are two doubly degenerate representations E of the little group D_3 (table (5.2.2)).

Considering a carbon atom as twisting centre within the layers, the action of the C_{3z} rotation about an AA cite results

$$\begin{aligned} C^c_{3z}\left|\psi^\sigma_{\boldsymbol{K}_m},+\right\rangle &= \left|\psi^\sigma_{\boldsymbol{K}_m},+\right\rangle \omega^{\sigma-1} \\ C^c_{3z}\left|\psi^\sigma_{\boldsymbol{K}_m},-\right\rangle &= \left|\psi^\sigma_{\boldsymbol{K}_m},-\right\rangle \omega^{1-\sigma} \end{aligned} \tag{5.7}$$

The representation of C_{3z} at $\boldsymbol{K}_m$ for the two sub-lattices and the two valleys is $(1,\omega)\cup(1,\omega^*)$. This in now the combination of all the representations of D_3, meaning $A_1\oplus A_2\oplus E$ (table (5.2.2)).

In both cases one finds that at K_m there is a four fold degeneracy that correspond to four zero energy eigenstates. Nevertheless, having either D_3 or D_6 as point group symmetry of the moiré lattice, implies different representations and thus different constrains on the tight-binding model. As it is pointed out in reference [28], for small angles of rotation the electronic properties of the system are independent on the exact geometrical features of the bilayer. This is true if the energy range of the analysis is of the order of the meV. It is in fact the case when one studies the almost flat mini-bands close to the magic angle. It follows that it is useful to implement always D_6, even when this is not an exact symmetry. In experiment Dirac cones are preserved even in unexpected circumstances and C_6 prevents from setting to zero symmetry allowed terms.

There are other high symmetry points in the moiré Brillouin zone, this are Γ, the centre of the FBZ and M, the midpoint between the two corners $\boldsymbol{K}_m$ and $\boldsymbol{K}'_m$. The little group at Γ, G_Γ, coincides with the point group G. This implies that for a D_6 lattice, the irreps at this point are the ones listed in table (5.2.2). On the other side, M has just D_2 symmetry group with four irreducible representations. The high symmetry points are shown in figure (5.3), where the arrows represents the line followed in the plots of the band structure.

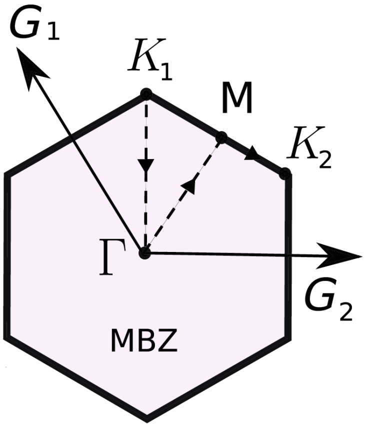

Figure 5.3: *Moiré Brillouin Zone of twisted bilayer graphene.* Γ, $K_{1/2}$ *and* M *are the high symmetry points, while the dashed lines represent the path followed in the band structure representation.* [35]

5.2.4 Remarks on the effective Hamiltonian

All the analysis performed so far, refers to commensurate structures. Nevertheless from second chapter for small angles of rotation, it is always possible to describe TBG with the continuum theory. Its Hamiltonian is constructed with two Dirac terms and a hopping matrix with a negligible dependence on the twist angle. This implies that no reference is made to the commensurability of the lattice and a crystalline study of the problem is allowed. The effective model preserves all the fundamental symmetries in the protection of Dirac cones. It is time reversal, has valley charge conservation and D_6 point group symmetry. Different lattices are then, well described by the same effective theory regardless of their different geometrical features. It implies that the results obtained from group theory can be applied to the continuum problem to study a wide range of structure. This becomes extremely important when the effect of corrugation is taken into account.

5.3 Centre of Wannier orbitals

An important step in the construction of Wannier orbitals, is the location of their centre. This depends on the symmetries of the energy bands at all high symmetry points [39]. The local density of state for the flat bands, is picked at the AA sites that generate a triangular lattice [19]. It is natural then, to create a tight-binding model on a triangular lattice from Wannier orbitals centred at AA regions. This is well represented in figure (5.2), where the moiré hexagon-cell appears constructed from six triangles with AA vertices and internal AB stacking. Taking into account a single valley, in the moiré first Brillouin zone Γ points present no degeneracy while K_m and K'_m are double degenerate ($U_v(1)$ degeneracy is not accounted). The construction of a triangular lattice model leads to the same symmetry representation for Γ, K_m and K'_m, that are now all non-degenerate or all Dirac points [19]. It follows that a correct tight-binding model should be described on a honeycomb lattice with the Wannier orbitals centred at the AB/BA regions, picked at the AA sites and with a non trivial shape. In monolayer graphene, this is equivalent to choose as centre of the Wannier orbitals the Wickoff position 2c, that identifies two points in the hexagonal unit cell. These correspond to the site of the two sub-lattice A and B, that are symmetric under the little group $G_{\boldsymbol{q}_{2c}}$, isomorphic to D_3.

5.4 Relaxation

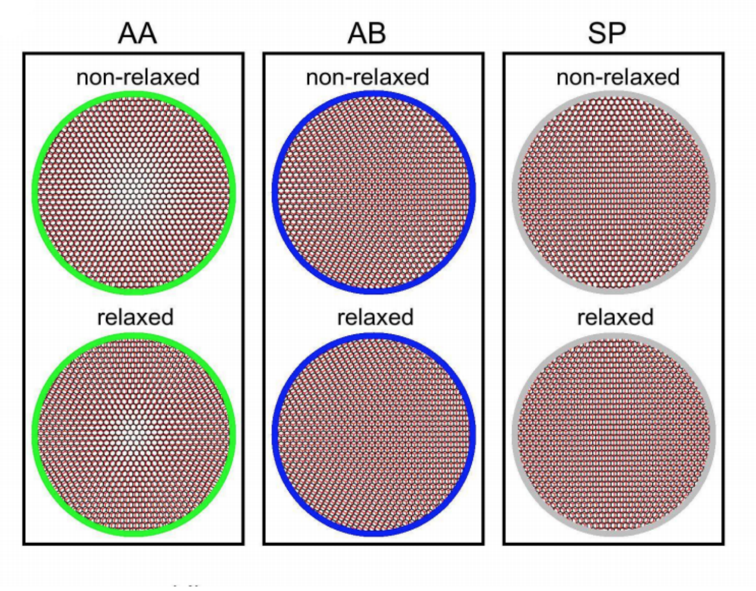

Figure 5.4: *Local structure of bilayer graphene for small twisted angles. The AA, AB and SP (regions between AB and BA) stacking are shown before and after the effect of relaxation. After corrugation the AA region shrinks to a small spot at the centre of the represented circle.* [40]

In the previous chapter it has been introduced the appearance of corrugation normal to the 2-D plane of TBG. Unless the lattice studied is an idealised version of real TBG, corrugation is a phenomenon that one should always expect and that is confirmed from experiments, specially at small twist angles. This effect is traced to a lattice relaxation with a stronger coupling energy between states at the AB/BA positions with respect to the AA ones. The main consequence is a bigger energy gap between the low energy mini-bands and those ones above and below. In addition to that, relaxation implies an in-plane deformation. AA regions tend to shrink, favouring an expansion of the AB ones and leading to the configuration shown in figure (5.2). The resulting lattice appears with bumps normal to the 2-D plane in correspondence to AA. To have an idea, for twisting angles $\sim 1°$ and full relaxation, one can find an interlayer distance difference of $\sim 0.2\text{Å}$ between AA ($\sim 3,61\text{Å}$

interlayer distance) and AB ($\sim 3,39$Å interlayer distance) sites starting with $d = 3,34$Å [40]. In figure (5.4), it is represented the local stacking structure before and after relaxation. In this numerical study, relaxation to stacked equilibrium positions of the atoms is accomplished by molecular dynamics, with effective force-fields to parametrize interactions between "classical" atoms. From the first image it is clear that the AA region shrinks to a small spot at the centre of the represented circle.

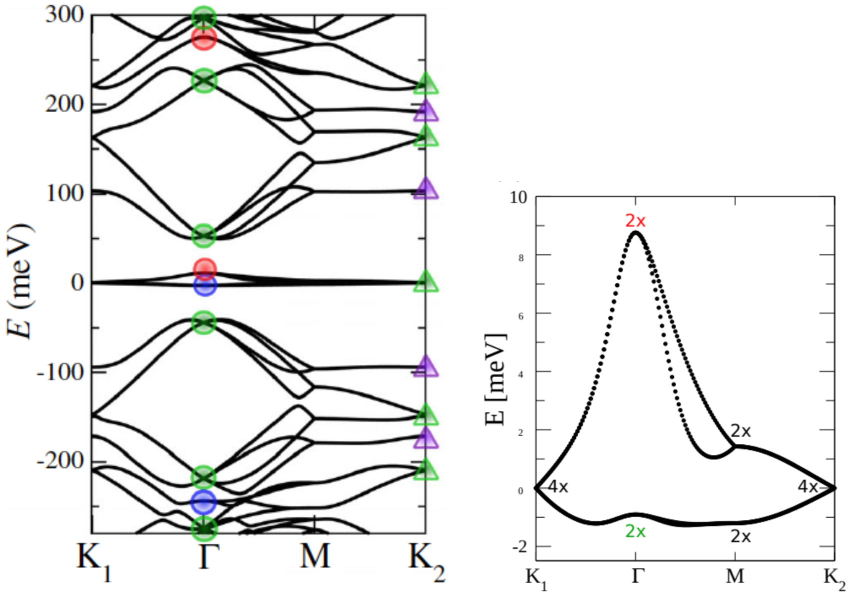

(a) (b)

Figure 5.5: *Band structure of twisted bilayer graphene for* $\theta = 1,08$ *angle of twist. In (a) the different coloured symbols refer to the irreducible representations at the high symmetry points. (b) zoom in to the flat bands. Numbers refer to the degeneracy at* Γ, $K_{1/2}$ *and* M*. It is included the effect of* $U_v(1)$ *valley charge conservation.* [35] [40]

For such a lattice there is not exact point symmetry group. Nevertheless, one should always consider D_6, even when the starting rotated lattice is D_3 [40]. As already pointed out, the exact local symmetry structure is irrelevant in the studying of the electronic properties of the sample. This result is proved, for example, by the study of the Bloch functions at the high symmetry points performed in [40] and [35].

In the figure (5.5a), it is shown the band structure from a tight binding numerical calculation of TBG at small angles with relaxation taken into account, [35]. The different coloured symbols refer to the irreducible representations at the high symmetry points, that transform like the corresponding Bloch functions. Blue, red and green circles correspond to $A_1 \oplus B_1$, $A_2 \oplus B_2$, $E_1 \oplus E_2$ irreps of D_6. Green and violet triangles stand for irreps E and $A_1 \oplus A_2$ of D_3.

Analysing only the low energy mini-bands, one can see that at Γ there are two doublets, namely $A_2 \oplus B_2$ for the upper band and $A_1 \oplus B_1$ for the lower one. Vice versa, at $\boldsymbol{K}$ there are two doublets of $E \oplus E$ (respectively one E for each cone).
In the second figure (5.5b), they are shown just the degeneracies at the flat bands. At each high symmetry point these are doubled with respect to the expected values. At $\boldsymbol{K}$ for example, from the E two dimensional representation one should expect only a double degeneracy. This is explained by the fact that $U_v(1)$ valley charge conservation must be taken into account. $U_v(1)$, in fact, implies an extra doubling of each degeneracy.

5.5 WANNIER OBSTRUCTIONS

At the end of the previous chapter it was clear the necessity to decide a tight-binding model for the mini-bands at low energy. The first step is to introduce a set of Wannier functions that exhibit the features and the symmetries of the system. This is not easy and even though many different models have been proposed, the problem is still open. As already mentioned, the difficulty on finding a tight-binding model for just the two low energy bands relies on the so called *Wannier obstructions* [28] [19].

The continuum model for a single valley, describes two almost flat bands with two Dirac cones at the border of the Brillouin Zone. In contrast to the monolayer lattice, there are two equivalent cones that correspond to a single valley. While in the first case two inequivalent Dirac points lie on the same band, in the latter there are two different bands each one with a couple of equivalent nodes. Wannier obstructions relies on the fact that, in any tight binding model, the Dirac cones have necessarily opposite winding number and net zero chirality. To overcome this problem one should add a term in the Hamiltonian for the other opposite valley. The consequence, though, is the breaking of single valley charge conservation, namely $U_v(1)$. Unless some symmetries are neglected, a well defined tight-binding model requires the introduction of extra bands. One can, in fact, describe the two low energy bands with all the symmetries of the continuum Hamiltonian and add higher energy ones that fix Wannier obstruction. This is equivalent to consider two set of two bands with opposite Chern number, that compensate each other from a topological point of view. Nevertheless, the obstruction is still somehow inherent in the problem since the two sets keep individually Wannier obstructions. This knot is harder to fix because it falls into a bigger issue, which is that bands with fragile topology do not admit any Wannier representation [41].

CONCLUSIONS

This thesis provides an in-depth analysis of small angle twisted bilayer graphene (TBG), extending topological properties of the monolayer to the TBG continuum model Hamiltonian and building a perspective on the most recent approaches to this problem.

The starting point of this work is the description of the electronic band structure of TBG throughout the study of the continuum model formulated by A. MacDonald and colleagues in 2012 [5]. At small angles of twist, the relevant excitations of the two layers of graphene, organise in a Moiré super-lattice that is described by an effective Hamiltonian. The Moiré band structure can be evaluated at arbitrary twist angles, not only at commensurate values. In particular, close to the magic angle the electronic structure, thus calculated, exhibits two nearly flat-bands near charge neutrality. Notably, by restricting to the first Moiré Brillouin zone, at first order approximation, one recovers a Dirac-like Hamiltonian in analogy to the single layer Dirac cones description.

This result is extremely important since it suggests the application of monolayer graphene topology at the Dirac cones to the bilayer lattice. In the former case the topological phase diagram is constructed from the Haldane model that, in some sense, is the simplest variant of grahene monolayer Hamiltonian exhibiting nontrivial topological features. This is a toy-model that explains the occurrence of quantum Hall effect on a standard Bloch band structure with broken time reversal but no net magnetic flux through the system. This procedure is extended to the bilayer continuum single valley Hamiltonian, finding a "flipped Haldane model" description. The phase diagram shows topological non-trivial states when C_2 symmetry is broken throughout an on-site potential that gaps the Dirac cones. On the other hand, the Chern number of the filled bands is null when the Haldane mass is included in the computations. This suggests an inconsistency in the outcomes. A non-zero Chern number is registered for an atomic insulator generated by a strong on-site potential. Hence it is reasonable and necessary to implement a tight-binding model with more then just two bands, to lighten up the physical contradictions of the result and to analyse the other unresolved properties of TBG.

Non-exact D_6 point group symmetry, relaxation of the two overlapping layers, together with fragile topology of the flat bands, are the problems tackled in the last part of this thesis. The construction of an accepted tight-binding model is still an open question and hangs on these obstructions. Even though these have often been neglected in early works, in our understanding their implementation is essential for the construction of a faithful model.

From this last viewpoint, this thesis does not show any landing or preference to a particular model, it rather lays the foundations for a future study. In particular, the construction of a tight-binding model with correlations between electrons could explain insulating states at half-filling of the flat bands. From latest experiments, in fact, it has been shown that TBG at the magic angle evinces Mott-like insulator behaviour alternated with superconducting phases when driven away from half-filling conditions. This is the reason why, in the last five years, there has been a tremendous interest in the study of this material. A good understanding of the problem and the proper formulation of a tight-binding model could explain the intriguing properties of this material and open the door for its possible controlled applications.

To conclude, the results of this work is the construction of a critical analysis that aims to deeply understand the features of small angle TBG continuum model, but at the same time unravel and comprehend its limits when one tries to revert back to localised low-energy orbitals in real space (Wannier functions) for Hubbard-like descriptions.

BIBLIOGRAPHY

[1] Yuan Cao, Valla Fatemi, Ahmet Demir, Shiang Fang, Spencer L. Tomarken, Jason Y. Luo, Javier D. Sanchez-Yamagishi, Kenji Watanabe, Takashi Taniguchi, Efthimios Kaxiras, Ray C. Ashoori, and Pablo Jarillo-Herrero. Correlated insulator behaviour at half-filling in magic-angle graphene superlattices. *Nature*, 556(7699):80–84, March 2018.

[2] Yuan Cao, Valla Fatemi, Shiang Fang, Kenji Watanabe, Takashi Taniguchi, Efthimios Kaxiras, and Pablo Jarillo-Herrero. Unconventional superconductivity in magic-angle graphene superlattices. *Nature*, 556(7699):43–50, March 2018.

[3] K. S. Novoselov. Electric field effect in atomically thin carbon films. *Science*, 306(5696):666–669, Oct 2004.

[4] F. D. M. Haldane. Model for a quantum hall effect without landau levels: Condensed-matter realization of the "parity anomaly". *Physical Review Letters*, 61(18):2015–2018, October 1988.

[5] R. Bistritzer and A. H. MacDonald. Moire bands in twisted double-layer graphene. *Proceedings of the National Academy of Sciences*, 108(30):12233–12237, Jul 2011.

[6] Mikito Koshino, Noah F.Q. Yuan, Takashi Koretsune, Masayuki Ochi, Kazuhiko Kuroki, and Liang Fu. Maximally localized wannier orbitals and the extended hubbard model for twisted bilayer graphene. *Physical Review X*, 8(3), Sep 2018.

[7] Wikipedia contributors. Electronic properties of graphene — Wikipedia, the free encyclopedia, 2020. [Online; accessed 10-February-2021].

[8] Leggett A.J. Graphene: Electronic band structure and dirac fermions. Lecture 5, summer 2010.

[9] A. H. Castro Neto, F. Guinea, N. M. R. Peres, K. S. Novoselov, and A. K. Geim. The electronic properties of graphene. *Reviews of Modern Physics*, 81(1):109–162, January 2009.

[10] Anthony T. Paxton. An introduction to the tight binding approximation–implementation by diagonalisation, 2009. Multiscale Simulation Methods in Molecular Sciences.

[11] Franz Utermohlen. Tight-binding model for graphene, September 12, 2018. report.

[12] Nilabha Bhattacharjee. *Multi-colour transient spectroscopy on single wall carbon nanotubes*. PhD thesis, Department of Physics and MathematicsUniversity of Eastern Finland, June 2012.

[13] Condensed Matter Group UCSD, Department of Physics. Moire superlattice. site page.

[14] J. M. B. Lopes-dos Santos, N. M. R. Peres, and A. H. Castro-Neto. Graphene bilayer with a twist: Electronic structure. *Physical Review Letters*, 99(25):6802, December 2007.

[15] R. Bistritzer and A. H. MacDonald. Transport between twisted graphene layers. *Physical Review B*, 81(24):5412, Jun 2010.

[16] Mikito Koshino. Interlayer interaction in general incommensurate atomic layers. *New Journal of Physics*, 17(1):015014, Jan 2015.

[17] Johannes C. Rode, Dmitri Smirnov, Christopher Belke, Hennrik Schmidt, and Rolf J. Haug. Twisted bilayer graphene: Interlayer configuration and magnetotransport signatures. *Annalen der Physik*, 529(11):1700025, July 2017.

[18] F. Rost, R. Gupta, M. Fleischmann, D. Weckbecker, N. Ray, J. Olivares, M. Vogl, S. Sharma, O. Pankratov, and S. Shallcross. Nonperturbative theory of effective hamiltonians for deformations in two-dimensional materials: Moiré systems and dislocations. *Physical Review B*, 100(3):5101, Jul 2019.

[19] Hoi Chun Po, Liujun Zou, Ashvin Vishwanath, and T. Senthil. Origin of mott insulating behavior and superconductivity in twisted bilayer graphene. *Physical Review X*, 8(3), Sep 2018.

[20] B. Andrei Bernevig and Taylor L. Hughes. *Topological Insulators and Topological Superconductors*. Princeton University Press, stu - student edition edition, 2013.

[21] DelftX. Topology in condensed matter, 2020. lecture notes.

[22] Wikipedia contributors. Adiabatic theorem — Wikipedia, the free encyclopedia, 2020. [Online; accessed 4-February-2021].

[23] Di Xiao, Ming-Che Chang, and Qian Niu. Berry phase effects on electronic properties. *Reviews of Modern Physics*, 82(3):1959–2007, July 2010.

[24] David Tong. The integer quantum hall effect. lecture notes.

[25] Jérôme Cayssol. Introduction to dirac materials and topological insulators. *Comptes Rendus Physique*, 14(9-10):760–778, Nov 2013.

[26] V.K.B. Kota. *Embedded Random Matrix Ensembles in Quantum Physics*. Springer International Publishing, 2014.

[27] Duc-Anh Le, Minh-Tien Tran, Thi-Thanh-Mai Tran, Thi-Thao Nguyen, Thi-Huong Nguyen, and Anh-Tuan Hoang. Phase transitions in the haldane-hubbard model within coherent potential approximation. *Physica B: Condensed Matter*, 532:139–143, 2018. Special issue on Frontiers in Materials Science: Condensed Matters.

[28] Liujun Zou, Hoi Chun Po, Ashvin Vishwanath, and T. Senthil. Band structure of twisted bilayer graphene: Emergent symmetries, commensurate approximants, and wannier obstructions. *Physical Review B*, 98(8):5435, August 2018.

[29] Jie Cao, Fenghua Qi, Hai Yang, and Guojun Jin. Monolayer-gap modulated topological phases in twisted bilayer graphene. *Physical Review B*, 101(15):5419, April 2020.

[30] Zhi-Da Song, Luis Elcoro, and B. Andrei Bernevig. Twisted bulk-boundary correspondence of fragile topology. *Science*, 367(6479):794–797, 2020.

[31] Jennifer Cano, Barry Bradlyn, Zhijun Wang, L. Elcoro, M. G. Vergniory, C. Felser, M. I. Aroyo, and B. Andrei Bernevig. Building blocks of topological quantum chemistry: Elementary band representations. *Physical Review B*, 97(3):5139, Jan 2018.

[32] R. Sakuma. Symmetry-adapted wannier functions in the maximal localization procedure. *Phys. Rev. B*, 87:235109, Jun 2013.

[33] Jiatong Chen, Ke Yin, Yi Xia, Vidvuds Ozolins, Stanley Osher, and Russel Caflisch. Symmetry-adapted Wannier Functions from L_1 regularized Sparse Optimization. In *APS March Meeting Abstracts*, volume 2016 of *APS Meeting Abstracts*, page B20.007, January 2016.

[34] Rennella Roberto. Symmetry analysis of twisted bilayer graphene (tbg). Master's thesis, universitá degli studi di Napoli "Federico II", 2019. Supervisor: Lucignano Procolo, Cantele Giovanni.

[35] M. Angeli, E. Tosatti, and M. Fabrizio. Valley jahn-teller effect in twisted bilayer graphene. *Physical Review X*, 9(4), Oct 2019.

[36] M. S. Dresselhaus. *Applications of Group Theory to the Physics of Solids*. Springer, 2002.

[37] Ado Jorio Mildred S Dresselhaus, Gene Dresselhaus. *"Group theory : application to the physics of condensed matter"*. "Springer", 2008.

[38] Smirnov Evarestov. *Site Symmetry in Crystals: Theory and Applications*. Springer series in solid-state sciences. Springer, 1993.

[39] Noah F. Q. Yuan and Liang Fu. Model for the metal-insulator transition in graphene superlattices and beyond. *Physical Review B*, 98(4):5103, Jul 2018.

[40] M. Angeli, D. Mandelli, A. Valli, A. Amaricci, M. Capone, E. Tosatti, and M. Fabrizio. Emergent d6 symmetry in fully relaxed magic-angle twisted bilayer graphene. *Physical Review B*, 98(23):5137, Dec 2018.

[41] Hoi Chun Po, Haruki Watanabe, and Ashvin Vishwanath. Fragile topology and wannier obstructions. *Physical Review Letters*, 121(12):6402, Sep 2018.